PHARMACOKINETIC-RATE IMAGING OF OPTICAL FLOUROPHORES AND BREAST CANCER DIAGNOSIS

By

Burak Alaçam

A Thesis Submitted to the Graduate

Faculty of Rensselaer Polytechnic Institute

in Partial Fulfillment of the

Requirements for the Degree of

DOCTOR OF PHILOSOPHY

Major Subject: Electrical Engineering

Approved by the
Examining Committee:

Birsen Yazici, Thesis Adviser

David Isaacson, Member

Badrinath Roysam, Member

Qiang Ji, Member

Xavier Intes, Member

Rensselaer Polytechnic Institute
Troy, New York

June 2008
(For Graduation August 2008)

PHARMACOKINETIC-RATE IMAGING OF OPTICAL FLOUROPHORES AND BREAST CANCER DIAGNOSIS

By

Burak Alaçam

An Abstract of a Thesis Submitted to the Graduate

Faculty of Rensselaer Polytechnic Institute

in Partial Fulfillment of the

Requirements for the Degree of

DOCTOR OF PHILOSOPHY

Major Subject: Electrical Engineering

The original of the complete thesis is on file
in the Rensselaer Polytechnic Institute Library

Examining Committee:

Birsen Yazici, Thesis Adviser
David Isaacson, Member
Badrinath Roysam, Member
Qiang Ji, Member
Xavier Intes, Member

Rensselaer Polytechnic Institute
Troy, New York

June 2008
(For Graduation August 2008)

CONTENTS

LIST OF TABLES

LIST OF FIGURES

ACKNOWLEDGMENT

To my family, my advisor, and my friends...

First and foremost, I specially want to thank to my advisor, Dr. Birsen Yazici. She has supported me throughout my thesis with her patience and knowledge. She always trusted in me, and motivate me for pursuing a Ph.D. degree. She always wanted me to do my very best, and spent her precious time with me to achieve this goal. I attribute the level of my Ph.D. degree to her encouragement and effort. Without her, this thesis would not have been possible. Once again, Hocam, I would like to thank you for everything. I will do my very best to deserve what you have invested in me to be a good academician and a good person.

I started my Ph.D. journey at Drexel University. Dr. Nihat Bilgutay is the person who trusted in me, and accepted me in the program. I want to thank him for all his support. He is one of the best people I have ever met. I hope he gets well soon...

I want to thank my father, Mehmet Ali Alacam, my mother Sevim Alacam, and my sister Burcu Alacam MILLION TIMES for always believing in me. I love them more than anything in the world.

I want to thank to Dr. Murat Guven. We work for the same advisor for years and years, both at Drexel University and RPI. We shared a lot in those years. We supported each other and made each other believe that Ph.D. is going to end one day. Murat thanks for everything...

I thank to Dr. Xavier Intes. I met him at UPENN where he was a post doc. After 3-4 years, he came to RPI and I had a chance to know him more. I am lucky in that respect. Thank you Dr. Intes for all your help, as a friend and as an academician...

I would like to thank my friends and coaches at RPI table tennis team, namely, Coach Jennifer Choi, Coach Joey Garcia, team members, Anurat Chapanond, Benjamin Tom, Yin Wang, Kumar Deep, Joel Dever, Michael Li, Greg Gennuso. It was

fun to be with you guys. I enjoyed it a lot...

More thanks to people:

At Drexel University, Dr. Banu Onaral, Dr. Meltem Izzetoglu, and Kurtulus Izzetoglu.

At University of Pennsylvania, Dr. Britton Chance, Dr. Shoko Nioka, and David Busch.

At RPI, Dr. David Isaacson, Dr. Badrinath Roysam, Dr. Qiang Ji, Dr. George Nagy, Ann Bruno, George Narode, Priscilla Magilligan, and Laraine Michaelides.

Finally, I want to thank to my friends, (the names are in random order, do not worry. Hmmm, I know you are going to think, "even if he says it is random, actually it is not". Hence, I prefer to arrange them in terms of surnames. I love you all), Lucky Utku Gunay Acer, Gulsah Angi, Alper Ayvaci, Murat Sabri Bicer, Ali Bulman, Umut Bulut, Dogan Can, Burak Cavdaroglu, Anurat Chapanond, Huseyin Dinc, Bilge Eker, Yasemin Eryigit, Pinar Gedikoglu, Betul Gencel, Kerem Goren, Murat Guven, Ekin Pehlivanoglu, Ezgi Taslidere, Banu Suzan Tezel, Fatma Tezel, Can Evren Yarman, and Gunay Yurtsever. I shared unforgettable memories with each one of you. Without you, I would have never finished my Ph.D.

Thanks to everyone here, and that I mistakenly forgot. It has been great pleasure working with you, spending time with you, sharing time with you. Thank you for being a part of my life during my Ph.D. years. Come visit me anytime, write to me anytime. I hope, I do not lose contact with any of you...

ABSTRACT

In this thesis, we study the value of near infra-red (NIR) optical imaging and spectroscopy techniques for breast cancer detection, diagnosis, and staging. In particular, we develop new mathematical models and computational techniques to investigate the value of endogenous contrast provided by NIR imaging and spectroscopy; and the pharmacokinetic information provided by optical fluorophores, specifically, indocyanine green (ICG).

First, we developed three different compartmental models to model the pharmacokinetics of ICG for healthy and malignant tissue. We introduced a systematic and robust approach to estimate and analyze ICG pharmacokinetics based on the extended Kalman filtering (EKF) framework. Additionally, we introduce an information theoretic criteria for the best compartmental model order selection. We tested our approach using the ICG concentration data acquired from four Fischer rats carrying adenocarcinoma tumor cells. Our animal study indicates that pharmacokinetic rates are potentially useful parameters for tumor differentiation and staging.

Secondly, we develop a method of forming pharmacokinetic-rate images of ICG. To form pharmacokinetic-rate images, we first obtain a sequence of ICG concentration images using the differential diffuse optical tomography technique. We next employ a two-compartment model composed of plasma, and extracellular-extravascular space (EES), and estimate the pharmacokinetic-rates and concentrations in each compartment using the EKF framework. The pharmacokinetic-rate images of the three patient show that the rates from the tumor region and outside the tumor region are statistically different. Additionally, the ICG concentrations in plasma, and the EES compartments are higher around the tumor region agreeing with the hypothesis that around the tumor region ICG may act as a diffusible extravascular flow in compromised capillary of cancer vessels.

Thirdly, we present a new method to form pharmacokinetic-rate images of optical fluorophores directly from NIR boundary measurements. We first derive a map-

ping from spatially resolved pharmacokinetic-rates to NIR boundary measurements by combining compartmental modeling with a diffusion based NIR photon propagation model. We express this mapping as a state-space equation. Next, we introduce a spatio-temporal prior model for the pharmacokinetic-rate images and combine it with the state-space equation. We address the image formation problem using the EKF framework. We analyzed the computational complexity of the resulting algorithms and evaluate their performance in numerical simulations. Simulation results show that the resulting algorithms are more robust and lead to higher signal-to-noise ratio as compared to existing approaches where the reconstruction of concentrations and compartmental modeling are treated separately. Additionally, we reconstructed pharmacokinetic-rate images using *in vivo* data obtained from three patients with breast tumors. The reconstruction results show that the pharmacokinetic-rates of ICG are higher inside the tumor region as compared to the surrounding tissue.

Finally, we present a study on the evaluation of a set of optical features extracted from *in vivo* NIR spectroscopy data obtained from 116 patients with breast tumors for breast cancer diagnosis. The *in vivo* data was collected from 44 patients with malignant and 72 patients with benign tumors. Three features, relative blood volume concentration, oxygenation desaturation and the size of the tumor, are used to differentiate benign and malignant tumors. The diagnostic capability of these features are evaluated using different classifiers including nearest mean, neural network, support vector machine, Parzen, and normal density-based classifiers. The area under the receiver operating characteristics curve of the nearest mean classifier using the three features yields the best value of 0.91. This result suggests that relative blood volume concentration, oxygenation desaturation and size information can differentiate malignant and benign breast tumors with a relatively high precision.

CHAPTER 1

1.1 Introduction

1.1.1 Breast Cancer Statistics

American cancer society (ACS) estimates that a total of nearly 200,000 new cases of invasive breast cancer will occur in women in the United States during the year 2008 [1]. Currently, there are over 2 million women living in the US who have been diagnosed with and treated for breast cancer. A total of 40,500 women are predicted to die from breast cancer in the US during the year 2008 as per ACS estimates [1]. Breast cancer continues to be the leading cancer among American women and is second to lung cancer in cancer deaths. Breast cancer is the leading cause of cancer deaths among women ages 40-59.

Early detection is critical for effective treatment of breast cancer. Patients with tumors 1 cm or less in size have more than 90% long-term survival [217]. Imaging of breast tumors plays an important role in the early detection. Although the number of breast cancer patients continues to increase since 1980, due to the new imaging and screening modalities, the death rates from breast cancer have declined in the US by 2.8% every year from 1990 to 2008.

1.1.2 Breast Imaging Modalities

There are a number of well established imaging modalities for breast cancer screening, diagnosis and staging. These include X-ray mammography, ultrasound, and magnetic resonance imaging (MRI). There are also emerging modalities such as positron emission tomography (PET) scan, and near-infrared (NIR) techniques that are currently being evaluated for breast cancer.

Currently, the most common screening technique is X-ray mammography which is a specific type of imaging that uses low-dose X-rays to image and examine breast tumors [3–5,211,212]. Although it is of great importance to breast cancer screening, it has a number of limitations. Every time a woman undergoes mammography, there is an 15% chance that the result is false positive, which can lead to additional, and

costly, imaging studies and biopsies. Approximately 15% of breast tumors are undetectable by X-ray mammography [213, 214]. The method also cannot accurately distinguish between benign and malignant tumors. Additionally, mammography exposes sensitive tissue to radiation and its exposure is a known risk factor for breast cancer.

Ultrasound is another imaging modality that is used for breast cancer detection and diagnosis [6–8,213,214]. The major advantage of ultrasound is its potential ability to differentiate cyst formations from other types of tumors. Ultrasound, however, has some drawbacks. Typically, tumor diagnosis is based on the radiologist's qualitative evaluation of the morphological features in ultrasound images. This approach, however, is prone to variability, due to lack of quantitative measures and degree of experience among radiologists, hence the false-positive rates can go up to 20% [8, 213, 214]. Additionally, an ultrasound image does not have enough spatial resolution an therefore does not provide as much detail for deeply located breast abnormalities.

MRI is also utilized to detect and diagnose breast tumors [9–11, 215, 216]. MRI is based on the principles of nuclear magnetic resonance, a spectroscopic technique, which is used to obtain microscopic chemical and physical information about molecules. MRI is often used to investigate breast tumors first detected with mammography, physical exam, or other imaging systems. It can be useful for staging breast cancer. However, MRI cannot always distinguish between cancerous and non-cancerous tumors with a false-positive rate of about 23% [215,216]. This can lead to unnecessary breast biopsies. Another drawback of breast MRI is that, it has been unable to image micro-calcifications. Furthermore, MRI is a relatively expensive modality for routine screening and diagnosis.

PET is another imaging modality that is currently being studied for breast cancer detection and diagnosis [55–58,205]. However PET's specificity is low. Moreover, conventional imaging techniques, i.e., MRI, X-ray, or ultrasound, are necessary for exact localization and correct interpretation of PET findings.

1.1.3 NIR Imaging and Spectroscopy for Breast Cancer

NIR optical methods provide complementary functional information that is not accessible by the imaging methods described above. There are various NIR imaging and spectroscopy techniques. These include optical spectroscopy [20, 21], diffuse optical tomography (DOT) [17–19], optical coherence tomograph (OCT) [24, 34], fluorescence diffuse optical tomograph (FDOT) [13–16], optical fluorescence reflectance imaging [36, 37], optical bioluminescence tomography (OBT) [22, 23], and pharmacokinetic-rate imaging of optical fluorophores [25, 95–97, 150, 179]. NIR techniques can provide *in vivo* measurements of oxygenation and vascularization state, the uptake and release of optical fluorophores and chromophore concentrations with high sensitivity. There is considerable evidence that tumor growth is dependent on angiogenesis [12]- [39], and that tumor aggressiveness can be assessed from its increased number of new vessels and reduced oxygenation state relative to normal breast tissue and benign breast lesions [40]- [42]. NIR methods has the potential to characterize angiogenesis related vessel density as it measures the total hemoglobin concentration and provide the ability to differentiate between benign and malignant lesions based on oxygen saturation. NIR methods are non-ionizing, relatively inexpensive and can be made portable.

NIR techniques in conjunction with NIR optical fluorophores have the potential to image (locate) and/or to differentiate between malignant and benign tumors [62, 63, 71–77, 81, 85]. One way of locating and diagnosing the tumor is pharmacokinetic-rate imaging of optical fluorophores [25, 95–97, 150, 179].

1.1.4 Pharmacokinetics of Optical Fluorophores and Compartmental Modeling

Pharmacokinetics can be defined as the mathematics of the time course of absorption, distribution, and excretion of optical fluorophores in the body [105]. The biological alterations such as cancerous tissues which influence the transfer processes of these fluorophores also influence the rate of change of absorption and excretion in the body. Hence, the analysis of pharmacokinetics of optical fluorophores is a potential means for tumor detection, diagnosis, staging, treatment monitoring, and

feasibility studies [144].

One approach to pharmacokinetic-rate analysis is the compartmental modeling [50, 187, 188]. In this method, a region of interest consists of a number of compartments, generally representing a volume of similar tissues into which the fluorophores are distributed. The concentration changes in a specific compartment are modeled as a result of the exchange of fluorophores between connected compartments. These changes are modeled by a collection of coupled ordinary differential equations (ODE); each equation describing the time change dictated by the biological laws that govern the concentration exchanges between the interacting compartments. Coefficients of the ODE's are called the pharmacokinetic rates that represent rates of exchange between different compartments. As in MRI [204, 215, 216], and PET [149, 205] compartmental modeling of optical fluorophores by means of NIR imaging techniques can provide useful physiological information for tumor detection, diagnosis, drug delivery and feasibility studies.

In the NIR range, the most widely used optical fluorophore is indocyanine green (ICG) [44, 45, 98–102]. ICG is a safe, and US Food and Drug Administration approved NIR absorbing and fluorescing dye. It is an intravascular contrast agent that may extravasate through vessels of high permeability, such as cancerous vessels. Therefore, ICG pharmacokinetic-rate imaging of the breast around tumor region mainly probes permeability and vascularization.

Several group of researchers reported compartmental modeling of ICG in animal and human subjects and studied the parameters related to capillary permeability as malignancy indicators [25, 95–97]. In [95] *in vivo* fluorescent NIR reflectance images of ICG were analyzed and the pharmacokinetics of ICG was studied to discriminate spontaneous canine adenocarcinoma from normal mammary tissue using a two-compartment model. It was concluded that the model parameters show no difference in the ICG uptake rates between the normal and diseased tissue regions. In [96] a study of the dynamics of ICG was presented in an adenocarcinoma rat tumor model. A compartmental model describing ICG dynamics was used to quantify physiologic parameters related to capillary permeability. In [97] the uptake of ICG by breast tumors was studied using a continuous wave diffuse optical tomography

apparatus. A two-compartment model was used to analyze the pharmacokinetics of ICG. This study shows that the malignant cases exhibits slower rate constants (uptake and outflow) compared to healthy tissue.

While the studies described above demonstrate the feasibility of the ICG pharmacokinetics in tumor characterization; due to the highly non-linear nature of the pharmacokinetic parameter estimation, variation in parameter values from one subject to another, and sparse data available in clinical and laboratory settings, a *systematic and robust* approach is needed to model, estimate and analyze ICG pharmacokinetics. Such an approach must include, a method for compartmental model order selection, a robust method of estimating ICG pharmacokinetic parameters, and a method of validating the selected model and the estimation results.

1.2 Thesis Outline

In this thesis, we study the value of NIR optical imaging and spectroscopy techniques for breast cancer detection, diagnosis, and staging. In particular, we develop mathematical modeling and computational techniques to investigate the value of *i*) pharmacokinetic information provided by ICG; and *ii*) the endogenous contrast provided by NIR imaging and spectroscopy.

In this thesis, we completed the following work:

1. We developed a method for mathematical modeling and estimation of pharmacokinetics of ICG using compartmental modeling and extended Kalman Filtering (EKF) framework. We tested our approach using the ICG data acquired from four Fisher rats carrying adenocarcinoma tumor cells. This work is presented in our publications [25, 137, 138].

2. We obtained spatially resolved pharmacokinetic-rate images of ICG using the NIR data acquired from three patients with breast tumors using a voxel-by-voxel construction method. This work is presented in our publications [179, 181].

3. We developed a method to reconstruct pharmacokinetic-rate images of optical fluorophores *directly* from boundary measurements. We tested our approach

using a simulated data set. We compared the *direct* reconstruction algorithm with the voxel-by-voxel reconstruction algorithm in simulation studies. We *directly* reconstructed spatially resolved pharmacokinetic-rate images of ICG using NIR data acquired from three patients with breast tumors, and compare our results with voxel-by-voxel reconstruction. This work is presented in our publications [178, 180, 183].

4. We evaluated the diagnostic value of total blood volume and oxygen saturation provided by endogenous NIR chromophores using the *in vivo* data acquired from 116 patients with breast tumors. This work is presented in our publications [184, 185].

1.2.1 EKF for the Modeling and Analysis of ICG Pharmacokinetics in Cancerous Tumors using NIR Optical Methods

In this work, we presented three different compartmental models for the ICG pharmacokinetics in cancerous tumors and propose an EKF framework to estimate the model parameters. The models capture the transportation of ICG between the vascular and extravascular compartments, including interstitial fluid region, parenchymal cell, intracellular binding site, and extravascular, extracellular spaces (EES).

We also presented a method for selecting the optimal compartmental model order based on Bayesian Information Criterion (BIC), and a statistical validation method based on residual analysis. We test our approach using the ICG concentration data acquired from four Fisher rats carrying adenocarcinoma tumor cells. Two-, three- and four-compartment models are fitted to data and pharmacokinetic model parameters and concentrations in different compartments are estimated using the EKF framework. The BIC suggests that the two-compartment model provides a sufficient fit for our data. The estimated model order and the model parameters are further validated by residual analysis. The model parameters are used to differentiate between two types of cancerous tumors. Our study suggests that the permeability rates out of the vasculature are higher in edematous tumors as compared to necrotic tumors. Additionally, we observe that in the two-compartment

model, the ICG concentration curve is higher in the EES compartment in edematous tumors. This suggests that the ratio of the peak value of the ICG concentrations in different compartments may be a useful parameter to differentiate tumors.

The advantages of EKF for the modeling and analysis of ICG pharmacokinetics are as follows:

- Effective modeling of multiple compartments, and multiple measurement systems governed by coupled ordinary differential equations, in the presence of measurement noise and compartmental model mismatch. This has the advantage of providing better fit than the exponential curve models ([95, 96, 150]) for the pharmacokinetics of optical fluorophores.

- Explicit estimation of the pharmacokinetic-rate parameters, volume fractions and concentrations in different compartments. (Unlike the methods in [95, 96, 150]).

- Suitable not just for the deterministic coupled ODEs but also for the stochastic coupled ODEs for the compartmental modeling.

- Not specific to a particular optical fluorophore, but applicable to the pharmacokinetic rate estimation of any optical fluorophore.

- Simultaneous estimation of pharmacokinetic model parameters and ICG concentrations in each compartment, which are not accessible *in vivo* by means of NIR techniques.

- Statistical validation of estimated concentrations and error bounds on the pharmacokinetic parameter estimates.

- Potential real-time monitoring of ICG pharmacokinetic parameters and ICG concentrations in different compartments due to the recursive nature of the EKF estimation method.

1.2.2 Voxel-by-Voxel Reconstruction of Spatially Resolved Pharmacokinetic Rate Images of ICG using Near Infrared Optical Methods

In [25, 137, 138], we assume that the pharmacokinetic-rates are constant over a tissue volume that may be as large as the entire imaging domain. However, pharmacokinetic-rates are expected to be different in healthy and tumor tissue as reported in PET, and MRI literature. It was shown that the spatially resolved pharmacokinetic-rate analysis provides increased sensitivity and specificity for breast cancer diagnosis [29, 32, 33]. For example, Sun *et al* [33] showed that FAU (1-2'-deoxy-2'-fluoro- β-D-arabinfuranosyl urasil, a PET contrast agent) accumulation in tumor region is significantly higher when compared to normal breast tissue based on pharmacokinetic-rate images. Mussurakis *et al* [29] showed that the pharmacokinetics of gadolinium-DTPA (an MRI contrast agent) can be used to differentiate between malignant and benign breast tumors with a high accuracy. It has also been shown that the spatially resolved image interpretation is superior to the isolated use of quantitative pharmacokinetic-rates.

In the area of diffuse NIR spectroscopy and imaging, a number of studies on spatially resolved pharmacokinetic-rates has been reported [95, 150]. Gurfinkel et al. [95] presented *in vivo* NIR reflectance images of ICG pharmacokinetics to discriminate canine adenocarcinoma (located at 0.5-1 cm depth) from normal mammary tissue. These images were generated by a non-tomographic technique using a CCD camera that is suitable only to image tumors close to surface. Milstein *et al* [150] presented a Bayesian tomographic image reconstruction method to form pharmacokinetic-rate images of optical fluorophores based on FDOT. Numerical simulations show that the method provides good contrast. However, no real data experiments were presented to study the diagnostic value of spatially resolved pharmacokinetic-rates.

In this work, we obtained spatially resolved pharmacokinetic rate images of ICG, using NIR data acquired from patients with breast tumors using a voxel-by-voxel reconstruction method. We first developed a set of temporally resolved 2-D ICG concentration images based on linearized diffusion model. We then estimated the ICG pharmacokinetic rates and the concentrations in each compartment for each

voxel based on the EKF framework and the two-compartment model. Reconstructed 2-D pharmacokinetic rate images of the three patient show that the rates from inside and outside the tumor region are statistically different with a p-value of 0.0001. Additionally, the ICG concentrations in plasma and the EES compartments are higher around the tumor agreeing with the hypothesis that around the tumor region ICG may act as a diffusible extravascular flow in leaky capillary of cancer vessels.

The advantages of obtaining spatially resolved pharmacokinetic-rate images as compared to bulk rates for breast cancer diagnosis are as follows:

- Localization of heterogeneities, i.e., tumors.
- Morphological comparison of pharmacokinetic-rate images and ICG concentration images in different compartments.
- Statistical comparison of pharmacokinetic rates from the inside and the outside of tumor region.

  For all these reasons, spatially resolved pharmacokinetic-rate images lead to consistent and superior diagnostic information as compared to bulk pharmacokinetic rates.

1.2.3 Reconstruction of Spatially Resolved Pharmacokinetic Rate Images of Optical Fluorophores from NIR Measurements

As a next step, we developed a method to reconstruct spatially resolved pharmacokinetic rate parameters of fluorophores *directly* from the boundary measurements using EKF framework [178, 180, 183].

We first derived a mathematical model that maps the boundary measurements to the total fluorophore concentrations. We call this map *concentration-to-measurement* (CTM) map. For this, we combined the compartmental model with a NIR photon propagation model which maps the total fluorophore concentrations to boundary measurements. To model photon propagation, we used the diffusion approximation to radiative transfer equation where the propagation of excitation

and emission light are modeled by two coupled diffusion equations [145]. We derived two CTM maps: linear time-invariant CTM map and non-linear time-varying CTM map for dynamic boundary measurements. In the linear time-invariant CTM map, the relationship between the total fluorophore concentration and the boundary measurements is linear and does not vary with respect to the time (time which describes the evolution of the fluorophore concentration). In the non-linear time-varying CTM map, on the other hand, the relationship between the total fluorophore concentration and the boundary measurements is non-linear at every instant of the tomographic data collection process and it varies with respect to time. We formed a state-space model based on the compartmental model equations and the NIR photon propagation model. Then, we derived a map relating the boundary measurements to spatially resolved pharmacokinetic-rates. We called this mapping *pharmacokinetic-rates-to-measurement* (PTM) map. We introduced a spatio-temporal prior model for the pharmacokinetic-rate and volume fraction parameters and incorporate this model to the state-space representation. We utilized the extended Kalman filtering (EKF) framework to address the resulting image reconstruction problems.

We analyzed the computational complexity of the resulting algorithms (linear and non-linear) and compare them with that of the voxel-by-voxel algorithm [179]. We evaluated the performance of our algorithms in numerical simulations using a tissue like numerical phantom. Our numerical study shows that there is a good agreement between the true and the estimated images in terms of localization of the heterogeneities and with respect to normalized mean-squared error criterion. Furthermore, the numerical studies show that the new method is more robust than the voxel-by-voxel algorithm with higher signal-to-noise ratio. Additionally, we present reconstruction of pharmacokinetic-rate images from *in vivo* data acquired from three patients with breast tumors. The reconstructed images show that they are superior than images reconstructed by voxel-by-voxel reconstruction algorithm.

An important feature of the method introduced here is the direct reconstruction of the pharmacokinetic-rate images of optical fluorophores as opposed to voxel-by-voxel reconstruction algorithm that we reported in [179]. The voxel-by-voxel algorithm does not take into account the temporal correlations due to decoupled

nature of the two-step algorithm described above. The new method, on the other hand, makes effective use of the temporal correlations present in the dynamic measurements by coupling the two steps and incorporating a spatio-temporal *a priori* model. This has the advantage of improved robustness and signal-to-noise ratio as compared to the voxel-by-voxel reconstruction method.

EKF framework was previously used to address the reconstruction of optical parameters [146–148]. In [146], Eppstein *et al.* utilized EKF to reconstruct images of absorption coefficient, fluorescence lifetime, and quantum efficiency using simulated noisy measurements. This study uses a dynamic model to impose spatial smoothing on the unknown optical parameters, but does not consider dynamic imaging of time-varying optical parameters. In [147] and [148], Kolehmainen *et al.*, and Prince *et al.* used EKF to reconstruct time-varying absorption images of human motor cortex. These studies demonstrate that EKF provides an effective framework in dynamic tomography problems in diffuse optical imaging. The underlying dynamic model in these studies assumes that the unknown optical image, i.e., the state variables, remains constant up to an additive noise term and the measurement model is given by the diffusion equation. In our work, on the other hand, the dynamic model is based on the coupled ODE's of the compartmental model while the measurement model is based on the CTM map derived from the two coupled diffusion equation representing the fluorescence light propagation.

In [150], Milstein *et al.* presented a direct reconstruction method for the pharmacokinetic-rate images of optical fluorophores. This work uses an exponential curve model for compartmental modeling and a linear time-invariant fluorescence light propagation model derived based on authors' prior work in [88, 89]. The reconstruction of pharmacokinetic-rate images is addressed based on maximum *a posteriori* (MAP) estimation together with a parametric iterative coordinate descent optimization technique similar to the approach in [149].

The advantages of direct reconstruction of pharmacokinetic-rate images using EKF algorithm are as follows:

- Addresses the pharmacokinetic-rate imaging based on both linear time-invariant and non-linear time-varying CTM maps. Non-linear time-varying CTM map

provides a more accurate relationship between the total fluorophore concentration and boundary measurements.

- Provides an effective method to address the pharmacokinetic-rate imaging based on nonlinear time-varying CTM map.
- Provides an effective framework for dynamic tomography within a recursive, linear estimation framework eliminating the need for numerical optimization. Furthermore, its noise suppression property can be improved by backward smoothing [191].
- Allows real time pharmacokinetic-rate imaging.
- Allows incorporation of spatio-temporal *a priori* models to the estimation scheme for improved robustness and SNR.

1.2.4 Evaluation of NIR Optical Features for Breast Cancer Diagnosis using *in vivo* Patient Data

We study the diagnostic capability of the endogenous flourophores (*optical features*) using NIR spectroscopy.

Interpretation of the *optical features* (i.e. deoxyhemoglobin, oxyhemoglobin, blood volume, water content, scattering, and absorption) has the capability to correctly diagnose the tumor, hence has a potential to reduce the number of unnecessary biopsies [221–227]. In [221], Pogue et al. presented a way of obtaining hemoglobin concentration, oxygen saturation, water fraction, scattering power, and scattering amplitude. These features were then investigated for their capability in differentiating benign and malignant tumors. In [222], Grosenick et al. reported on the diagnostic capability of the optical features, i.e., scattering and absorption coefficients, hemoglobin concentration, and blood oxygen saturation obtained using NIR spectroscopic techniques. The results showed that the optical features can be used to distinguish carcinoma from healthy breast tissue. Khayat et al. [223] presented classification results of optical features, oxyhemoglobin, deoxyhemoglobin, blood volume, lipid and water content, scattering and absorption coefficients, using optical tomography. The results showed the diagnostic capability of features extracted

from optical images to classify different types of breast lesions. Recently, Xu et al. [224] presented a study for breast cancer diagnosis using optical features obtained by a handheld NIR spectroscopy probe. 12 features related to blood oxygen saturation and total hemoglobin concentration are evaluated. The results showed that NIR features has the potential to differentiate between benign and malignant tumors with a high accuracy.

We presented the diagnostic capability of the features extracted from *in vivo* NIR spectroscopy data obtained from 116 patients with breast tumors [184,185]. *In vivo* data was collected from 44 patients with malignant and 72 patients with benign tumors. Three features, relative blood concentration, oxygen saturation and the size of the tumor, are used to diagnose benign and malignant tumors. The diagnostic capability of these features are evaluated using different classifiers including nearest mean, neural network, support vector machine, Parzen, and normal density-based classifiers. The area under the receiver operating characteristics curve of the nearest mean classifier using the three features yields 0.91. This result suggests that relative blood volume concentration and oxygenation desaturation can differentiate malignant and benign breast tumors with a relatively high precision.

1.2.5 Organization of the Thesis

The thesis is organized as follows: In Chapter 2, we present EKF for the modeling and analysis of ICG pharmacokinetics in cancerous tumors using, in Chapter 3, we present voxel-by-voxel reconstruction of pharmacokinetic-rate images of ICG for breast tumors, in Chapter 4, we present direct reconstruction of pharmacokinetic-rate images of optical fluorophores using optical boundary measurements, in Chapter 5, we present the evaluation of NIR optical features for breast cancer diagnosis using *in vivo* patient data, Chapter 6 presents our conclusion and future work.

CHAPTER 2
EKF for the Modeling and Analysis of ICG Pharmacokinetics in Cancerous Tumors using NIR Optical Methods

In this chapter, we investigate three different compartmental models for the ICG kinetics and determine the optimal model order, based on Bayesian information criteria. The three models capture the transportation of ICG between the vascular and extravascular compartments, including interstitial fluid region, parenchymal cell, intracellular binding site, and extravascular, extracellular spaces (EES). An extended Kalman filtering (EKF) framework is proposed to estimate the model parameters and ICG concentrations in different compartments.

The chapter is organized as follows: In Section 2.1, we present an overview about what ICG is, in Section 2.2, we present the two-, three- and four-compartment models for ICG pharmacokinetics in tissue. In Section 2.3, we present the state-space representation of the compartmental models; estimation of ICG pharmacokinetic parameters and ICG concentrations in the EKF framework; and an optimal model order selection criterion. In Section 2.4, we present the experimental results obtained from Fischer rat data.

2.1 Indocyanine Green

Many advances in dye development have accelerated within the past 4 years but the majority of studies investigating NIR fluorescent-contrast agents have been limited to indocyanine green (ICG) due to its low toxicity and FDA approval.

ICG an optical dye commonly used in retinopathy and hepatic diagnostics [44, 45, 98–102]. It is excited at 730 nm. ICG has strong affinity for blood proteins; in plasma, ICG is near-completely bound, primarily to albumin. Thus, although ICG itself has a molecular weight of 700 Da, its *in vivo* kinetics is similar to those of a 70 kDa molecule. Its kinetics is governed by the movement of albumin in

and between the vascular and extravascular region. After binding with albumin, the absorption peak of ICG is shifted to 805nm and fluorescence peak at stays at 830nm well within the diagnostic window of low tissue absorption [46, 47]. For human use, ICG is administered intravenously with a bolus injection; a typical dosage is 0.25mg/kg (dosage to body weight). ICG is a nonspecific, transient, and local vascularized contrast agent.

ICG is eliminated from the body primarily through the bile: ICG outside of the circulatory system is not available for removal until it returns to the system. The kinetics of this transition offers a possible route to non-invasively determining the leakiness of large molecules from the microvasculature; this permeability is characteristic of the poorly developed vasculature observed in angiogenesis. This increase in local microvasculature density also increases the magnitude of the signal from inter-capillary ICG.

2.2 ICG Pharmacokinetic Modeling Using NIR Measurements

There are some differences in the delivery of ICG between normal and cancerous vasculature. In normal tissue, ICG acts as a blood flow indicator in tight capillaries of normal vessels. However in tumors, ICG may act as a diffusible (extravascular) flow in the leaky capillary of cancer vessels. To investigate the validity of this hypothesis, one has to employ at least a two-compartment model composed of plasma and EES. Additionally, the permeability rate is expected to increase as the malignancy advances [96, 97]. Fig. 2.1 (a) and (b) illustrates the ICG flow for healthy and malignant tissue, respectively.

2.2.1 Compartmental Analysis of ICG Pharmacokinetics

Compartmental modeling allows relatively simple and effective mathematical representation of complex biological responses due to contrast agents. A region of interest is assumed to consist of a number of compartments, generally representing a volume or a group of similar tissues into which the contrast agent is distributed. The concentration change in a specific compartment is modeled as a result of the

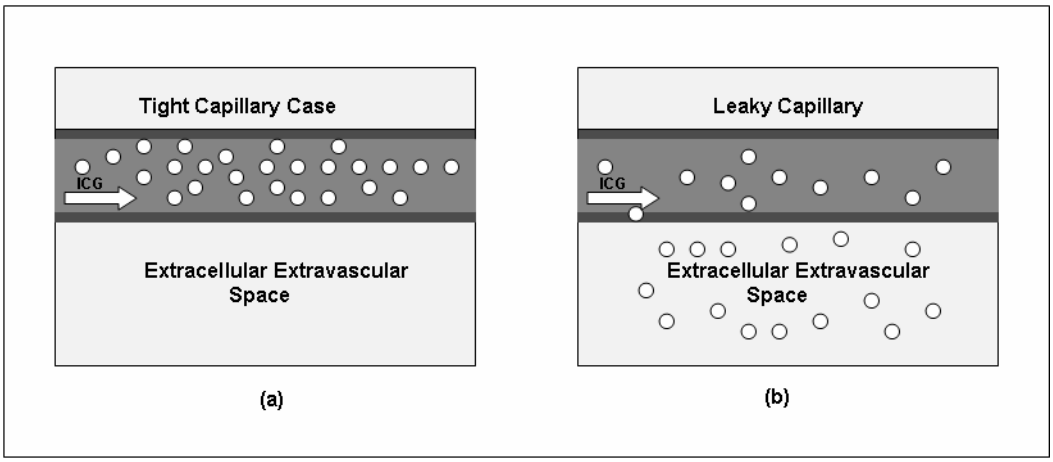

Figure 2.1: An illustration of the ICG flow (a) in tight capillary of normal vessel, (b) in permeable capillary of tumor tissue.

exchange of contrast agent between connected compartments. These changes are modeled by a collection of coupled ODEs; each equation describing the time change dictated by the biological laws that govern the concentration exchanges between the interacting compartments [50, 105, 187, 188].

2.2.1.1 The four-compartment model

Fig. 2.2 illustrates the capillary and extracapillary space relevant to the four compartment model. The four-compartment model includes capillary region, interstitial fluid region, parenchymal cell region and intracellular binding site as compartments [106]. The ICG, injected intravenously into the subject, can pass from the capillary into the reversible binding site inside the cell through the interstitial fluid region and the parenchymal cell region [106–108]. Moreover, in advanced tumor stages, the leakiness around the tumor vessels is expected to increase, resulting in higher permeability rates during the transportation of ICG into the compartments. A block diagram of the four-compartment transport and chemical model of ICG delivery is shown in Fig. 2.3(a).

Let C_p, C_i, C_{pc}, C_b denote the ICG concentrations in plasma, the interstitial fluid region, the parenchymal cell region and the intracellular binding site, respectively; and let $k_{out}^{(4)}$, $k_a^{(4)}$, $k_b^{(4)}$, $k_c^{(4)}$, $k_d^{(4)}$, $k_e^{(4)}$ and $k_f^{(4)}$ be the constants used as

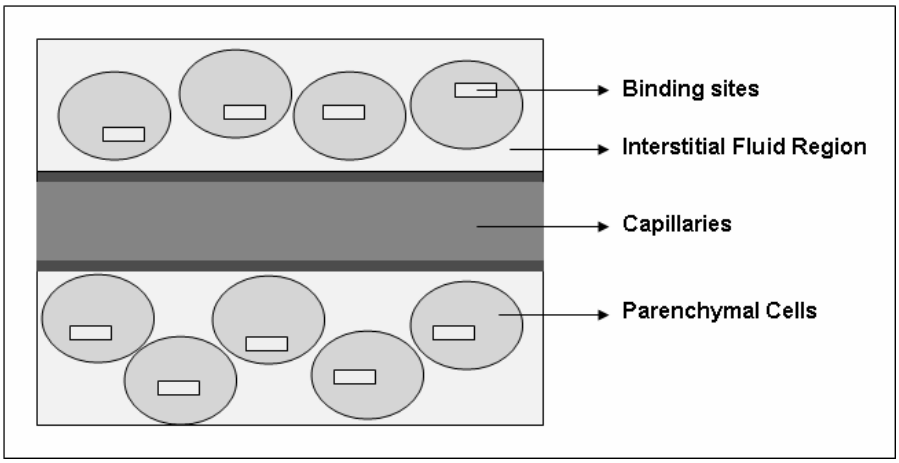

Figure 2.2: A simple illustration of the capillary extracapillary structure.

equilibrium coefficients as shown in Fig. 2.3(a). Then the set of differential equations representing the ICG transition between the four compartments is given as follows:

The leakage into and the drainage out of plasma:

$$\frac{dC_p(t)}{dt} = k_b^{(4)} C_i(t) - k_a^{(4)} C_p(t) - k_{out}^{(4)} C_p(t). \tag{2.1}$$

The leakage into and the drainage out of the interstitial fluid region:

$$\frac{dC_i(t)}{dt} = k_a^{(4)} C_p(t) - k_b^{(4)} C_i(t) - k_c^{(4)} C_i(t) + k_d^{(4)} C_{pc}(t). \tag{2.2}$$

The leakage into and the drainage out of the parenchymal cell:

$$\frac{dC_{pc}(t)}{dt} = k_c^{(4)} C_i(t) - k_d^{(4)} C_{pc}(t) - k_e^{(4)} C_{pc}(t) + k_f^{(4)} C_b(t). \tag{2.3}$$

The leakage into and the drainage out of the intracellular binding site:

$$\frac{dC_b(t)}{dt} = k_e^{(4)} C_{pc}(t) - k_f^{(4)} C_b(t). \tag{2.4}$$

Physiologically, the equilibrium constants are defined by the permeability surface area products given as $PS\rho$, where P is the capillary permeability constant, S is the

capillary surface area, and ρ is the tissue density. $k_{out}^{(4)}$ is proportional to the flow rate into and out of the capillary and $k_a^{(4)}$, $k_b^{(4)}$, $k_c^{(4)}$, $k_d^{(4)}$, $k_e^{(4)}$, and $k_f^{(4)}$ represent intra-tissue physiologic effects during ICG delivery from the capillary to the binding site. Note that the superscript denotes the order of the compartmental model.

The actual bulk ICG concentration in the tissue measured by NIR spectroscopy, $m(t)$, is a linear combination of the ICG concentrations in the four different compartments.

$$m(t) = v_p^{(4)} C_p(t) + v_i^{(4)} C_i(t) + v_{pc}^{(4)} C_{pc}(t) + v_b^{(4)} C_b(t), \tag{2.5}$$

where $v_p^{(4)}$, $v_i^{(4)}$, $v_{pc}^{(4)}$, $v_b^{(4)}$, are volume fractions of plasma, the interstitial fluid region, the parenchymal cell region and the intracellular binding site, respectively.

2.2.1.2 The three-compartment model

In this model, the parenchymal cell and intracellular binding site compartments are combined to form a single compartment called parenchymal cell. This amounts to the assumptions that the transport of ICG into the intracellular binding site is negligible as compared to the other compartments, and therefore omitted from the model. A block diagram of the three-compartment transport and chemical model of ICG delivery is shown in Fig. 2.3(b). The three-compartment transport equations are given as follows:

The leakage into and the drainage out of plasma:

$$\frac{dC_p(t)}{dt} = k_b^{(3)} C_i(t) - k_a^{(3)} C_p(t) - k_{out}^{(3)} C_p(t) \tag{2.6}$$

The leakage into and the drainage out of the interstitial space:

$$\frac{dC_i(t)}{dt} = k_a^{(3)} C_p(t) - k_b^{(3)} C_i(t) - k_c^{(3)} C_i(t) + k_d^{(3)} C_{pc}(t) \tag{2.7}$$

The leakage into and the drainage out of the parenchymal cell:

$$\frac{dC_{pc}(t)}{dt} = k_c^{(3)} C_i(t) - k_d^{(3)} C_{pc}(t) \tag{2.8}$$

The total ICG concentration measured by NIR:

$$m(t) = v_p^{(3)} C_p(t) + v_i^{(3)} C_i(t) + v_{pc}^{(3)} C_{pc}(t) \tag{2.9}$$

where $v_p^{(3)}$, $v_i^{(3)}$, $v_{pc}^{(3)}$ and C_p, C_i, C_{pc} are as defined in the four-compartment model.

2.2.1.3 The two-compartment model

In the two-compartment model, the tumor region is assumed to be composed of two compartments, namely the plasma and the extra-cellular extra-vascular space (EES) [96, 109, 110]. The EES is defined as the region that lies outside of both the vascular region and the tumor cells. The transport of the ICG to the third and fourth compartments are assumed to be negligible. Therefore the last two compartments in the four compartment model is omitted. We consider transcapillary leakage to occur only at the tumor site. We also assume that a small perturbation of the global plasma concentration does not affect the bulk removal. Fig. 2.3(c) shows the block diagram of the two-compartment model for the ICG kinetics. Let C_p and C_e denote the ICG concentrations in plasma and the EES, respectively. Then the two-compartment ICG chemical transport equations are given as follows:

The leakage into and the drainage out of plasma:

$$\frac{dC_p(t)}{dt} = k_b^{(2)} C_e(t) - k_a^{(2)} C_p(t) - k_{out}^{(2)} C_p(t). \tag{2.10}$$

The leakage into and the drainage out of the EES:

$$\frac{dC_e(t)}{dt} = k_a^{(2)} C_p(t) - k_b^{(2)} C_e(t). \tag{2.11}$$

The parameters $k_a^{(2)}$ and $k_b^{(2)}$ govern the leakage into and the drainage out of the EES, respectively. The parameter $k_{out}^{(2)}$ describes the ICG elimination from the body through kidneys and liver.

Actual bulk ICG concentration in the tissue measured by NIR is a linear combination of plasma and EES ICG concentrations given by:

$$m(t) = v_p^{(2)} C_p(t) + v_e^{(2)} C_e(t), \tag{2.12}$$

where the parameters $v_p^{(2)}$ and $v_e^{(2)}$ denote the plasma and EES volume fractions, respectively.

2.3 Extended Kalman Filtering for the ICG Pharmacokinetics

For the rest of our discussion in this chapter, we shall use the explicit form of the two-compartment model as a running example to clarify our notation. Note that for the rest of the paper, all matrices and vectors will be in boldface and scalar quantities will be in non-boldface notation.

2.3.1 State-space Representation of the ICG Pharmacokinetics

Coupled differential equations resulting from the two-compartment modeling of the ICG pharmacokinetics can be expressed in state-space representation as follows:

$$\begin{bmatrix} dC_e(t) \\ dC_p(t) \end{bmatrix} = \begin{bmatrix} -k_b^{(2)} & k_a^{(2)} \\ k_b^{(2)} & -(k_a^{(2)} + k_{out}^{(2)}) \end{bmatrix} \begin{bmatrix} C_e(t) \\ C_p(t) \end{bmatrix} + d\mathbf{B}(t), \tag{2.13}$$

$$m(t) = \begin{bmatrix} v_e^{(2)} & v_2^{(2)} \end{bmatrix} \begin{bmatrix} C_e(t) \\ C_p(t) \end{bmatrix} + \eta(t)$$

where $d\mathbf{B}(t)$ is the Wiener process increment, $d\mathbf{B}(t) = \boldsymbol{\omega}(t)dt$. Here, $\boldsymbol{\omega}(t)$and $\eta(t)$ can be thought of as uncorrelated zero mean Gaussian processes with covariance matrix $\mathbf{Q}$, and variance σ^2, respectively.

In vector-matrix notation, the continuous time state-space representation for the $n-$compartment model is given by:

$$d\mathbf{C}(t) = \boldsymbol{\kappa}(\boldsymbol{\alpha}_n)\mathbf{C}(t)dt + d\mathbf{B}(t),$$

$$m(t) = \mathbf{V}(\boldsymbol{\alpha}_n)\mathbf{C}(t) + \eta(t). \tag{2.14}$$

In (2.14), $\mathbf{C}(t)$ denotes the concentration vector; $\boldsymbol{\kappa}(\boldsymbol{\alpha}_n)$ is the system matrix, $\mathbf{V}(\boldsymbol{\alpha}_n)$ is the measurement matrix and $\boldsymbol{\alpha}_n$ is the parameter vector whose elements are the pharmacokinetic constants and the volume fractions for the $n-$compartment model. For example the parameter vector $\boldsymbol{\alpha}_2$ for the two-compartment model is given by

$$\boldsymbol{\alpha}_2 = [k_a^{(2)} \;\; k_b^{(2)} \;\; k_{out}^{(2)} \;\; v_e^{(2)} \;\; v_p^{(2)}]. \tag{2.15}$$

The ICG measurements in (2.14) are collected at discrete time instances, $t = kT$, $k = 0, 1, ...$, where T is the sampling period. Therefore, the continuous model described in (2.14) has to be discretized. To simplify our notation, we shall use $\mathbf{C}(k) = \mathbf{C}(kT)$ and $m(k) = m(kT)$. The discrete state space system and the measurement models are given as follows:

$$\mathbf{C}(k+1) = \boldsymbol{\kappa}_d(\boldsymbol{\alpha}_n)\mathbf{C}(k) + \boldsymbol{\omega}(k)$$

$$m(k) = \mathbf{V}_d(\boldsymbol{\alpha}_n)\mathbf{C}(k) + \eta(k), \tag{2.16}$$

where $\boldsymbol{\kappa}_d(\boldsymbol{\alpha}_n) = e^{\boldsymbol{\kappa}(\boldsymbol{\alpha}_n)T}$ is the discrete-time system matrix and $V_d(\boldsymbol{\alpha}_n) = V(\boldsymbol{\alpha}_n)$ is the discrete-time measurement matrix. $\boldsymbol{\omega}(k)$ and $\eta(k)$ are zero mean Gaussian white noise processes with covariance matrix $\mathbf{Q}_d$ and variance σ_d^2, respectively. Discretization of state-space models can be found in various system theory books, see for example [111].

An explicit form of the discrete state space model for the two-compartment case is given as follows:

$$\begin{bmatrix} C_e(k+1) \\ C_p(k+1) \end{bmatrix} = \begin{bmatrix} \tau_{11} & \tau_{12} \\ \tau_{21} & \tau_{22} \end{bmatrix} \begin{bmatrix} C_e(k) \\ C_p(k) \end{bmatrix} + \boldsymbol{\omega}(k) \tag{2.17}$$

$$m(k) = \begin{bmatrix} v_e^{(2)} & v_p^{(2)} \end{bmatrix} \begin{bmatrix} C_e(k) \\ C_p(k) \end{bmatrix} + \eta(k),$$

where τ_{ij} is the i^{th} row and j^{th} column entry of the system matrix $\boldsymbol{\kappa}_d(\boldsymbol{\alpha}_2)$. Note that the matrix entry τ_{ij} is an exponential function of the parameters $k_a^{(2)}$, $k_b^{(2)}$ and

$k_{out}^{(2)}$.

To simplify the estimation process, we shall first estimate the matrix entries, τ_{ij}, of the discrete-time system matrix $\boldsymbol{\kappa}_d(\boldsymbol{\alpha}_n)$ and then compute the pharmacokinetic parameters for each compartmental model.

2.3.2 Modeling of ICG Pharmacokinetic Parameters and Concentrations in an Extended Kalman Filter Framework

The Kalman filter provides a recursive method to estimate the states in state-space models, in which the states are driven by noise, and the measurements are collected in the presence of measurement noise [112, 114, 191]. In the case of non-linear state-space models, the extended Kalman filter linearizes the model around the current state estimate, and then applies the KF to the resulting linear model. The EKF framework is also utilized for the joint estimation of the unknown system and/or measurement parameters and states. In a linear state-space model when both states and system parameters are unknown, the linear state-space model can be regarded as a non-linear model in which the linear system parameters and states are combined to form the new states of the non-linear model. This system is then linearized and solved for the unknown states using the KF estimator. We consider a linear Taylor approximation of the non-linear model. The details of the linearization procedure and a general discussion on EKF can be found in [115–117, 191].

In our problem, the objective is to simultaneously estimate the states, i.e., the ICG concentrations in each compartment, and the system and measurement parameters, i.e., the pharmacokinetic parameters and the volume fractions. Let $\boldsymbol{\theta}_n$ denote the discrete-time parameter vector of the pharmacokinetic rates and volume fractions. For example, in the two-compartment model, $\boldsymbol{\theta}_2$ is given by

$$\boldsymbol{\theta}_2 = \begin{bmatrix} \tau_{11} & \tau_{12} & \tau_{21} & \tau_{22} & v_e^{(2)} & v_p^{(2)} \end{bmatrix}^T. \tag{2.18}$$

Note that the parameter vector $\boldsymbol{\theta}_n$, derived from the state space model (2.17), is time independent. In order to estimate $\boldsymbol{\theta}_n$ within the EKF framework, the fol-

lowing dynamic model is introduced:

$$\boldsymbol{\theta}_n(k+1) = \boldsymbol{\theta}_n(k) + \boldsymbol{\varsigma}(k), \tag{2.19}$$

where $\boldsymbol{\varsigma}(k)$ is a zero mean white noise process with covariance matrix $\mathbf{S}_d$ [191]. Here, $\boldsymbol{\theta}_n(k)$ can be thought of as the k^{th} update of the parameter rather than its value at time k.

We append the parameter vector $\boldsymbol{\theta}_n(k+1)$ to the ICG concentration vector $\mathbf{C}(k+1)$ to form the new non-linear state-space model given by

$$\begin{bmatrix} \mathbf{C}(k+1) \\ \boldsymbol{\theta}_n(k+1) \end{bmatrix} = \begin{bmatrix} \mathbf{K}(\boldsymbol{\theta}_n)\mathbf{C}(k) \\ \boldsymbol{\theta}_n(k) \end{bmatrix} + \begin{bmatrix} \boldsymbol{\omega}(k) \\ \boldsymbol{\varsigma}(k) \end{bmatrix} \tag{2.20}$$

$$m(k) = \begin{bmatrix} \mathbf{V}_d(\boldsymbol{\theta}_n) & 0 \end{bmatrix} \begin{bmatrix} \mathbf{C}(k) \\ \boldsymbol{\theta}_n(k) \end{bmatrix} + \eta(k),$$

where $\mathbf{K}(\theta_n) = \boldsymbol{\kappa}_d(\boldsymbol{\alpha}_n)$.

2.3.3 EKF Joint Estimation of ICG Concentrations, Pharmacokinetic Parameters, and Volume Fractions

In this section we will summarize the major steps of the EKF estimator for the joint estimation of ICG concentrations and compartmental model parameters.

Let the subscript $k|t$ denote the estimate at time k given all the measurements up to time t. Then the 1-step ahead prediction of the ICG concentrations and the compartmental model parameters are given as follows:

$$\begin{bmatrix} \hat{\mathbf{C}} \\ \hat{\boldsymbol{\theta}_n} \end{bmatrix}_{k|k-1} = \begin{bmatrix} \mathbf{K}(\hat{\boldsymbol{\theta}_n})\hat{\mathbf{C}} \\ \hat{\boldsymbol{\theta}_n} \end{bmatrix}_{k-1|k-1}. \tag{2.21}$$

For the two-compartment model, (2.21) becomes

$$\begin{bmatrix} \hat{C}_e \\ \hat{C}_p \\ \hat{\boldsymbol{\theta}}_2 \end{bmatrix}_{k|k-1} = \begin{bmatrix} \hat{\tau_{11}}\hat{C}_e + \hat{\tau_{12}}\hat{C}_p \\ \hat{\tau_{21}}\hat{C}_e + \hat{\tau_{22}}\hat{C}_p \\ \hat{\boldsymbol{\theta}}_2 \end{bmatrix}_{k-1|k-1} . \tag{2.22}$$

The error covariance matrix, $\mathbf{P}_{k|k-1}$, of the 1-step ahead predictions is given as follows:

$$\mathbf{P}_{k|k-1} = \mathbf{J}_{k-1}\mathbf{P}_{k-1|k-1}\mathbf{J}_{k-1}^T + \begin{bmatrix} \mathbf{Q}_d & 0 \\ 0 & \mathbf{S}_d \end{bmatrix}, \tag{2.23}$$

where $\mathbf{J}_k$ is the Jacobian of the non-linear EKF system function at time k. Explicitly, it is given by:

$$\mathbf{J}_k = \begin{bmatrix} \mathbf{K}(\hat{\boldsymbol{\theta}}_n) & \frac{\partial}{\partial \hat{\boldsymbol{\theta}}_n}[\mathbf{K}(\hat{\boldsymbol{\theta}}_n)\hat{\mathbf{C}}] \\ \mathbf{0} & \mathbf{I} \end{bmatrix}_{k|k}, \tag{2.24}$$

where $\mathbf{0}$ and $\mathbf{I}$ denote zero and identity matrices, respectively. The Jacobian matrix for the two-compartment model becomes

$$\mathbf{J}_k = \begin{bmatrix} \begin{pmatrix} \hat{\tau_{11}} & \hat{\tau_{12}} \\ \hat{\tau_{21}} & \hat{\tau_{22}} \end{pmatrix} & \begin{pmatrix} \hat{C}_e & \hat{C}_p & 0 & 0 & 0 & 0 \\ 0 & 0 & \hat{C}_e & \hat{C}_p & 0 & 0 \end{pmatrix} \\ \mathbf{0}_{(6\times 2)} & \mathbf{I}_{(6\times 6)} \end{bmatrix}_{k|k}, \tag{2.25}$$

where $\mathbf{0}_{(6\times 2)}$ is a 6×2 zero matrix, and $\mathbf{I}_{(6\times 6)}$ is a 6×6 identity matrix.

The 1-step ahead predictions are updated to the k^{th}-step estimates by means of the Kalman gain matrix which is given by

$$\mathbf{G}_k = \mathbf{P}_{k|k-1}\boldsymbol{\Lambda}^T[\boldsymbol{\Lambda}\mathbf{P}_{k|k-1}\boldsymbol{\Lambda}^T + \sigma_k^2]^{-1}, \tag{2.26}$$

where $\boldsymbol{\Lambda}$ is the following vector

$$\begin{bmatrix} \mathbf{V}_d(\hat{\boldsymbol{\theta}}) & \frac{\partial}{\partial \hat{\boldsymbol{\theta}}}[\mathbf{V}_d(\hat{\boldsymbol{\theta}})\hat{\mathbf{C}}] \end{bmatrix}_{k|k-1}. \tag{2.27}$$

For the two-compartment model the $\mathbf{\Lambda}$ vector becomes

$$\left[\begin{array}{cccccccc} \hat{v_e}^{(2)} & \hat{v_p}^{(2)} & 0 & 0 & 0 & 0 & \hat{C}_e & \hat{C}_p \end{array} \right]_{k|k-1}. \tag{2.28}$$

The k^{th}-step estimate of the concentrations and the parameters are obtained recursively using

$$\left[\begin{array}{c} \hat{\mathbf{C}} \\ \hat{\boldsymbol{\theta}} \end{array} \right]_{k|k} = \left[\begin{array}{c} \hat{\mathbf{C}} \\ \hat{\boldsymbol{\theta}} \end{array} \right]_{k|k-1} + \mathbf{G}_k(m(k) - [\mathbf{V}_d(\hat{\boldsymbol{\theta}})\hat{\mathbf{C}}]_{k|k-1}). \tag{2.29}$$

For the two-compartment case, the k^{th}-step estimate of the concentrations and the parameters is

$$\left[\begin{array}{c} \hat{C}_e \\ \hat{C}_p \\ \hat{\boldsymbol{\theta}}_2 \end{array} \right]_{k|k} = \left[\begin{array}{c} \hat{C}_e \\ \hat{C}_p \\ \hat{\boldsymbol{\theta}}_2 \end{array} \right]_{k|k-1} + \mathbf{G}_k(m(k) - (\hat{v_e}^{(2)}\hat{C}_e - \hat{v_p}^{(2)}\hat{C}_p)_{k|k-1})). \tag{2.30}$$

The error covariance matrix, $\mathbf{P}_{k|k}$, of the k^{th}-step estimates is updated as

$$\mathbf{P}_{k|k} = [\mathbf{I} - \mathbf{G}_k\mathbf{\Lambda}]\mathbf{P}_{k|k-1}, \tag{2.31}$$

where $\mathbf{I}$ is the identity matrix.

In general, the convergence of EKF depends on proper choices of the initial values of the parameters, $\boldsymbol{\theta}$, initial values of the concentrations, $\mathbf{C}$, and proper selection of the noise covariance matrices $\mathbf{S}_d$, $\mathbf{Q}_d$, and the variance σ_d^2 [171]. The parameter σ_d^2 controls the convergence of the Kalman gain $\mathbf{G}_k$. To ensure stability, we set σ_d^2 much higher than the $\mathbf{\Lambda}P_{k|k-1}\mathbf{\Lambda}^T$ term in (2.26). However, setting very high values of σ_d^2 leads to slow convergence of the Kalman gain $\mathbf{G}_k$. The main cause of divergence in EKF can be tracked down to the fact that a change in the parameter vector has no direct effect on the Kalman gain; in other words, there is no coupling term between the Kalman gain and the parameter vector [172]. Based on this observation, we improved the convergence of the EKF by modifying the term

$\mathbf{J}(1,2) = \frac{\partial}{\partial \boldsymbol{\theta}}\mathbf{K}(\hat{\boldsymbol{\theta}})\hat{\mathbf{C}}$ in (2.24), as described in [172].

It has been shown that if $\mathbf{Q}_d$, $\mathbf{S}_d$ and σ_d^2 are selected less than the actual values, it leads to overconfidence in the accuracy of the estimates of the error covariance matrix [170]. Therefore, we regarded these matrices as tuning parameters and not as the estimates of the true covariance matrices, as suggested in [170].

Theoretically, the state estimates can be initialized at the expected value of the ICG concentrations, i.e. $E[\mathbf{C}(0)]$. One approach to the initialization of the parameters is to utilize the state-space presentation given in (2.16). Since $E(m(0)) = \mathbf{V}_d(\boldsymbol{\theta}_n(0))E[\mathbf{C}(0)]$, $m(0) - \mathbf{V}_d(\boldsymbol{\theta}_n(0))E[\mathbf{C}(0)]$ is a zero mean random variable. If we express the variance of the measurement $m(0)$ in terms of the variance of $\mathbf{C}(0)$ using the measurement model in (2.16), and solve for $\boldsymbol{\theta}_n$, we get the estimate $\hat{\boldsymbol{\theta}}_n(0)$ as the most appropriate value for initialization. The details of the selection of the initial values for the parameters can be found in [191].

The initialization of the error covariance matrix is also important for the performance of the EKF. The error covariance matrix is the matrix which provides information about the error bounds for the estimates. Theoretically, the initial error covariance matrix is a diagonal matrix where the diagonal entries are the initial estimates of the variance of concentrations and pharmacokinetic parameters, i.e.

$$\mathbf{P}_{0|0} = \begin{bmatrix} Cov(\mathbf{C}(0)) & 0 \\ 0 & \mathbf{S}_d \end{bmatrix}. \tag{2.32}$$

In depth discussion on the convergence properties of the EKF can be found in [170–172, 191].

2.3.4 Compartmental Model Order Selection

We adopted the Bayesian information criterion (BIC) for the optimal model order selection. BIC is a well known information theoretic criterion, in which the optimal model order is selected by minimizing a cost function to avoid over-fitting. The cost function depends on the number of observations, the number of unknown parameters to be estimated and the likelihood function. A detailed discussion of the BIC can be found in [121–123].

In order to calculate the BIC for different compartmental models, we first derived a likelihood function for the extended Kalman filter. The derivation is based on maximum likelihood estimation of the parameters in the Kalman filtering framework given as in [124], [125]. We then modified this likelihood function for the extended Kalman filter estimator for the joint estimation of compartmental model parameters and concentrations.

The cost function for the BIC is given by

$$\phi_{BIC}(p) = p \ln N - 2 \ln L(\boldsymbol{\theta}_p, m(1), m(2), ..., m(N)), \tag{2.33}$$

where p is the dimension of $\boldsymbol{\theta}_p$, which is related to the number of compartments in the model, N is the data length, and $L(\boldsymbol{\theta}, m(1), m(2), ..., m(N))$ is the likelihood function.

The likelihood function for the EKF is given by

$$L(\boldsymbol{\theta}, m(1), m(2), ..., m(N)) = -\frac{1}{2}\sum_{k=1}^{N} \ln[\det(\mathbf{H}_k)] - \frac{1}{2}\sum_{k=1}^{N} \mathbf{A}_k^T \mathbf{H}_k^{-1} \mathbf{A}_k, \tag{2.34}$$

where the matrix $\mathbf{H}$ is defined as:

$$\mathbf{H}_k = \Lambda \mathbf{P}_{k|k-1} \mathbf{\Lambda}^T + \sigma_k^2, \tag{2.35}$$

and σ_k^2, $\mathbf{\Lambda}$, and $\mathbf{P}_{k|k-1}$ are as defined in Section 2.3.3. The vector $\mathbf{A}$ is defined as:

$$\mathbf{A}_k = m(k) - [V_d(\hat{\boldsymbol{\theta}})\hat{\mathbf{C}}]_{k|k-1}, \tag{2.36}$$

where $m(k)$ is the ICG concentration data collected from Fisher rats at time k, and $[\mathbf{V}_d(\hat{\boldsymbol{\theta}})\hat{\mathbf{C}}]_{k|k-1}$ is the 1-step ahead estimate of the volume fractions and concentrations. The explicit form of the likelihood function for BIC calculation is given by

$$L(\boldsymbol{\theta}, m(1), ..., m(N)) = -\frac{1}{2}\sum_{k=1}^{N} \ln[\det(\mathbf{\Lambda} \mathbf{P}_{k|k-1} \mathbf{\Lambda}^T + \sigma_k^2)]$$

$$-\frac{1}{2}\sum_{k=1}^{N}[m(k)-[\mathbf{V}_d(\hat{\boldsymbol{\theta}})\hat{\mathbf{C}}]_{k|k-1}]^T[\boldsymbol{\Lambda}\mathbf{P}_{k|k-1}\boldsymbol{\Lambda}^T+\sigma_k^2]^{-1} .[m(k)-[\mathbf{V}_d(\hat{\boldsymbol{\theta}})\hat{\mathbf{C}}]_{k|k-1}]. \quad (2.37)$$

where all the parameters and matrices are as defined in Section 2.3.3.

2.4 Experimental Results - ICG Pharmacokinetics in Fischer Rat Data

We applied the proposed EKF framework to the pharmacokinetic analysis of ICG data obtained from four Fischer rats with adenocarcinoma. R3230ac adenocarcinoma cells were injected below the skin into four Fischer rats 3 weeks prior to measurements. The tumor size for the rats varies in diameter from 5 to 30 mm. Measurements were conducted with a combined frequency-domain and steady-state optical technique that facilitates rapid measurement of tissue absorption. Frequency domain measurements were obtained at 674, 800, 849, 898, and 915 nm, modulated at frequencies from 50 to 601 MHz, sweeping a total of 233 frequencies. Tumors were also imaged by use of contrast-enhanced magnetic resonance imaging and co-registered with the location of the optical probe. In addition, a broadband continuous wave reflectance measurement spanning the range 650-1000 nm was performed with a spectrometer. With the reduced-scattering coefficient spectrum and diffusion theory, the broadband reflectance spectra were converted to absorption coefficient spectra. The absolute concentration of ICG, together with oxy-hemoglobin, deoxy-hemoglobin, and water were calculated by using multiple linear regressions of ICG extinction coefficient spectra to the calculated absorption spectrum at approximately every second for ten minutes. A detailed discussion of the measurement process and apparatus can be found in [126, 127].

Fig. 2.4 presents the ICG concentrations (μM) from four different rats. Tumors in Rat 1 and 2 are classified as necrotic because of their low tissue oxy-hemoglobin, low total hemoglobin, and low gadolinium-diethylene-triamine pentaacetic acid (Gd-DTPA) enhancement levels. Tumors in Rat 3 and 4 are classified as edematous due to their high water content [128]. It can be observed from Fig. 2.4

that the necrotic cases display low peak ICG concentration values and slowly rising slopes unlike the edematous cases with high peak values and sharp rising slopes.

We estimated the pharmacokinetic rates for the four-, three- and two-compartment models. Each data set has 504 measurements. The reported parameter estimates are the asymptotic values obtained when the extended Kalman filter has converged. In other words, the predicted parameter values corresponding to the final estimate, i.e., $k_a^2 = k_{a,\ (k=504)}^2$.The results are given in Tables 2.1, 2.2, and 2.3, respectively. The error bounds on the estimates are derived from the covariance matrix of the EKF estimator. The estimated pharmacokinetic rates for all compartmental models indicate that the exchange rates between the capillary and the adjacent compartment (ISS or EES), k_a^n, k_b^n, $n = 2, 3, 4$, are significantly different for the necrotic and edematous tissue. We observe that for the four- and three-compartment models, the estimated exchange rates between the ISS and parenchymal cell compartments, k_c^n, k_d^n, $n = 3, 4$, are comparable. Similarly, the estimated rate of drainage out of the plasma, k_{out}^n, $n = 2, 3, 4$, are consistent for all models.

Based on the model parameter estimates, we computed the BIC values for each rat data to reveal over-fitting. The BIC values and the number of unknown parameters for each rat data are tabulated in Table 2.4. The BIC suggests that the two-compartment model is sufficient for all four measurement sets.

We further analyze the goodness-of-fit of the compartmental models by means of residual analysis. The basic idea of residual analysis is to compare the actual measurements $m(k)$ with their 1-step ahead predictions, $\hat{m}(k)_{k|k-1}$, based on the estimated parameters. A detailed discussion on residual analysis can be found in [112, 129]. The mean and variance of the residual error for the four-, three- and two-compartmental models are tabulated in Table 2.5. To normalize the error with respect to the magnitude of the actual measurements, we calculated the signal-to-noise ratio (SNR) using the median value of the measurements and the mean of the residual errors for each rat data. As seen from the results in Table 2.6, the SNR values are higher for the two-compartment case for all data sets. These results show that the two-compartment model provides the minimum bias and the best statistical efficiency. Fig. 2.5 shows the measured total concentration data and its 1-step ahead

Table 2.1: Four-Compartment Model:Estimated pharmacokinetic parameters using EKF algorithm

	$k_a^{(4)}$ $(sec^{-1}10^{-2})$	$k_b^{(4)}$ $(sec^{-1}10^{-2})$	$k_c^{(4)}$ $(sec^{-1}10^{-2})$	$k_d^{(4)}$ $(sec^{-1}10^{-2})$
Rat 1 (Necrotic)	1.45±0.013	1.22±0.019	1.86±0.017	2.02±0.026
Rat 2 (Necrotic)	3.48±0.048	2.77±0.034	4.28±0.048	4.33±0.040
Rat 3 (Edematous)	4.94±0.052	5.16±0.067	4.22±0.052	4.13±0.067
Rat 4 (Edematous)	5.25±0.053	5.31±0.063	5.07±0.068	5.22±0.063

	$k_e^{(4)}$ $(sec^{-1}10^{-2})$	$k_f^{(4)}$ $(sec^{-1}10^{-2})$	$k_{out}^{(4)}$ $(sec^{-1}10^{-3})$
Rat 1 (Necrotic)	2.74±0.041	2.41±0.051	4.05±0.059
Rat 2 (Necrotic)	2.98±0.048	3.03±0.061	4.76±0.062
Rat 3 (Edematous)	4.14±0.070	4.27±0.078	5.39±0.085
Rat 4 (Edematous)	4.43±0.075	4.03±0.072	3.85±0.056

Table 2.2: Three-compartment Model:Estimated pharmacokinetic parameters using EKF algorithm

	$k_a^{(3)}$ $(sec^{-1}10^{-2})$	$k_b^{(3)}$ $(sec^{-1}10^{-2})$	$k_c^{(3)}$ $(sec^{-1}10^{-2})$	$k_d^{(3)}$ $(sec^{-1}10^{-2})$	$k_{out}^{(3)}$ $(sec^{-1}10^{-3})$
Rat 1 (Necrotic)	1.93±0.061	1.28±0.049	1.82±0.032	2.02±0.041	3.89±0.052
Rat 2 (Necrotic)	4.41±0.074	2.48±0.067	4.87±0.066	5.03±0.057	5.45±0.071
Rat 3 (Edematous)	4.71±0.085	3.88±0.077	4.95±0.059	4.68±0.050	4.42±0.040
Rat 4 (Edematous)	5.29±0.091	6.48±0.096	4.48±0.062	4.20±0.048	5.01±0.055

Table 2.3: Two-compartment Model:Estimated pharmacokinetic parameters and volume fractions using EKF algorithm

	$k_a^{(2)}$ $(sec^{-1}10^{-2})$	$k_b^{(2)}$ $(sec^{-1}10^{-2})$	$k_{out}^{(2)}$ $(sec^{-1}10^{-3})$	$v_e^{(2)}$ (10^{-2})	$v_p^{(2)}$ (10^{-2})
Rat 1 (Necrotic)	2.47±0.043	1.06±0.052	4.61±0.073	21.8±1.92	1.41±0.053
Rat 2 (Necrotic)	3.54±0.082	2.98±0.086	4.83±0.092	25.4±3.49	2.42±0.088
Rat 3 (Edematous)	6.90±0.101	4.93±0.072	3.95±0.048	30.4±2.81	4.84±0.120
Rat 4 (Edematous)	8.40±0.114	7.77±0.091	4.02±0.068	53.0±4.73	7.03±0.321

Table 2.4: Test for model order selection for three different compartmental models for four different data sets

		Rat1	**Rat2**	**Rat3**	**Rat4**
Model	p	$\phi_{BIC}(p)$	$\phi_{BIC}(p)$	$\phi_{BIC}(p)$	$\phi_{BIC}(p)$
Two-compartment Model	7	-178.242	-198.367	-202.81	-172.098
Three-compartment Model	11	-71.615	-83.849	-92.182	-63.912
Four-compartment Model	15	-39.719	-45.121	-56.340	-30.023

prediction based on the two-compartment model for each rat data. Clearly, there is a good agreement between the actual and the predicted values.

Based on the BIC and residual analysis, we conclude that the two-compartment model provides the best statistical fit for the rat data and investigate the estimated model parameters in more detail.

In the two-compartment model, the rate of leakage into the EES from the capillary, $k_a^{(2)}$, range from 0.0247 to 0.0840 sec^{-1} and the rate of drainage out of the EES and into the capillary, $k_b^{(2)}$, range from 0.0106 to 0.0777 sec^{-1}. Note that the permeability rates for the necrotic cases are lower than the ones observed for the edematous cases. Additionally, the estimated values for the pharmacokinetic rates are much higher than the normal tissue values due to the increased leakiness of the blood vessels around the tumor region [96, 130]. The estimated plasma volume fractions agrees with the values reported earlier [96], and the values presented in the literature [131, 132]. These results confirm that $v_p^{(2)}$ can be large in tumors and that its magnitude varies with respect to the stage of the tumor [110]. The estimated values of the EES volume fraction, $v_e^{(2)}$, range from 0.218 to 0.53, in agreement with the 0.2 to 0.5 range reported earlier [109]. Note that these results are valid only for the ICG pharmacokinetics in tumor cells R3230ac, adenocarcinoma and may not be generalized for other types of contrast agents or tumor types.

Fig. 2.6 shows the estimated ICG concentrations in plasma and the EES compartments for the two-compartment model for Rats 1 to 4. Note that the concentration curves in Fig. 2.5 and Fig. 2.6 follow a similar time course since the curves in Fig. 2.6 is a linear combination of the curves in Fig. 2.5. Note that initial estimates of concentrations are noisy due to the limited data used in the recursive

Table 2.5: The mean and variance of the error between the estimates and measurements

	Four-compartment		**Three-compartment**		**Two-compartment**	
	Mean	Variance	Mean	Variance	Mean	Variance
Rat1	0.0987	7.641e-004	0.0605	4.732e-004	0.0072	2.567e-005
Rat2	0.1043	9.152e-004	0.0767	3.017e-004	0.0057	4.829e-005
Rat3	0.1204	8.905e-004	0.0883	4.921e-004	0.0041	3.021e-005
Rat4	0.0904	5.977e-004	0.0589	6.839e-004	0.0076	8.618e-005

Table 2.6: SNR values for three different compartmental models for four different data sets

	Rat1	**Rat2**	**Rat3**	**Rat4**
Model	SNR (dB)	SNR (dB)	SNR (dB)	SNR (dB)
Two-compartment Model	73.2	68.1	108.3	107.9
Three-compartment Model	30.7	36.1	23.9	47.0
Four-compartment Model	20.8	29.9	27.7	18.4

EKF estimation. This can be improved by Kalman backward smoothing [133]. The peak values of the plasma concentration, C_p, range from 2.72 μM to 4.28 μM. The absolute value of the concentrations may not be very useful. However, concentration of ICG in a compartment relative to the one in another compartment may provide useful information. We consider the ratio of the peak concentrations in plasma and the EES as a potential parameter to discriminate different tumors. The peak C_p/C_e ratio for Rats 1 to 4 is 0.551, 0.593, 0.787, 1.151, respectively. This ratio is higher in edematous cases consistent with the fact that ICG-albumin leaks more into the EES in edematous tumors. Additionally, the ICG concentration in plasma decays faster than the ICG concentration in the EES due to its elimination through the liver and kidneys.

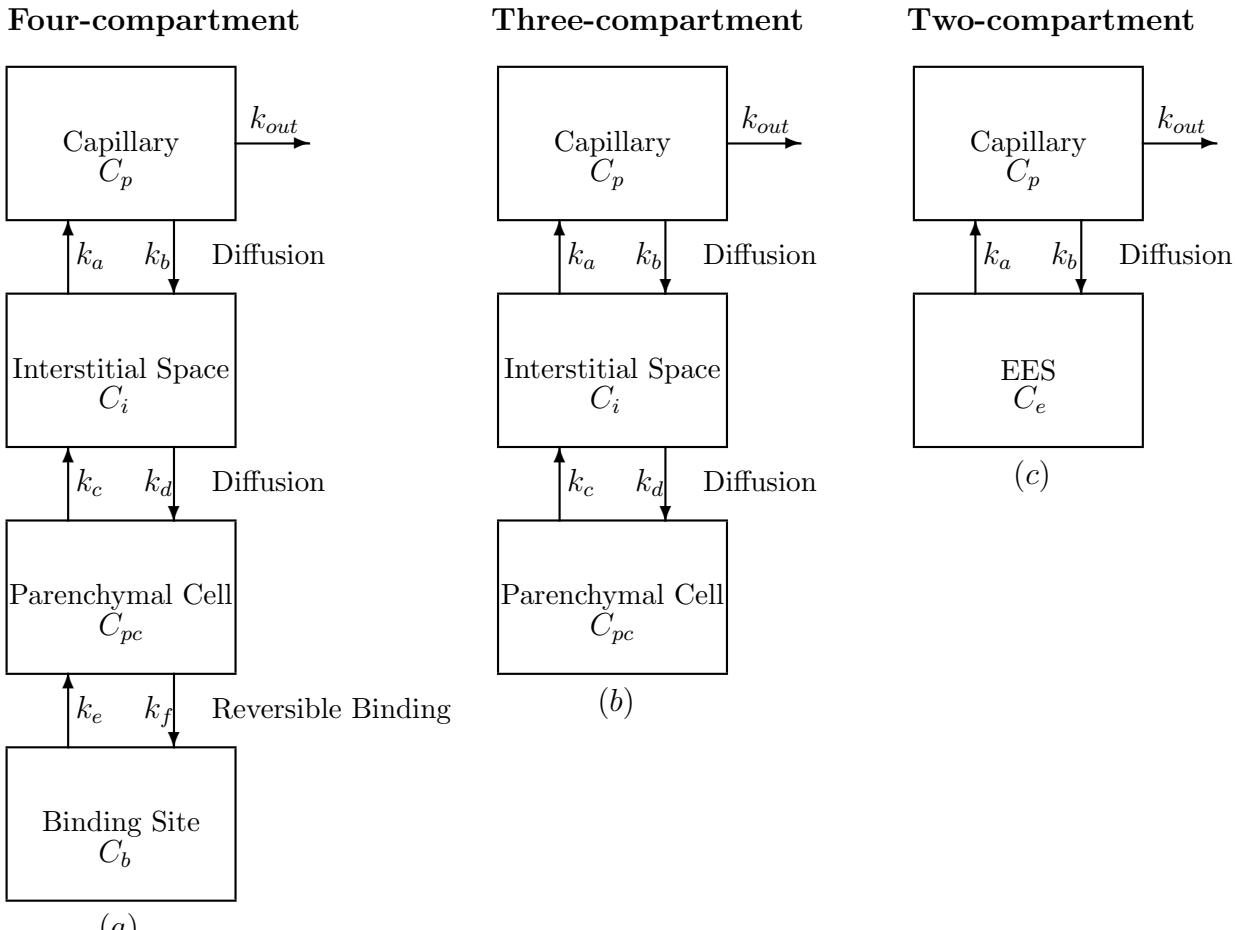

Figure 2.3: Block diagram of (a) the four-compartment, (b) the three-compartment, and (c) the two-compartment models for ICG pharmacokinetics.

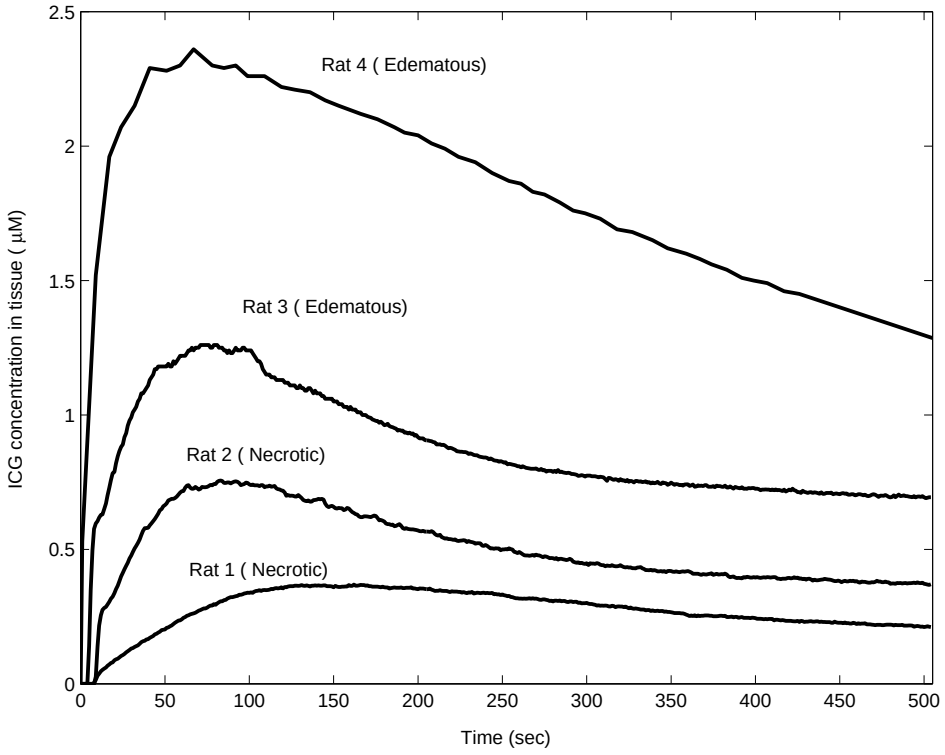

Figure 2.4: ICG concentrations measured in tissue for four different rats.

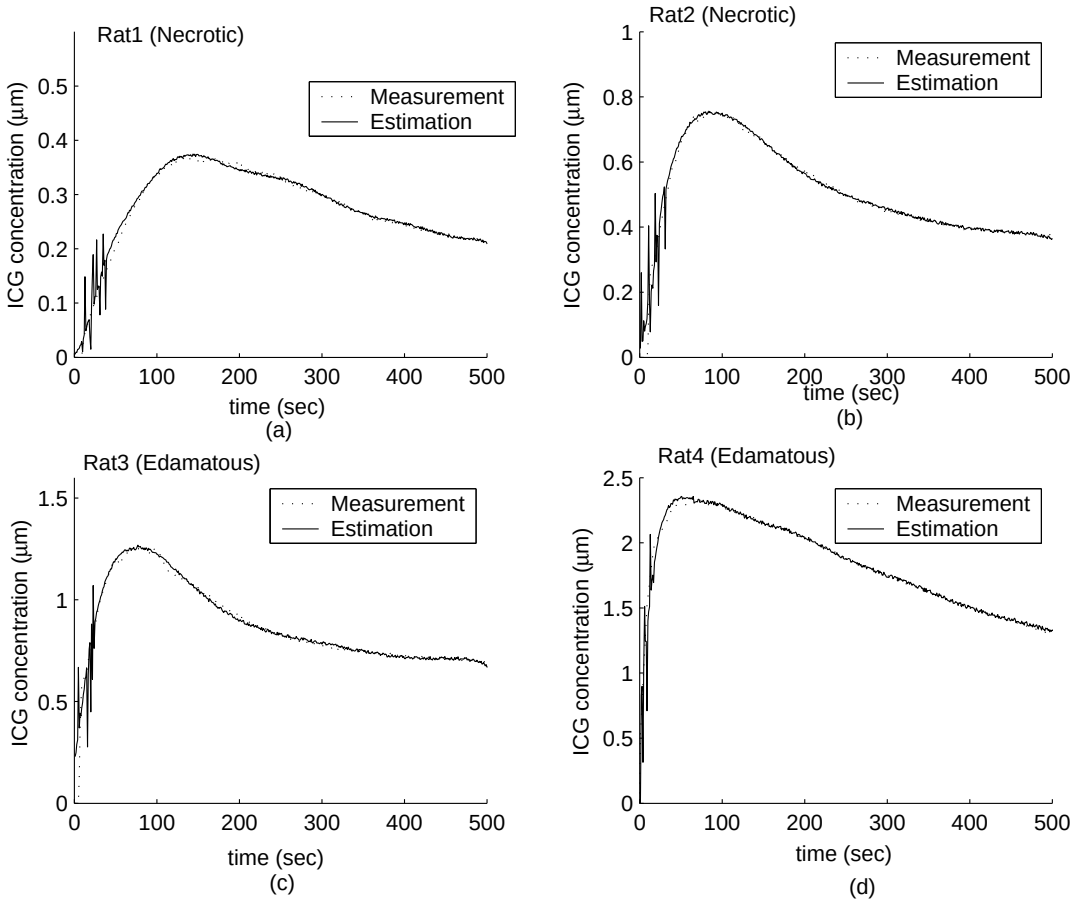

Figure 2.5: ICG concentration measurement data and 1-step prediction of the measurements for four different rats.

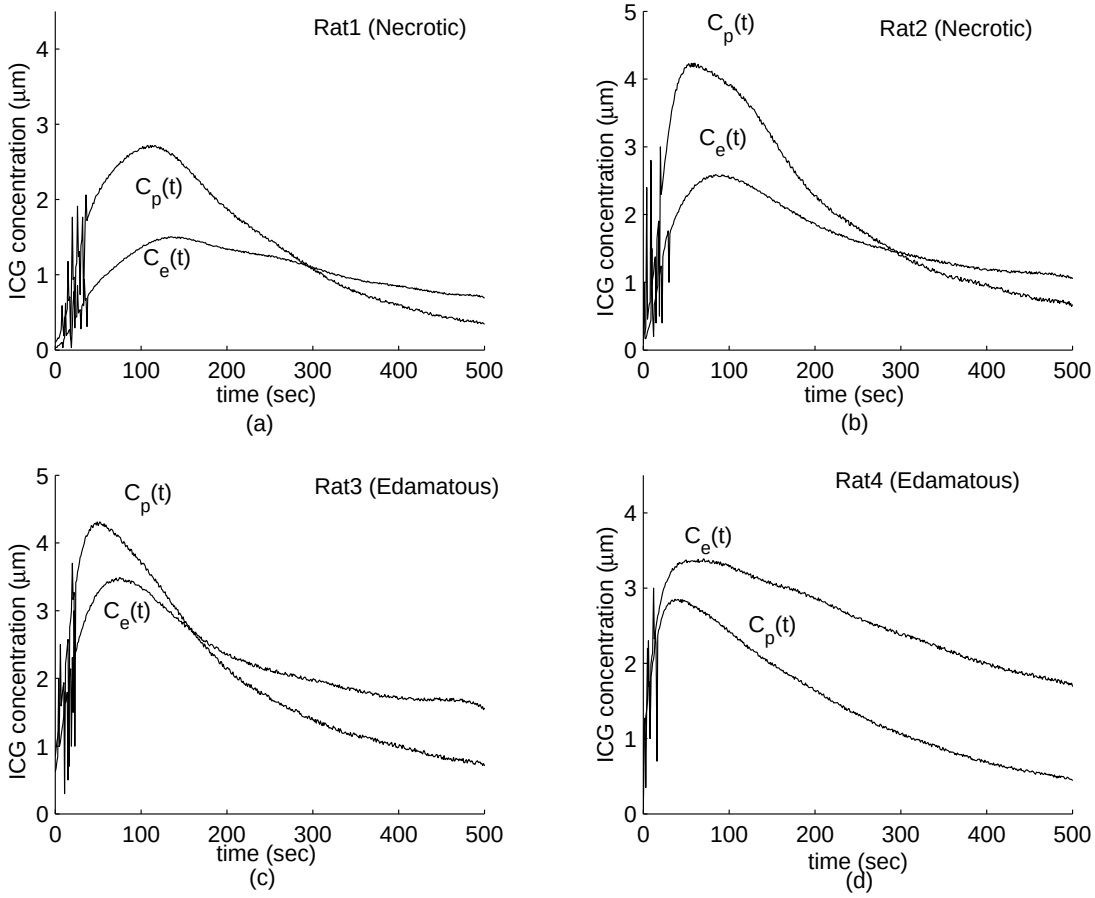

Figure 2.6: ICG concentrations in plasma, $C_p(t)$ and EES, $C_e(t)$, for four different rats. (a) Rat1, (b) Rat2, (c) Rat3, and (d) Rat4.

CHAPTER 3
Pharmacokinetic-rate Images of Indocyanine Green for Breast Tumors using Near Infrared Optical Methods

In the studies described in Chapter 1 and Chapter 2 [25,96,97], the pharmacokinetic-rates are assumed to be constant over a tissue volume that may be as large as the entire imaging domain. However, pharmacokinetic-rates are expected to be different in healthy and tumor tissue as reported in positron emission tomography (PET), and magnetic resonance imaging (MRI) literature. It was shown that the spatially resolved pharmacokinetic-rate analysis provides increased sensitivity and specificity for breast cancer diagnosis [29, 32, 33].

In the area of diffuse NIR spectroscopy and imaging, a number of studies on spatially resolved pharmacokinetic-rates has been reported [95, 150]. Gurfinkel et al. [95] presented *in vivo* NIR reflectance images of ICG pharmacokinetics to discriminate canine adenocarcinoma (located at 0.5-1 cm depth) from normal mammary tissue. These images were generated by a non-tomographic technique using a CCD camera that is suitable only to image tumors close to surface. Milstein *et al* [150] presented a Bayesian tomographic image reconstruction method to form pharmacokinetic-rate images of optical fluorophores based on fluorescence diffuse optical tomography. Numerical simulations show that the method provides good contrast. However, no real data experiments were presented to study the diagnostic value of spatially resolved pharmacokinetic-rates.

In this chapter, we present a method of forming pharmacokinetic-rate images and report spatially resolved pharmacokinetic-rates of ICG using *in vivo* NIR data acquired from three patients with breast tumors. To the best of our knowledge, our work is the first study presenting the pharmacokinetic-rate images of an optical contrast agent using *in vivo* breast data based on tomographic techniques. We first develop a set of spatio-temporally resolved ICG concentration images based on differential diffuse optical tomography. We model the ICG pharmacokinetics by a two-compartment model composed of plasma and extracellular-extravascular space

(EES) compartments. We then estimate the ICG pharmacokinetic-rates and the concentrations in different compartments based on the EKF framework [25]. We show that the pharmacokinetic-rates from the tumor region and outside the tumor region are statistically different. We also estimate a single set of pharmacokinetic-rates (bulk pharmacokinetic-rates) for the entire breast tissue. Our study indicates that spatially resolved pharmacokinetic-rates provide more consistent and superior diagnostic information as compared to the bulk pharmacokinetic-rates.

The rest of the chapter is organized as follows: In Section 3.1, we present the reconstruction of ICG concentration images. In Section 3.2, we present modeling and estimation of ICG pharmacokinetic-rate images using the EKF framework. In Section 3.3, we present the spatially resolved ICG pharmacokinetic-rate analysis of *in vivo* breast data. Section 3.4 summarizes our results.

3.1 Reconstruction of Bulk ICG Concentration Images

In our data collection process, a sequence of boundary measurements are collected over a period of time. Each set of measurements are used to form a frame of the ICG concentration images. The resulting sequence of ICG concentration images are then used to form pharmacokinetic-rate images. To reconstruct each frame of the ICG concentration images, we follow a static reconstruction approach and use differential diffuse optical tomography (DDOT) technique [97, 189].

In DDOT, two sets of excitation measurements are collected corresponding to before and after the ICG injection, and the ICG concentration is determined by the perturbation method [97, 189]. The photon propagation before and after the injection is modeled by the following diffusion equations:

$$\nabla \cdot D_x(r)\nabla\Phi_x^{\pm}(r,\omega) - \left(\mu_{ax}^{\pm}(r) + j\omega/c\right)\Phi_x^{\pm}(r,\omega) = 0, \qquad r \in \Omega \subset R^3 \tag{3.1}$$

with Robin-type boundary conditions:

$$2D_x(r)\frac{\partial\Phi_x^{\pm}(r,\omega)}{\partial\nu} + \rho\Phi_x^{\pm}(r,\omega) = -S(r,\omega), \qquad r \in \partial\Omega. \tag{3.2}$$

where x stands for the excitation, c is the speed of light inside the medium Ω; ω

denotes the modulation frequency of the source, $\mu_{ax}^{-}(r)$ and $\mu_{ax}^{+}(r)$ are the absorption coefficients before and after the ICG injection, D_x is the diffusion coefficient which is assumed independent of $\mu_{ax}^{\pm}$, known but not necessarily constant, $\Phi_x^{\pm}(r,\omega)$ denotes optical field at location r before and after the ICG injection. Here, ν denotes the outward normal to the boundary $\partial\Omega$ of Ω, ρ is a constant representing the refractive index mismatch between the two regions separated by $\partial\Omega$, and $S(r,\omega)$ is the excitation source on the boundary.

The absorption coefficient after the injection μ_{ax}^{+} are modeled as a sum of the absorption coefficient of the medium before the ICG injection μ_{ax}^{-} and the perturbation caused by the ICG $\Delta\mu_{ax}(r)$:

$$\Delta\mu_{ax}(r) = \mu_{ax}^{+}(r) - \mu_{ax}^{-}(r), \quad r \in \Omega \subseteq R^3. \tag{3.3}$$

In the forward model, the analytical solutions of the heterogonous diffusion equation given in (3.1) is derived using first order Rytov approximation [97]. The sample volume is divided into a set of voxels and the measurements are related to the relative absorption coefficients of each voxel by a system of linear equations. The shape of the breast was approximated as a cylinder and the Kirchhoff approximation [139,140] for diffuse waves was used to model the interaction of light with boundaries. In order to minimize optode-tissue coupling mismatch due to breathing motion, the forward model was augmented with the coupling coefficient technique as described in Boas *et al* [141].

Here, the Rytov-type measurements, which are defined by the natural logarithm of the ratio of the post-ICG measurements to the pre-ICG measurements were used [189]. Let $\Psi_x(r_d,\omega;r_s)$ denote the Rytov-type measurements at location r_d due to source at r_s. The linearized relationship between the differential absorption coefficient and measurements is given by [166],

$$\Psi_x(r_d,\omega;r_s) = -\frac{1}{\Phi_x^{-}(r_d,\omega;r_s)} \int_\Omega G_x^{-}(r-r_d,\omega;r_s) I_x(r) \Phi_x^{-}(r,\omega;r_s) d^3r \tag{3.4}$$

where $\Phi_x^{-}(r,\omega;r_s)$ is the photon density obtained at the excitation wavelength before ICG injection, $I_x(r) = c\Delta\mu_{ax}(r)/D_x$, and $G_x^{-}(r-r_d,\omega;r_s)$ is the Green's function of

(3.1) for a source at r_s before the injection describing the propagation of light from the heterogeneity r to the detector at r_d.

We address the inverse problem of recovering $\Delta\mu_{ax}$ from Rytov-measurements Ψ_x based on the forward model (3.4) using the singular value decomposition of the Moore-Penrose generalized system. We use a zeroth-order Tikhonov regularization to stabilize the inversion procedure. The regularization parameter was determined by L-curve analysis [142] using the data obtained from a phantom study previously employed to validate the apparatus [97]. The optimal regularization parameter was found to be 6×10^{-4} and set to be the same for all patient images and time instances. A detailed discussion of the forward and inverse models used for the reconstruction of differential absorption coefficients ($\Delta\mu_{ax}$) can be found in Intes *et al* [97].

To construct a set of ICG concentration images, we use the linear relationship between the differential absorption coefficients and ICG concentrations [46]:

$$\Delta\mu_a(r) = ln10\ \epsilon_\lambda\ m(r) \tag{3.5}$$

where ϵ_λ is the extinction coefficient of ICG at the wavelength 805nm, $m(r)$ is the bulk ICG concentration in the tissue, and $\Delta\mu_a(r)$ is as defined in (3.3).

Note that the method described here is applicable for frequency domain case but for simplicity we set the frequency to zero, i.e. $\omega = 0$.

3.2 Modeling and Estimation of ICG Pharmacokinetics

3.2.1 Two-compartment Model of ICG Pharmacokinetics

Using the method outlined in Section 3.2, we reconstruct a sequence of ICG concentration images. As an example, Fig. 3.1-3.3 shows a set of images reconstructed from *in vivo* breast data.

Our objective is to model the pharmacokinetics of ICG at each voxel of ICG concentration images using compartmental modeling. To do so, we first extracted the time varying ICG concentration curves for each voxel from the sequence of ICG concentration images. An example of such a curve is shown in Fig. 3.4. We next fit a two-compartment model to each ICG concentration curve [25, 95].

Using the two-compartment model introduced by Alacam *et al* [25], ICG transition between plasma and extracellular-extravascular space (EES) can be modeled as follows:

$$\begin{bmatrix} \dot{C}_e(t) \\ \dot{C}_p(t) \end{bmatrix} = \begin{bmatrix} -k_{out} & k_{in} \\ k_{out} & -(k_{in}+k_{elm}) \end{bmatrix} \begin{bmatrix} C_e(t) \\ C_p(t) \end{bmatrix} + \boldsymbol{\omega}(t),\ t \in\ [T_0, T_1] \tag{3.6}$$

where $C_p(t)$ and $C_e(t)$ represent the ICG concentrations in plasma and EES at time t, respectively. The rates k_{in}, k_{out}, and k_{elm} have a unit of sec^{-1}. They are defined as the permeability surface area products given by $PS\gamma$, where P is the capillary permeability constant, S is the capillary surface area, and γ is the tissue density. k_{in} and k_{out} govern the leakage into and the drainage out of the EES. The parameter k_{elm} describes the ICG elimination from the body through kidneys and liver. Here, $\boldsymbol{\omega}(t)$ is uncorrelated zero-mean Gaussian process with covariance matrix $\mathbf{Q}$ representing the model mismatch.

The actual total ICG concentration in the tissue is a linear combination of plasma and the EES ICG concentrations, and modeled as:

$$m(t) = \begin{bmatrix} v_e & v_p \end{bmatrix} \begin{bmatrix} C_e(t) \\ C_p(t) \end{bmatrix} + \eta(t),\quad t \in\ [T_0, T_1] \tag{3.7}$$

where $m(t)$, $C_e(t)$, and $C_p(t)$ are defined in (3.5) and (3.6); v_p and v_e are plasma and the EES volume fractions, respectively; and $\eta(t)$ is uncorrelated zero-mean Gaussian process with covariance matrix $\mathbf{R}$, representing the measurement noise.

3.2.2 Estimation of ICG Pharmacokinetics using Extended Kalman Filtering

In matrix-vector notation, (3.6) and (3.7) can be expressed as:

$$\dot{\mathbf{C}}(t) = \mathbf{K}(\boldsymbol{\alpha})\mathbf{C}(t) + \boldsymbol{\omega}(t), \tag{3.8}$$

$$m(t) = \mathbf{V}(\boldsymbol{\alpha})\mathbf{C}(t) + \eta(t),$$

where $\mathbf{C}(t)$ denotes the concentration vector with elements $C_e(t)$, and $C_p(t)$; $\mathbf{K}(\boldsymbol{\alpha})$ is the system matrix, $\mathbf{V}(\boldsymbol{\alpha})$ is the measurement matrix as defined in equation (3.7), and $\boldsymbol{\alpha}$ is the parameter vector given by

$$\boldsymbol{\alpha} = [k_{out} \;\; k_{in} \;\; k_{elm} \;\; v_e \;\; v_p]^T. \tag{3.9}$$

The ICG measurements in (3.8) are collected at discrete time instances, $t = kT$, $k = 0, 1, ...$, where T is the sampling period. Therefore, the continuous model described in (3.8) is discretized. We can express the discrete compartmental model as follows:

$$\mathbf{C}_d(k+1) = \mathbf{K}_d(\boldsymbol{\theta})\mathbf{C}_d(k) + \boldsymbol{\omega}_d(k), \tag{3.10}$$

$$\mathbf{m}(k) = \mathbf{V}_d(\boldsymbol{\theta})\mathbf{C}_d(k) + \boldsymbol{\eta}_d(k),$$

where $\mathbf{K}_d(\boldsymbol{\theta}) = e^{\mathbf{K}(\boldsymbol{\alpha})}$ is the discrete time system matrix; $\mathbf{V}_d(\theta) = \mathbf{V}(\boldsymbol{\alpha})$ is the discrete measurement matrix; $\boldsymbol{\omega}_d(k)$ and $\boldsymbol{\eta}_d(k)$ are zero-mean Gaussian white noise processes with covariances matrix $\mathbf{Q}_d$ and variance $\mathbf{R}_d$, respectively. The vector $\boldsymbol{\theta}$ is composed of parameters τ_{ij} which are functions the pharmacokinetic-rates and volume fractions:

$$\boldsymbol{\theta} = \begin{bmatrix} \tau_{11} & \tau_{12} & \tau_{21} & \tau_{22} & v_e & v_p \end{bmatrix}^T. \tag{3.11}$$

We first estimate τ_{ij}'s, $i, j = 1, 2$ and then compute the pharmacokinetic-rates k_{in}, k_{out} and k_{elm} [25, 111]. The explicit form of the discrete state-space model is given as follows:

$$\begin{bmatrix} C_e(k+1) \\ C_p(k+1) \end{bmatrix} = \begin{bmatrix} \tau_{11} & \tau_{12} \\ \tau_{21} & \tau_{22} \end{bmatrix} \begin{bmatrix} C_e(k) \\ C_p(k) \end{bmatrix} + \boldsymbol{\omega}_d(k) \tag{3.12}$$

$$m(k) = \begin{bmatrix} v_e & v_p \end{bmatrix} \begin{bmatrix} C_e(k) \\ C_p(k) \end{bmatrix} + \eta_d(k).$$

We estimate the parameter vector $\boldsymbol{\theta}$ and concentration vector $\mathbf{C}_d$ by using the EKF framework. The EKF is a recursive modeling and estimation method with numerous advantages in ICG pharmacokinetic modeling [25]. These include effective modeling of multiple compartments, and multiple measurement systems in the presence of measurement noise and uncertainties in the compartmental model

dynamics, simultaneous estimation of model parameters and ICG concentrations in each compartment, statistical validation of estimated concentrations and error bounds on the model parameter estimates, and incorporation of available a priori information about the initial conditions of the permeability rates into the estimation procedure.

When both states (ICG concentrations) and model parameters (pharmacokinetic-rates and volume fractions) are unknown, a linear state-space model can be regarded as a non-linear model; the linear system parameters and states combine to form the new states of the non-linear model. This system is then linearized and the new unknown states are found using the EKF estimator [25, 115–117]. In EKF framework, $\boldsymbol{\theta}$ can be treated as a random process with the following model:

$$\boldsymbol{\theta}(k+1) = \boldsymbol{\theta}(k) + \boldsymbol{\varsigma}_d(k), \tag{3.13}$$

where $\boldsymbol{\varsigma}_d(k)$ is a zero-mean Gaussian process with covariance matrix $\mathbf{S}_d$.

Table 3.1 summarizes the joint estimation of pharmacokinetic-rates and ICG concentration in different compartments. In Table 3.1, $\hat{\mathbf{C}}_d(k|k-1)$ is the state estimate propagation at step k given all the measurements up to step $k-1$; $\hat{\mathbf{C}}_d(k)$ is the state estimate update at step k; $\mathbf{P}_{k,k-1}$ denotes the error covariance propagation at step k given all the measurements up to step $k-1$; $\mathbf{P}_{k,k}$ is the error covariance update at step k; $\mathbf{S}_d$ is the preassigned covariance matrix of $\boldsymbol{\varsigma}_d(k)$; $\mathbf{J}_k$ is the Jacobian matrix due to iterative linearization of the state equation at step k; $\mathbf{G}_k$ is the recursive Kalman gain at step k; $\mathbf{R}_d$ is the covariance matrix of the measurements; $\mathbf{Q}_d$ is the covariance matrix of the concentration vector; and $\mathbf{I}$ is the identity matrix. A detailed discussion of the extended Kalman filtering algorithm, and the initialization of the parameters, concentrations, and covariance matrices can be found in Alacam *et al* [25].

Table 3.1: EKF algorithm for simultaneous estimation of states and parameters.

Initial Conditions	$\begin{bmatrix}\hat{\mathbf{C}}_d(0)\\ \hat{\boldsymbol{\theta}}(0)\end{bmatrix} = \begin{bmatrix}E(\mathbf{C}_d(0))\\ \hat{\boldsymbol{\theta}}(0)\end{bmatrix}, \quad \mathbf{P}_{0,0} = \begin{bmatrix}Var(\mathbf{C}_d(0)) & 0\\ 0 & \mathbf{S}_d\end{bmatrix}$
State Estimate Propagation	$\begin{bmatrix}\hat{\mathbf{C}}_d(k\|k-1)\\ \hat{\boldsymbol{\theta}}(k\|k-1)\end{bmatrix} = \begin{bmatrix}\mathbf{K}_d(\hat{\boldsymbol{\theta}}(k-1))\hat{\mathbf{C}}_d(k-1)\\ \hat{\boldsymbol{\theta}}(k-1)\end{bmatrix}$
Error Covariance Propagation	$\mathbf{P}_{k,k-1} = \mathbf{J}_{k-1}\mathbf{P}_{k-1,k-1}\mathbf{J}_{k-1}^T + \begin{bmatrix}\mathbf{Q}_d & 0\\ 0 & \mathbf{S}_d\end{bmatrix}$
State Estimate Update	$\begin{bmatrix}\hat{\mathbf{C}}_d(k)\\ \hat{\boldsymbol{\theta}}(k)\end{bmatrix} = \begin{bmatrix}\hat{\mathbf{C}}_d(k\|k-1)\\ \hat{\boldsymbol{\theta}}(k\|k-1)\end{bmatrix} + \mathbf{G}_k(\mathbf{m}(k) - \mathbf{V}_d(\hat{\boldsymbol{\theta}}(k\|k-1))\hat{\mathbf{C}}_d(k\|k-1))$
Error Covariance Update	$\mathbf{P}_{k,k} = [\mathbf{I} - \mathbf{G}_k\boldsymbol{\Lambda}_{k\|k-1}]\mathbf{P}_{k,k-1}$
Kalman Gain	$\mathbf{G}_k = \mathbf{P}_{k,k-1}\boldsymbol{\Lambda}_{k\|k-1}^T[\boldsymbol{\Lambda}_{k\|k-1}\mathbf{P}_{k,k-1}\boldsymbol{\Lambda}_{k\|k-1}^T + \mathbf{R}_d]^{-1}$
Definitions	$\mathbf{J}_k = \begin{bmatrix}\mathbf{K}_d(\hat{\boldsymbol{\theta}}(k)) & \frac{\partial}{\partial\boldsymbol{\theta}}[\mathbf{K}_d(\hat{\boldsymbol{\theta}}(k))\hat{\mathbf{C}}_d(k)]\\ \mathbf{0} & \mathbf{I}\end{bmatrix}$ $\boldsymbol{\Lambda}_{k\|k-1} = \begin{bmatrix}\mathbf{V}_d(\hat{\boldsymbol{\theta}}(k\|k-1))\\ 0\end{bmatrix}^T$

3.3 Spatially Resolved ICG Pharmacokinetic-rate Analysis of *in vivo* Breast Data

3.3.1 Apparatus

In this work, we use the data collected with a continuous wave (CW) NIR imaging apparatus. The apparatus has 16 light sources, which are tungsten bulbs with less than 1 watt of output power. They are located on a circular holder at an equal distance from each other with 22.5 degrees apart. Sixteen detectors, namely, silicon photodiodes, are situated in the same plane. The breast is arranged in a pendular geometry with the source-detector probes gently touching its surface. Figure 3.5 illustrates the configuration of the apparatus and the configuration of the detectors and the sources in a circular plane. Note that sources and detectors

Table 3.2: Tumor information for each patient

	Tumor Type	Tumor Size	Tumor Location
Case 1	Fibroadenoma	1-2 cm	6-7 o'clock
Case 2	Adenocarcinoma	2-3 cm	4-5 o'clock
Case 3	Invasive Ductal Carcinoma	4 by 3 cm	6 o'clock

are co-located. The detectors use the same positions as the sources to collect the light originating from one source at a time. Only the signals from the farthest 11 detectors are used in the analysis. For example, when Source 1 is on, the data is collected using Detectors 4 to 14. This provides sufficient number of source-detector readings (176 readings) to reconstruct $\Delta\mu_a$ images at each time instant. A band pass filter at 805 nm, the absorption peak of ICG, is placed in front of the sources to select the desired wavelength. A set of data for one source is collected every $\sim$ 500 ms. The total time for a whole scan of the breast including 16 sources and 16 detectors is $\sim$ 8.8 seconds. A more detailed explanation of the apparatus and the data collection procedure can be found in Nioka *et al* [143].

3.3.2 Tumor Information and Protocol

Three different patients with different tumor types are included in this study. Measurements are made before the biopsy to avoid modification of the blood volume and flow in the tumor region. First case, (Case 1), is fibroadenoma, which corresponds to a mass estimated to be $1-2$ cm in diameter within a breast of 9 cm diameter located at 6-7 o'clock. Second case, (Case 2), is adenocarcinoma corresponding to a tumor estimated to be $2-3$ cm in diameter within a breast of 7.7 cm diameter located at 4-5 o'clock. The third case, (Case 3), is invasive ductal carcinoma, which corresponds to a mass estimated to be 4 by 3 cm located at 6 o'clock. Table 3.2 describes the tumor information for each patient. *A priori* information on the location and size of the tumor was obtained by palpation and the diagnostic information was derived *a posteriori* from biopsy and surgery. ICG is injected intravenously by bolus with a concentration of 0.25 mg per kg of body weight. Data acquisition started before the injection of ICG and continued for 10 minutes.

3.4 Results and Discussion

Using the CW imager described above, source-detector readings were collected from different angles for each patient. Differential absorption coefficient images were reconstructed based on DDOT forward model given in equations (3.1) to (3.4) with ω set to zero. Using the linear relationship (3.5) between ICG concentration, and absorption coefficient, ICG concentration images were obtained for each case. A sample set of ICG concentration images for the selected time instants are shown in Figures 3.1-3.3 for Case 1, 2, and 3, respectively. Although only 9 images are displayed, there are approximately 50 images for each case, each corresponding to a different time instant. Each image is composed of 649 voxels. Note that the ICG concentration images in Figures 3.1-3.3 represent the bulk ICG concentrations in the tissue, not the ICG concentrations in plasma or the EES compartments.

We next extracted the time course of ICG concentration for each voxel. As an example, Fig. 3.4 shows the time course of ICG concentrations for all three cases for a specific voxel in the tumor region (65^{th}, 276^{th}, 188^{th} voxel for Case 1, Case 2, and Case 3, respectively). We then fit the two-compartment model to each time course data using the EKF framework; and estimated k_{in}, k_{out}, k_{elm}, and the ICG concentrations in plasma and the EES. We chose initial values within the biological limits that lead to minimum norm error covariance matrix. The images of k_{in}, and k_{out} for each case are shown in Figures 3.6(a)-(b), 3.7(a)-(b), and 3.8(a)-(b), respectively. Additionally, we constructed the ICG concentration images for plasma and the EES compartments. Figures 3.9-3.14 show the ICG concentration in plasma and the EES for 3 different time instants for Case 1, 2, and 3, respectively. Our results show that the pharmacokinetic-rates are higher around the tumor region agreeing with the fact that permeability increases around the tumor region due to compromised capillaries of tumor vessels. We also observed that ICG concentrations in plasma and the EES compartments are higher around the tumors agreeing with the hypothesis that around the tumor region ICG may act as a diffusible extravascular flow in leaky capillary of tumor vessels.

Using the *a priori* and *a posteriori* information on the location, and the size of the tumors, we plotted an ellipse (or a circle) to identify the approximate location

Table 3.3: Mean and standard deviation of pharmacokinetic-rates for the tumor region and outside the tumor region

	k_{in} $(sec^{-1}10^{-2})$		k_{out} $(sec^{-1}10^{-2})$		k_{elm} $(sec^{-1}10^{-3})$	
	Inside	Outside	Inside	Outside	Inside	Outside
Case 1	2.14±0.018	0.73±0.011	1.24±0.069	0.43±0.013	4.11±0.057	3.87±0.012
Case 2	2.92±0.076	1.14±0.052	1.58±0.051	0.65±0.036	3.94±0.081	4.12±0.047
Case 3	6.87±0.093	3.06±0.015	4.96±0.048	1.66±0.072	4.49±0.056	4.46±0.081

and size of the tumor in the pharmacokinetic-rate images. We note that the radii of the ellipses were chosen large enough to include the tumor boundaries. Figures 3.6(a), 3.7(a), and 3.8(a) present the k_{in} images with approximate tumor location and size for Case 1, 2, and 3, respectively. The consistency of the bright regions in the k_{in} images, and circular/elliptical regions drawn based on the *a priori* and *a posteriori* information shows that the pharmacokinetic-rate images may provide good localization of tumors.

The histograms of k_{in} and k_{out} images for the tumor region (as indicated by circular/elliptical regions) and outside the tumor region are shown in Figures 3.15(a)-(c) and Figures 3.16(a)-(c), respectively. Note that all non-zero voxels outside the elliptical region constitute "outside the tumor region". The solid curves in Figures 3.15 and 3.16 show the Gaussian fit. The histograms and their Gaussian fits in Figures 3.15 and 3.16 show that the mean and the standard deviation of k_{in} and k_{out} values are different for the tumor and outside the tumor region. Table 3.3 tabulates the mean values (± spatial standard deviation) of the pharmacokinetic-rates for the tumor region and outside the tumor region for all three cases. The pharmacokinetic rates are higher for Case 3 (invasive ductal carcinoma), for both the tumor region and outside the tumor region as compared to Case 2 (adenocarcinoma). Similarly, the kinetic rates are higher for Case 2 (adenocarcinoma), as compared to Case 1 (fibroadenoma) for both the tumor region and outside the tumor region. This observation shows that high mean values of k_{in} and k_{out} may be indicative of tumor aggressiveness.

To understand the value of pharmacokinetic-rate imaging as compared to the bulk pharmacokinetic-rate analysis, we averaged the concentration images spatially,

Table 3.4: Bulk Pharmacokinetic-rates extracted from the entire breast tissue

	k_{in} $(sec^{-1}10^{-2})$	k_{out} $(sec^{-1}10^{-2})$	k_{elm} $(sec^{-1}10^{-1})$
Case 1	0.84±0.013	0.62±0.017	3.66±0.042
Case 2	2.01±0.022	0.83±0.012	4.01±0.054
Case 3	4.06±0.072	3.36±0.051	4.37±0.052

and obtained a bulk concentration value for each time instant. We then formed a time curve for the bulk ICG concentrations. Next, we fit the two-compartment model to the resulting time curves and estimated the bulk pharmacokinetic-rates. Table 3.4 tabulates the bulk pharmacokinetic-rates for each patient. To compare the bulk rates with spatially resolved rates, in Figures 3.17 and 3.18, the bulk pharmacokinetic-rates are overlaid on the histograms of the pharmacokinetic-rate images. The dotted line shows the Bayesian minimum error classifier threshold, (the value corresponding to the intersection of the histograms), [207], for each case. We see that for Case 1, the bulk rates of k_{in}, and k_{out} are both classified as healthy tissue (outside the tumor region). For Case 2, k_{in} is classified as cancerous tissue (in the tumor region) and k_{out} is classified as healthy tissue. Similarly for Case 3, k_{in} is classified as healthy and k_{out} is classified as cancerous tissue. This indicates that spatially resolved rates may provide more consistent and superior information than the bulk rates.

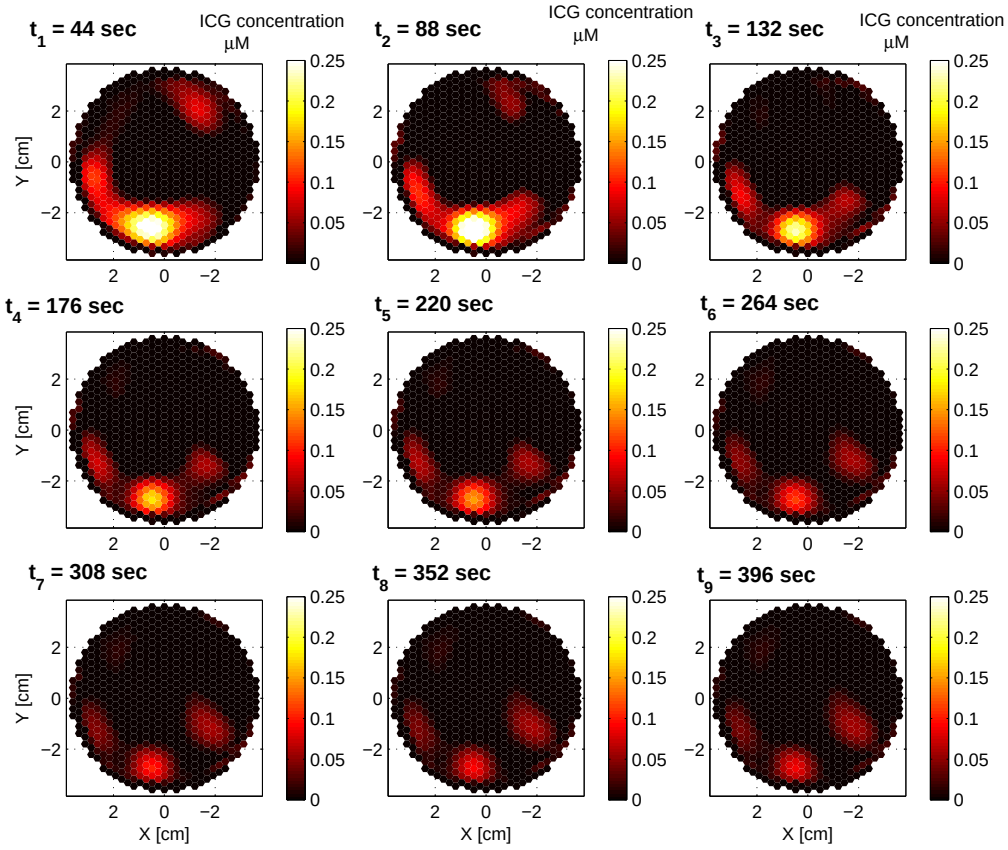

Figure 3.1: ICG concentration images for a set of time instants for Case 1.

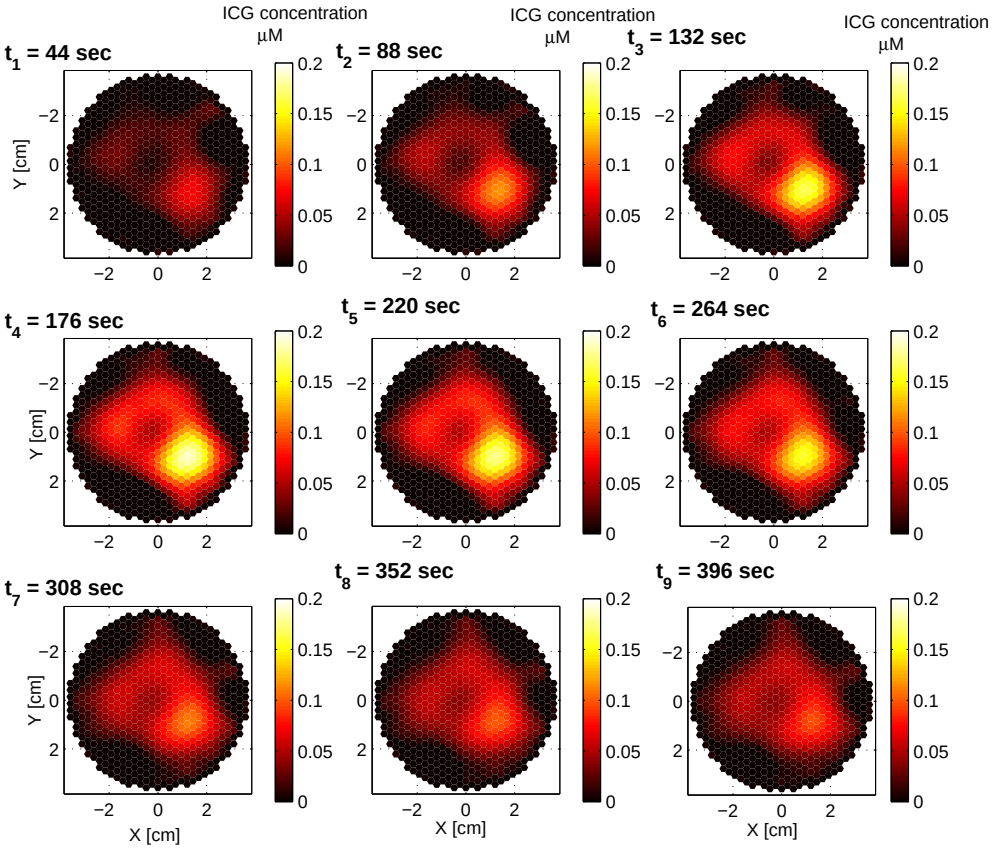

Figure 3.2: ICG concentration images for a set of time instants for Case 2.

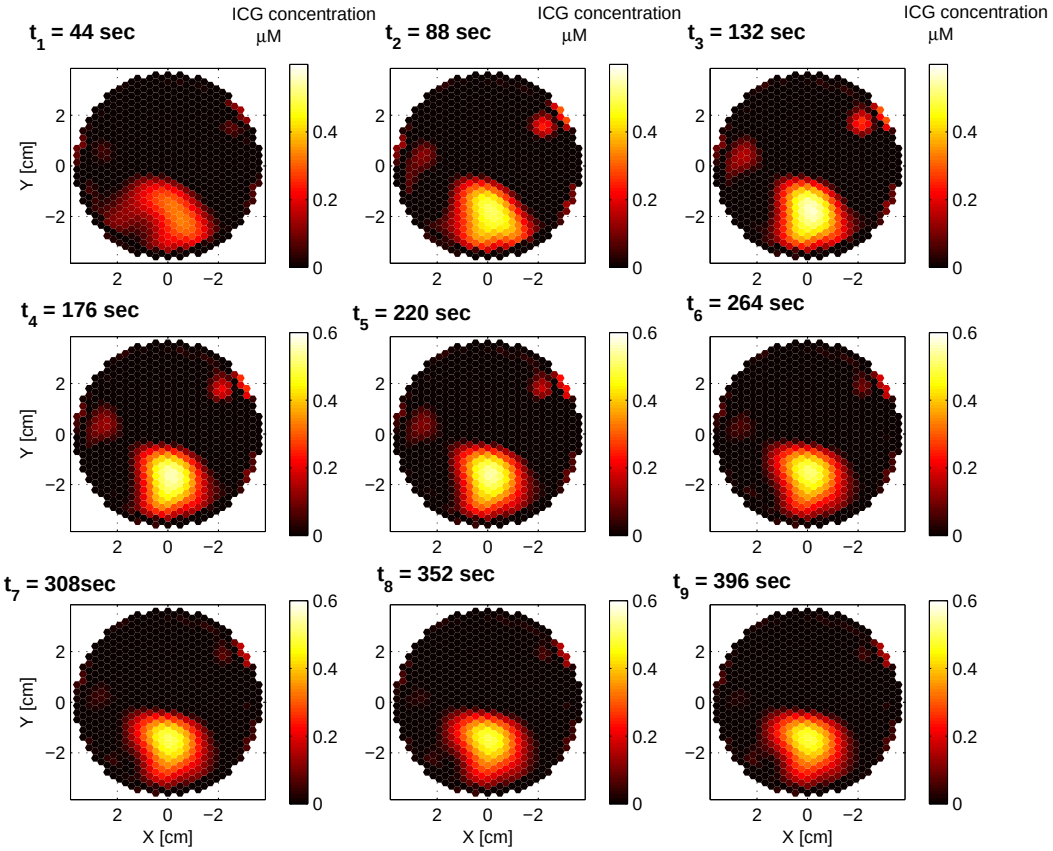

Figure 3.3: ICG concentration images for a set of time instants for Case 3.

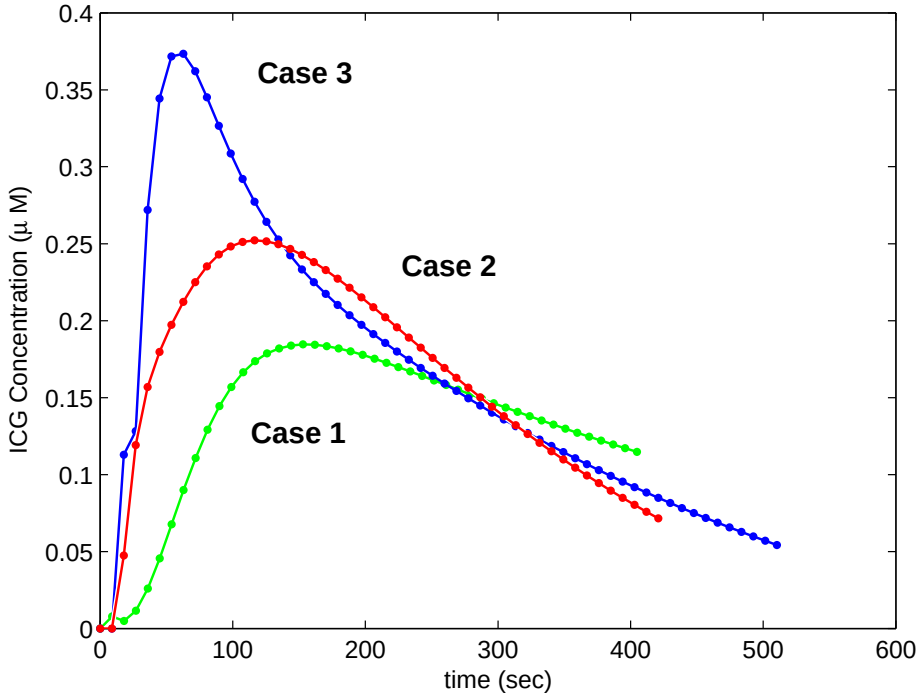

Figure 3.4: Time course of ICG concentration curves for a specific voxel, 65^{th}, 276^{th}, 188^{th} voxel for Case 1, Case 2, and Case 3, respectively.

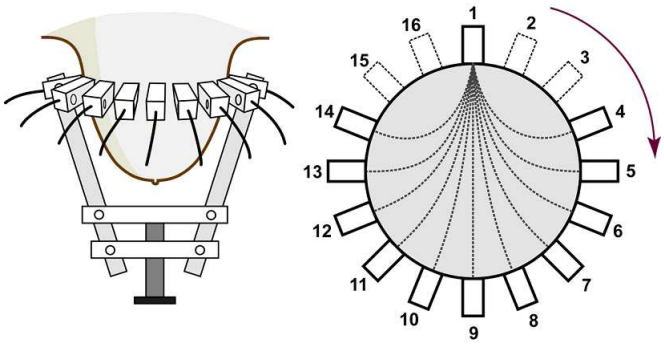

Figure 3.5: (Left) schematic diagram, (Right) the cut section of the CW NIR imaging apparatus with 16 sources and detectors.

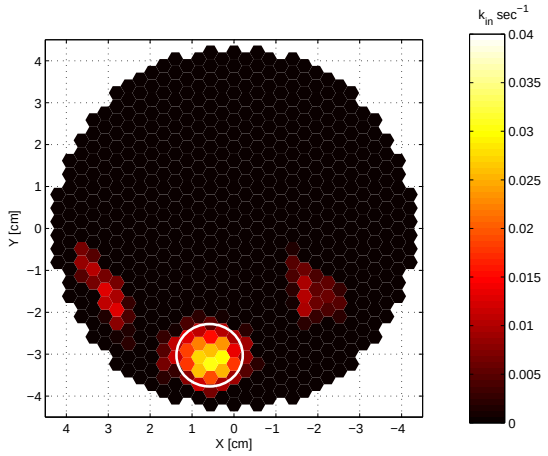

(a)

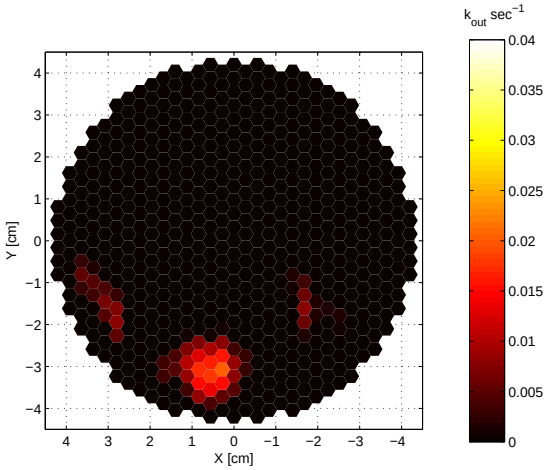

(b)

Figure 3.6: Pharmacokinetic-rate images, (a) k_{in}, and (b) k_{out} for Case 1. The k_{in} images are shown with approximate tumor location and size.

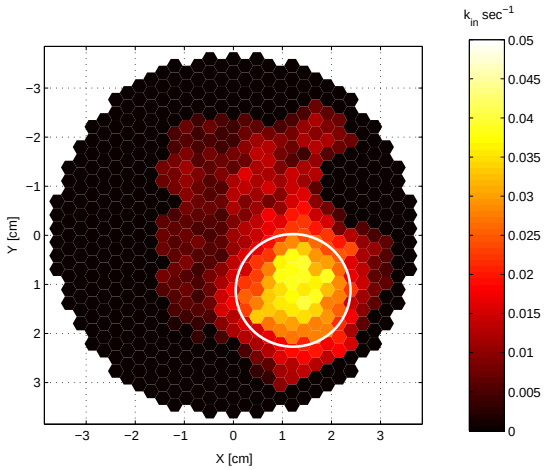

(a)

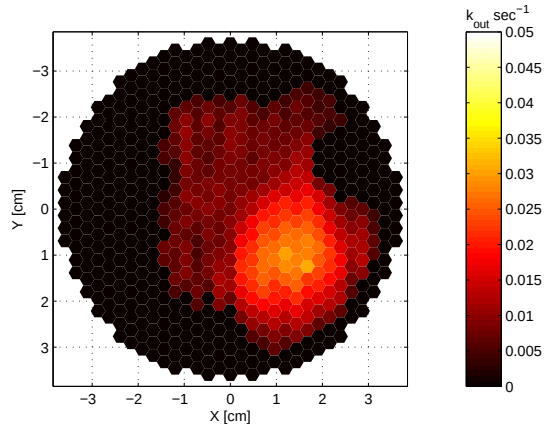

(b)

Figure 3.7: Pharmacokinetic-rate images, (a) k_{in}, and (b) k_{out} for Case 2. The k_{in} images are shown with approximate tumor location and size.

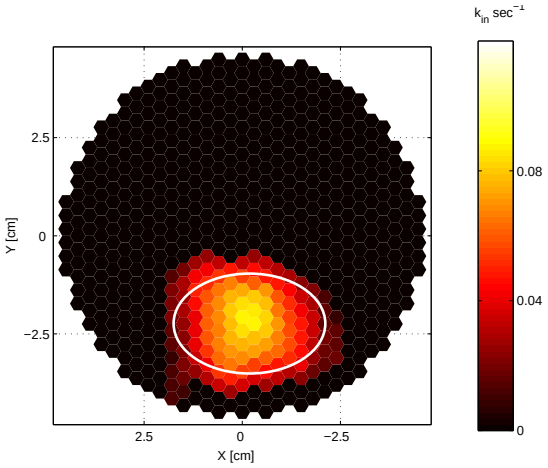

(a)

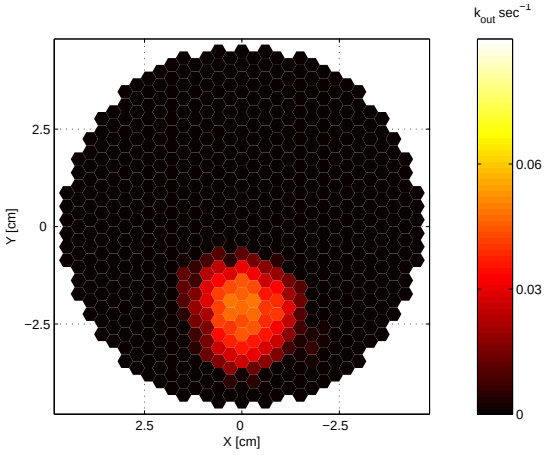

(b)

Figure 3.8: Pharmacokinetic-rate images, (a) k_{in}, and (b) k_{out} for Case 3. The k_{in} images are shown with approximate tumor location and size.

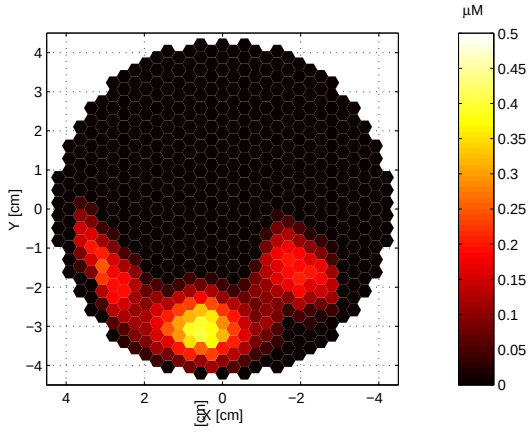

(a)

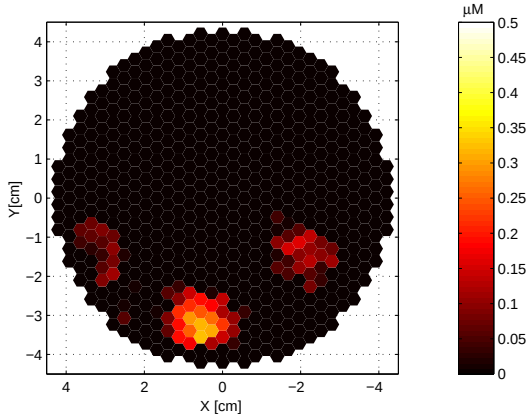

(b)

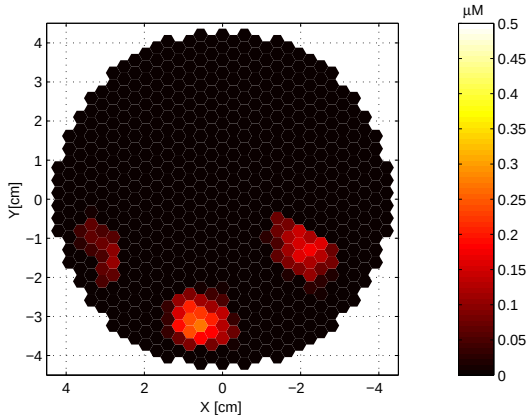

(c)

Figure 3.9: ICG concentration images in plasma for Case 1 for (a) 246.4^{th}, (b) 334.4^{th}, and (c) 422.4^{th} seconds.

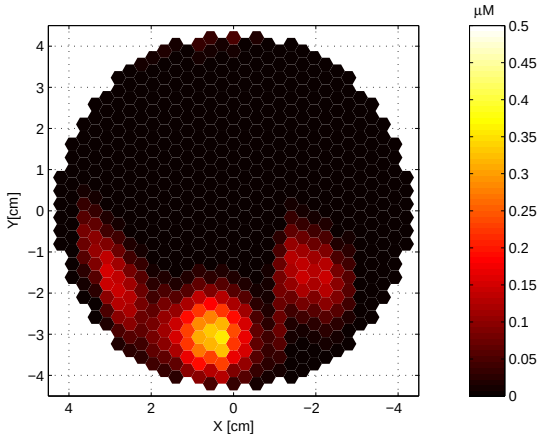

(a)

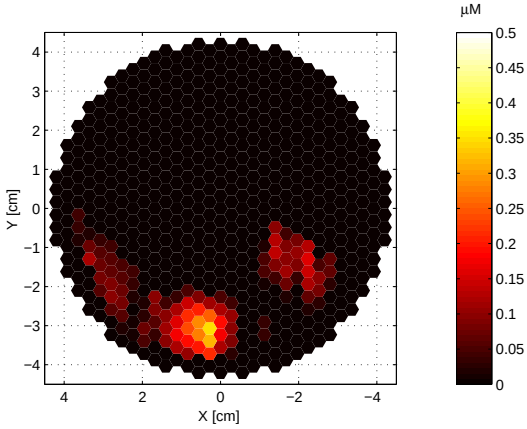

(b)

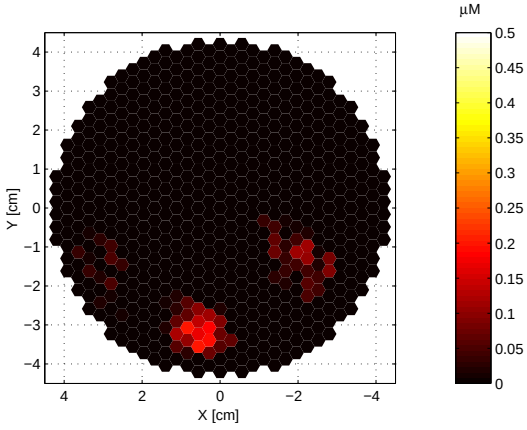

(c)

Figure 3.10: ICG concentration images in the EES for Case 1 for (a) 246.4^{th}, (b) 334.4^{th}, and (c) 422.4^{th} seconds.

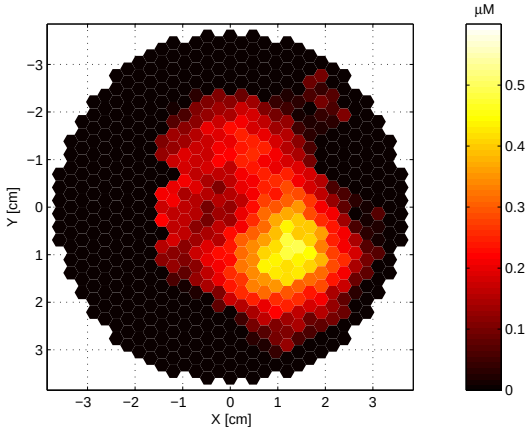

(a)

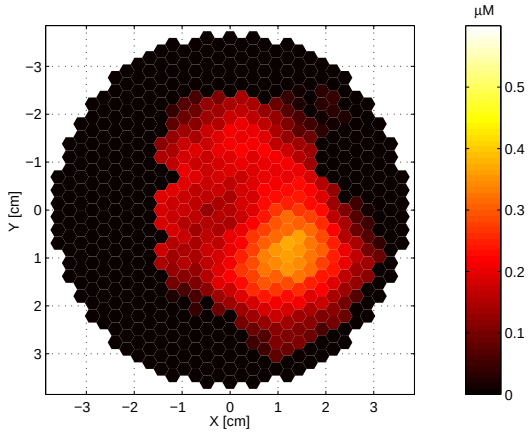

(b)

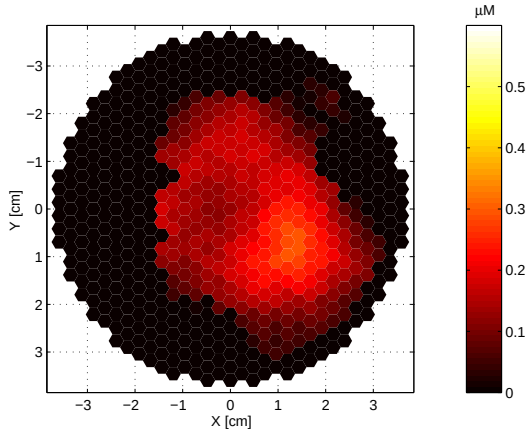

(c)

Figure 3.11: ICG concentration images in plasma for Case 2 for (a) 228.8^{th}, (b) 316.8^{th}, and (c) 404.8^{th} seconds.

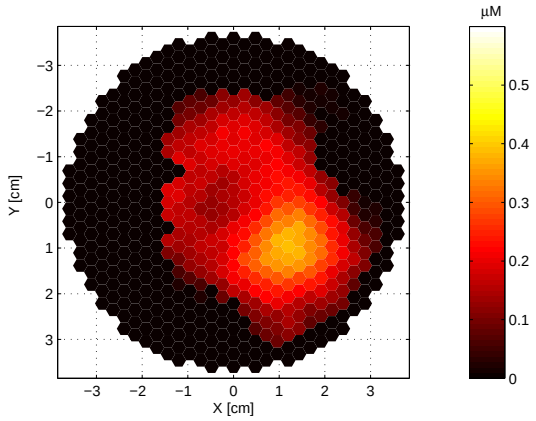

(a)

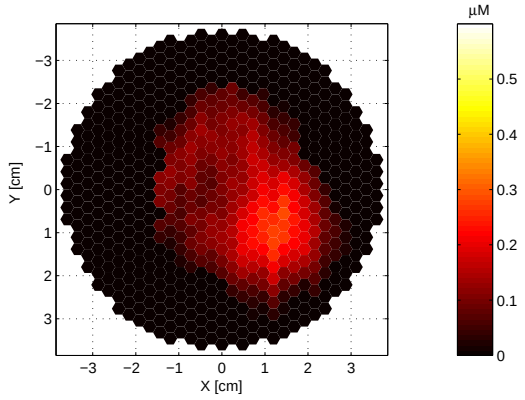

(b)

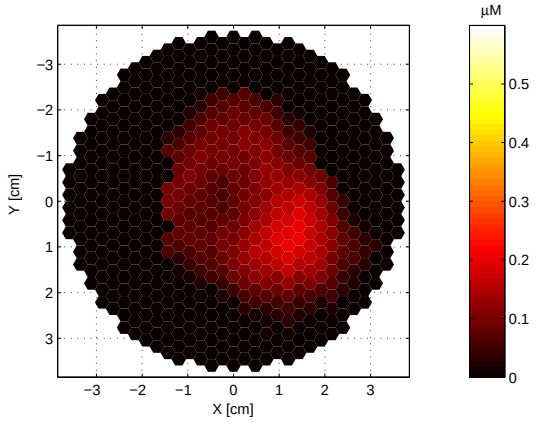

(c)

Figure 3.12: ICG concentration images in the EES for Case 2 for (a) 228.8^{th}, (b) 316.8^{th}, and (c) 404.8^{th} seconds.

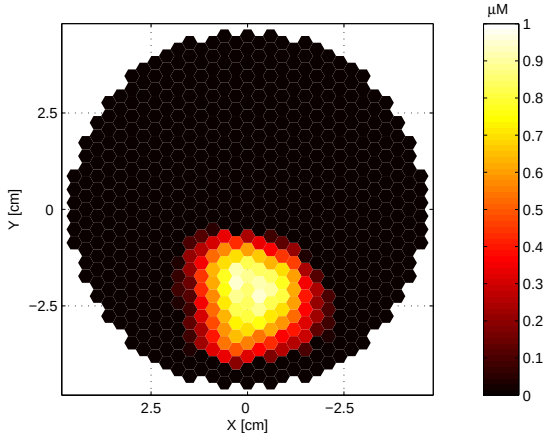

(a)

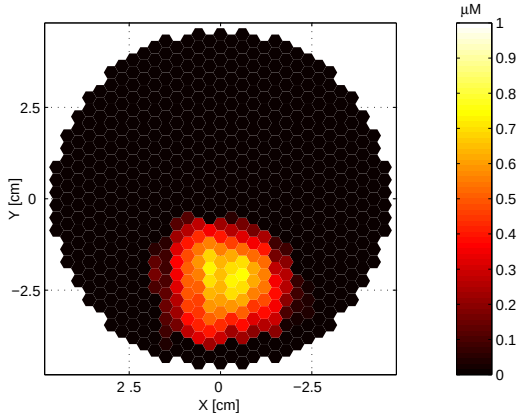

(b)

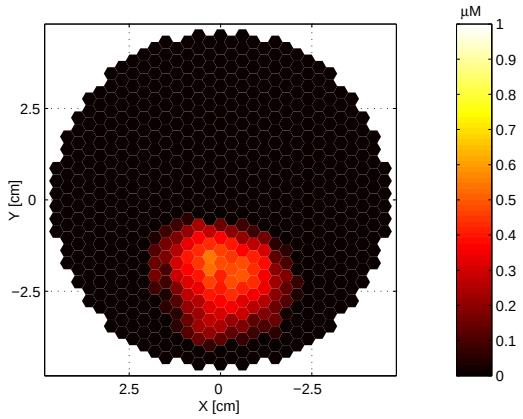

(c)

Figure 3.13: ICG concentration images in the plasma for Case 3 for (a) 246.4^{th}, (b) 378.4^{th}, and (c) 510.4^{th} seconds.

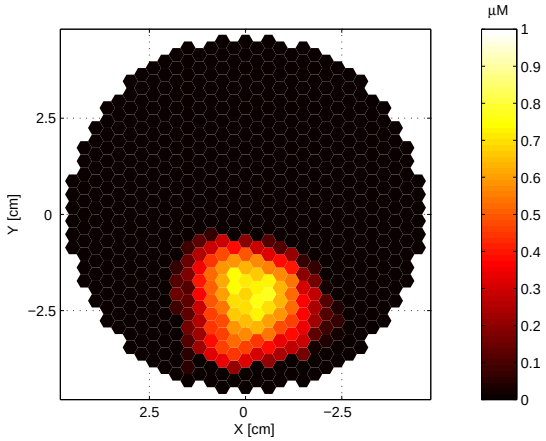

(a)

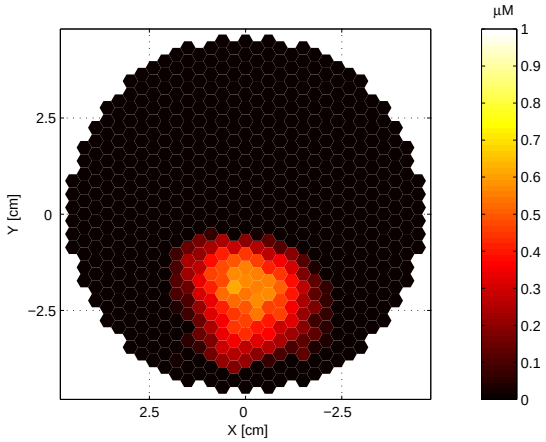

(b)

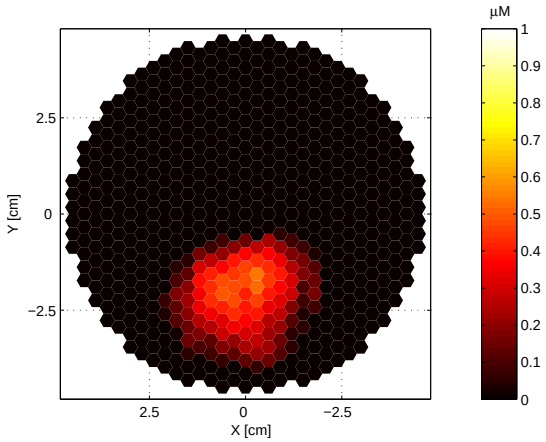

(c)

Figure 3.14: ICG concentration images in the EES for Case 3 for (a) 246.4^{th}**, (b)** 378.4^{th}**, and (c)** 510.4^{th} **seconds.**

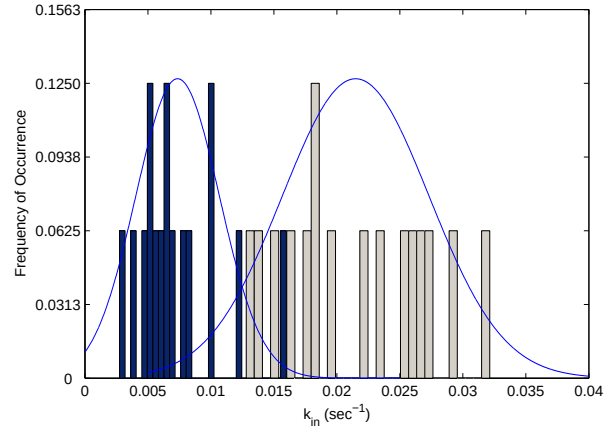

(a)

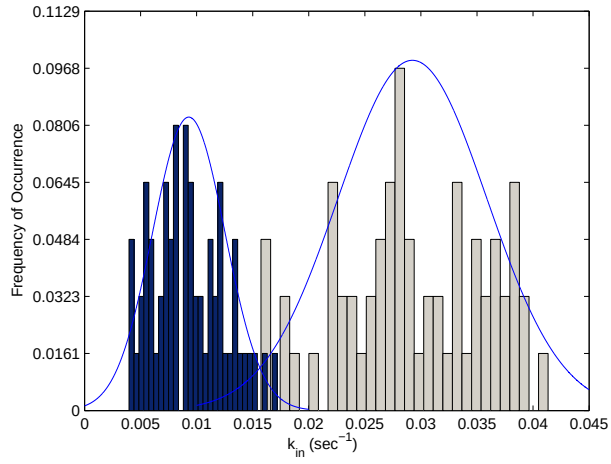

(b)

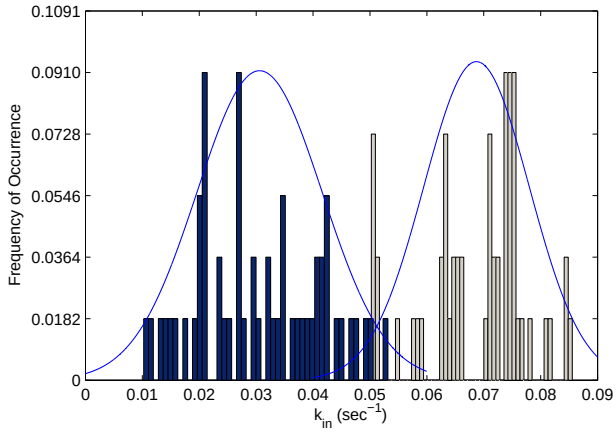

(c)

Figure 3.15: The histograms of k_{in} for (a) Case 1, (b) Case 2, (c), Case 3 for the tumor region (gray) and outside (blue) the tumor region (as indicated by circular/elliptical regions). The solid lines in figures show the Gaussian fit.

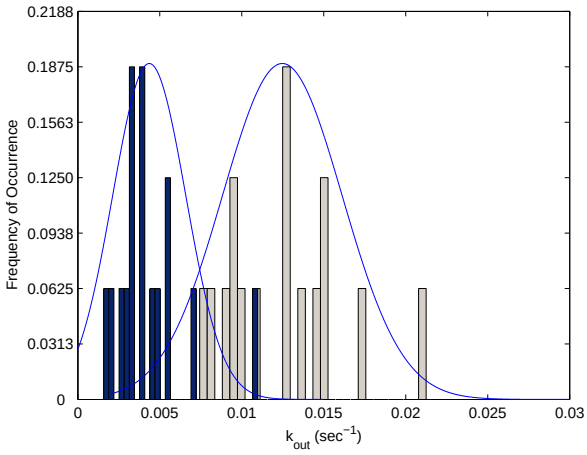

(a)

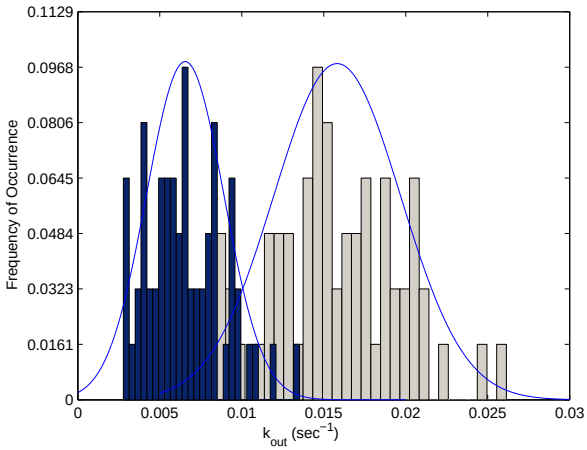

(b)

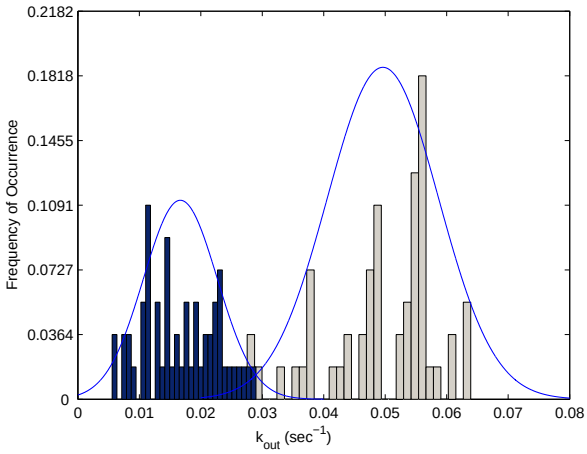

(c)

Figure 3.16: The histograms of k_{out} for (a) Case 1, (b) Case 2, (c), Case 3 for the tumor region (gray) and outside (blue) the tumor region (as indicated by circular/elliptical regions). The solid lines in figures show the Gaussian fit.

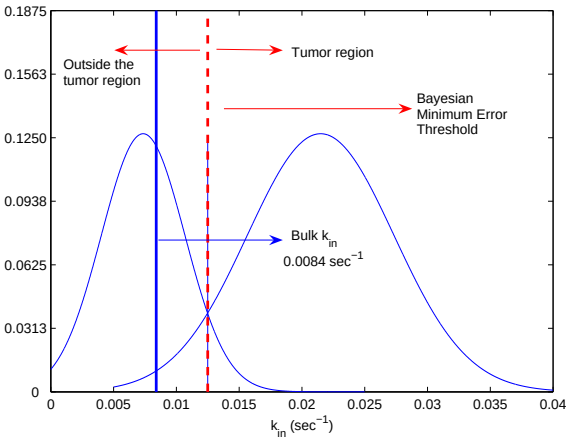

(a)

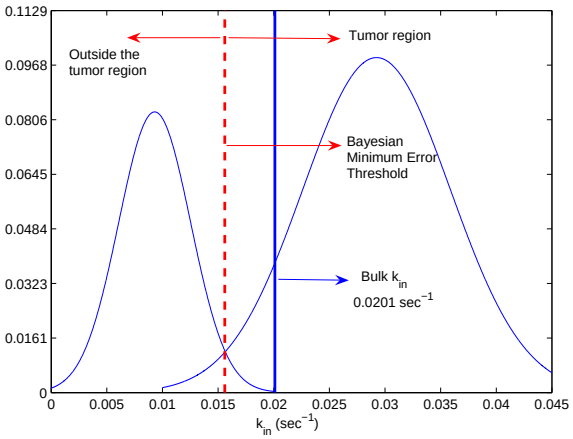

(b)

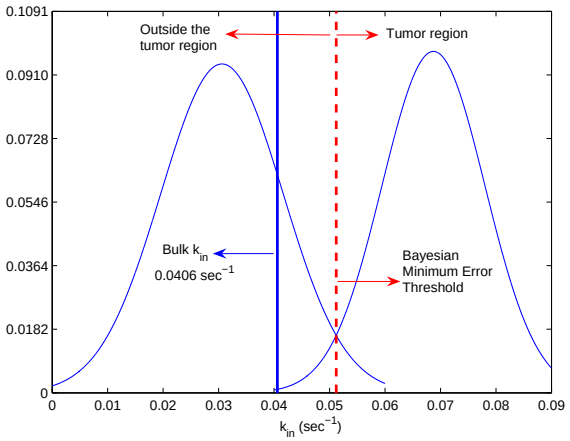

(c)

Figure 3.17: Solid line (blue) shows bulk k_{in} rates for (a) Case 1, (b) Case 2, (c), Case 3 together with the histogram fits. The dashed (red) line indicates the Bayesian minimum error classifier threshold.

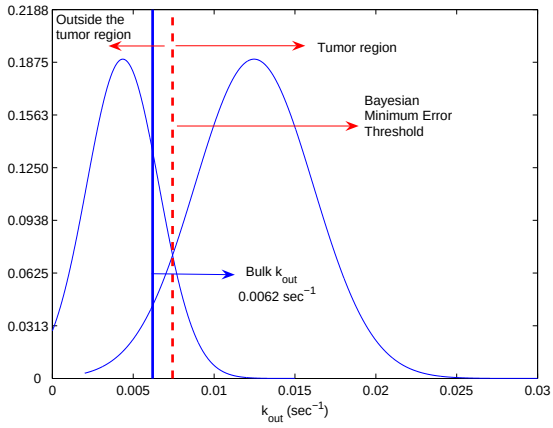

(a)

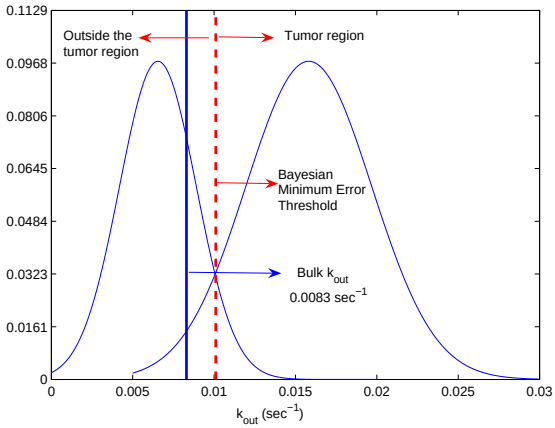

(b)

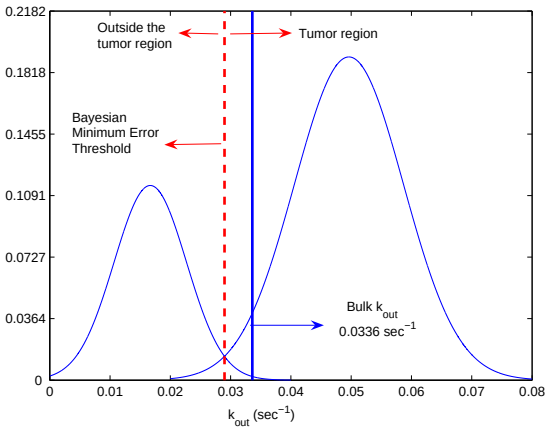

(c)

Figure 3.18: Solid line (blue) shows bulk k_{out} rates for (a) Case 1, (b) Case 2, (c), Case 3 together with the histogram fits. The dashed (red) line indicates the Bayesian minimum error classifier threshold.

CHAPTER 4
Reconstruction of Spatially Resolved Pharmacokinetic Rate Images of Optical Fluorophores from NIR Measurements

In this chapter, we present a new method to form pharmacokinetic-rate images of optical fluorophores directly from near infra-red (NIR) boundary measurements. We first derive a mapping from spatially resolved pharmacokinetic-rates to NIR boundary measurements by combining compartmental modeling with a diffusion based NIR photon propagation model. We express this mapping as a state-space equation. Next, we introduce a spatio-temporal prior model for the pharmacokinetic-rate images and combine it with the state-space equation. We address the image formation problem using the extended Kalman filtering framework. We analyzed the computational complexity of the resulting algorithms and evaluate their performance in numerical simulations and real data obtained from three patients carrying breast tumors.

The rest of the chapter is organized as follows: Section 4.2 describes the spatially resolved compartmental modeling and the two-compartment model for ICG pharmacokinetics. In Section 4.3, we present the NIR photon propagation model based on coupled diffusion equations. In Section 4.4, we present the pharmacokinetic-rate-to-measurement map for optical fluorophores. In Section 4.5, we present the spatio-temporal prior model, the direct reconstruction of pharmacokinetic-rate images based on EKF framework, initialization of the EKF and the computational complexity of the resulting algorithms. In Section 4.6, we present the numerical simulations and the reconstructed images using the *in vivo* breast data.

4.1 Spatially Resolved Compartmental Modeling and the Two-compartment Model for ICG

4.1.1 Spatially Resolved Compartmental Modeling

In general, the continuous-time state-space representation for an n-compartment model is given by

$$d\boldsymbol{\mathcal{C}}(t) = \boldsymbol{\mathcal{K}}(\boldsymbol{\alpha}_n)\boldsymbol{\mathcal{C}}(t)dt, \tag{4.1}$$

$$a(t) = \boldsymbol{\mathcal{V}}(\boldsymbol{\alpha}_n)\boldsymbol{\mathcal{C}}(t) \quad t \in [T_0, T_1] \tag{4.2}$$

where $t \in [T_0, T_1]$ denotes time, $\boldsymbol{\mathcal{C}}(t) \in \mathbb{R}^n$ denotes the concentration vector whose elements are the concentrations of the fluorophores in different compartments, $a(t)$ is the total fluorophore concentration at time t, n is the number of compartments, $\boldsymbol{\alpha}_n$ is the parameter vector whose elements are the pharmacokinetic rates and volume fractions [25]. $\boldsymbol{\mathcal{K}}(\boldsymbol{\alpha}_n) \in \mathbb{R}^{n\times n}$ is the system matrix whose entries are the pharmacokinetic rates and $\boldsymbol{\mathcal{V}}(\boldsymbol{\alpha}_n) \in \mathbb{R}^n$ is the vector comprised of volume fractions.

The compartmental model equations given in equations (4.1) and (4.2) can be extended to include spatial variations in a straightforward manner. Let $\Omega \subset \mathbb{R}^3$ denote the domain of interest, and $\boldsymbol{\mathcal{C}}(\boldsymbol{r}, t)$ represent the concentration vector in different compartments at location $\boldsymbol{r} \in \Omega$, and at time t; and let $\boldsymbol{\alpha}_n(\boldsymbol{r})$ denote the parameter vector whose elements are the pharmacokinetic rates and volume fractions at location $\boldsymbol{r}$. Then, the compartmental model given in (4.1) and (4.2) can be extended to a spatially-resolved model as follows:

$$\dot{\boldsymbol{\mathcal{C}}}(\boldsymbol{r}, t) = \boldsymbol{\mathcal{K}}(\boldsymbol{\alpha}_n(\boldsymbol{r}))\boldsymbol{\mathcal{C}}(\boldsymbol{r}, t), \tag{4.3}$$

$$a(\boldsymbol{r}, t) = \boldsymbol{\mathcal{V}}(\boldsymbol{\alpha}_n(\boldsymbol{r}))\boldsymbol{\mathcal{C}}(\boldsymbol{r}, t) \quad t \in [T_0, T_1], \quad \boldsymbol{r} \in \Omega, \tag{4.4}$$

where $\dot{\boldsymbol{\mathcal{C}}}$ denotes the elementwise time-derivative of $\boldsymbol{\mathcal{C}}$.

Although our study is applicable to pharmacokinetic modeling of any optical fluorophore, in the following subsection, we will specifically discuss the spatially-resolved pharmacokinetic modeling of ICG using a two-compartment model due to

its relevance to breast cancer studies.

4.1.2 Two-compartment Model for the ICG Pharmacokinetics

Spatially resolved ICG transition between plasma and the EES can be modeled using the following coupled ODEs:

$$\begin{bmatrix} \dot{C}_e(\boldsymbol{r},t) \\ \dot{C}_p(\boldsymbol{r},t) \end{bmatrix} = \begin{bmatrix} -k_{out}(\boldsymbol{r}) & k_{in}(\boldsymbol{r}) \\ k_{out}(\boldsymbol{r}) & -(k_{in}+k_{elm})(\boldsymbol{r}) \end{bmatrix} \begin{bmatrix} C_e(\boldsymbol{r},t) \\ C_p(\boldsymbol{r},t) \end{bmatrix}, \quad t \in [T_0,T_1], \quad \boldsymbol{r} \in \Omega, \tag{4.5}$$

where $k_{in}(\boldsymbol{r})$ and $k_{out}(\boldsymbol{r})$ are the spatially-resolved pharmacokinetic-rates that govern the leakage into and the drainage out of the EES, $k_{elm}(\boldsymbol{r})$ describes the ICG elimination from the body through kidneys and liver. The vector $\boldsymbol{\mathcal{C}}(\boldsymbol{r},t)$ in (4.3) and (4.4) is composed of $C_p(\boldsymbol{r},t)$, and $C_e(\boldsymbol{r},t)$, representing the ICG concentration in plasma and the EES at $\boldsymbol{r} \in \Omega$ and $t \in [T_0,T_1]$, respectively.

The ICG concentration in tissue, $a(\boldsymbol{r},t)$, is given as a linear combination of the ICG concentration in plasma and the EES

$$a(\boldsymbol{r},t) = v_p(\boldsymbol{r})C_p(\boldsymbol{r},t) + v_e(\boldsymbol{r})C_e(\boldsymbol{r},t) \quad t \in [T_0,T_1], \quad \boldsymbol{r} \in \Omega, \tag{4.6}$$

where $v_p(\boldsymbol{r})$, $v_e(\boldsymbol{r})$ are spatially-resolved plasma and EES volume fractions, respectively. Here, the unknowns are concentrations in different compartments, pharmacokinetic rates, and volume fractions.

We combine all the pharmacokinetic parameters into a single vector and define

$$\boldsymbol{\alpha}_2(\boldsymbol{r}) = [k_{in}(\boldsymbol{r}) \quad k_{out}(\boldsymbol{r}) \quad k_{elm}(\boldsymbol{r}) \quad v_p(\boldsymbol{r}) \quad v_e(\boldsymbol{r})]^T. \tag{4.7}$$

4.2 Concentration-to-Measurement Map for FDOT

In this work, the quantity we wish to reconstruct is the spatially resolved pharmacokinetic-rate images from a sequence of boundary measurements obtained by diffuse optical tomographic methods. To do this, we first develop a map which

relates sequence of boundary measurements to the spatially resolved fluorophore concentrations. We call this map *concentration-to-measurement* (CTM) map.

A suitable CTM map can be developed based on a photon propagation model in fluorescing medium. We use diffusion approximation of radiative transfer equation to model photon propagation where the propagation of excitation and emission light are modeled by two coupled diffusion equations.

To relate time-varying fluorophore concentrations to a sequence of boundary measurements, we parameterize time evolution of the fluorophore concentration by a slow-time parameter t; and photon propagation during one instance of a tomographic data collection process by a fast-time parameter t'. Note that t' is in the order of the speed of light whereas t is in the order of seconds. Thus, we assume that the absorption and scattering coefficients of tissue are constant during one instance of the tomographic data collection period but vary with the slow-time variable t. As a result, frequency domain couple diffusion equation is adequate to model light propagation during the dynamic data collection process. Figure 4.1 illustrates a typical time evolution of the fluorophore concentration with respect to slow-time variable t.

In the following subsections, for notational brevity, we drop the slow-time dependence in our equations and set $a(\boldsymbol{r},t) = a(\boldsymbol{r})$, $\mu_{axf}(\boldsymbol{r},t) = \mu_{axf}(\boldsymbol{r})$, $\phi_{x,m}(\boldsymbol{r},\omega,t) = \phi_{x,m}(\boldsymbol{r},\omega)$, etc. Note that the subindex in $B_{x,m}$ is a standard notation to denote the quantity B at both excitation and emission wavelengths.

4.2.1 Model for Light Propagation in Fluorescing Medium

The light propagation at the excitation and emission wavelengths can be modelled by the following coupled diffusion equations: [145]:

$$-\nabla\cdot D_x(\boldsymbol{r})\nabla\phi_x(\boldsymbol{r},\omega)+\left(\mu_{ax}(\boldsymbol{r})+\frac{j\omega}{c}\right)\phi_x(\boldsymbol{r},\omega) = S(\boldsymbol{r},\omega), \quad \boldsymbol{r}\in\Omega\subset\mathbb{R}^3 \tag{4.8}$$

$$\begin{aligned}-\nabla\cdot D_m(\boldsymbol{r})\nabla\phi_m(\boldsymbol{r},\omega)+\left(\mu_{am}(\boldsymbol{r})+\frac{j\omega}{c}\right)\phi_m(\boldsymbol{r},\omega) &= -\phi_x(\boldsymbol{r},\omega)\gamma\mu_{axf}(\boldsymbol{r})\\ &\quad\cdot\frac{1-j\omega\tau(\boldsymbol{r})}{1+[\omega\tau(\boldsymbol{r})]^2}.\end{aligned} \tag{4.9}$$

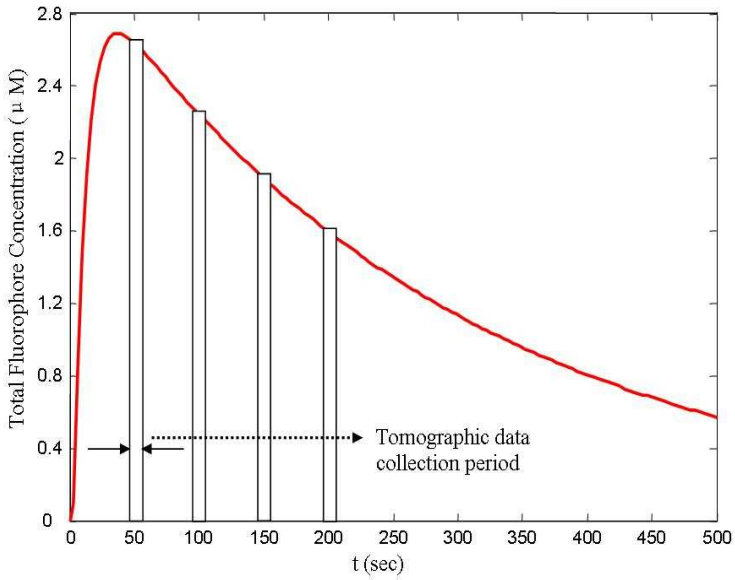

Figure 4.1: Total fluorophore concentration versus slow-time variable, t.

where the subscripts x and m denote the excitation and emission wavelengths, respectively. $\phi_{x,m}(\boldsymbol{r},\omega)$ represents the spatially varying optical field in the medium; ω denotes the modulation frequency of the source (the Fourier transform with respect to the fast-time variable t'); c is the speed of light inside the medium Ω; $\tau(\boldsymbol{r})$ is the fluorophore lifetime; γ is the fluorophore's quantum efficiency; $\mu_{ax,m}(\boldsymbol{r})$ stands for the spatially varying absorption coefficient of the medium at the excitation and emission wavelengths, respectively, $\mu_{axf}(\boldsymbol{r})$ is the fluorophore's absorption coefficient; and $\gamma\mu_{axf}(\boldsymbol{r})$ is the fluorophore yield; $S(\boldsymbol{r},\omega)$ is the excitation source, $D_{x,m}(\boldsymbol{r})$ is the spatially varying diffusion coefficient given by $D_{x,m}(\boldsymbol{r}) = \frac{1}{3\left[\mu'_{sx,m}(\boldsymbol{r})+\mu_{ax,m}(\boldsymbol{r})\right]}$, where $\mu'_{sx,m}(\boldsymbol{r})$ is the reduced scattering coefficient.

The optical coefficients at the excitation and emission wavelengths are due to both the endogenous chromophores and exogenous fluorophore. Thus,

$$\mu_{ax}(\boldsymbol{r}) = \mu_{axe}(\boldsymbol{r}) + \mu_{axf}(\boldsymbol{r}), \tag{4.10}$$

$$\mu_{am}(\boldsymbol{r}) = \mu_{ame}(\boldsymbol{r}) + \mu_{amf}(\boldsymbol{r}). \tag{4.11}$$

Here, the subscript e denotes the endogenous chromophores, and the subscript f denotes the exogenous fluorophore.

We choose Robin-type boundary conditions given as [190]

$$\begin{aligned} 2D_x(\boldsymbol{r})\frac{\partial\phi_x(\boldsymbol{r},\omega)}{\partial\nu} + \rho\phi_x(\boldsymbol{r},\omega) &= 0, \quad \boldsymbol{r}\in\partial\Omega & (4.12)\\ 2D_m(\boldsymbol{r})\frac{\partial\phi_m(\boldsymbol{r},\omega)}{\partial\nu} + \rho\phi_m(\boldsymbol{r},\omega) &= 0, & (4.13)\end{aligned}$$

where $\partial\Omega$ denotes the boundary of Ω, ν denotes the outward normal of the boundary $\partial\Omega$, ρ is a constant accounting for the refractive index mismatch between the two regions separated by $\partial\Omega$.

Let $a(\boldsymbol{r})$ denote the concentration of fluorophores at $\boldsymbol{r} \in \Omega$. The relationship between $a(\boldsymbol{r})$ and the fluorophore absorption coefficient, $\mu_{a(x,m)f}$, is given by [46]

$$\mu_{a(x,m)f}(\boldsymbol{r}) = \ln 10\epsilon_{x,m}a(\boldsymbol{r}) \quad \boldsymbol{r}\in\Omega, \tag{4.14}$$

where $\epsilon_{x,m}$ denotes the fluorophore extinction coefficients at the excitation and emission wavelengths, respectively.

4.2.2 Non-linear Concentration-to-Measurement Map

Let $\Phi_m(\boldsymbol{r}_d, \boldsymbol{r}_s; \omega)$ denote the ratio of the emission data to the excitation data (normalized Born data [190]) at the emission wavelength at the detector location $\boldsymbol{r}_d$ due to an excitation source at $\boldsymbol{r}_s$. The relationship between $\Phi_m(\boldsymbol{r}_d, \boldsymbol{r}_s; \omega)$ and $a(\boldsymbol{r})$ is given by

$$\begin{aligned}\Phi_m(\boldsymbol{r}_d,\boldsymbol{r}_s;\omega) &= \frac{\ln 10\epsilon_x\gamma}{\phi_x(\boldsymbol{r}_d,\boldsymbol{r}_s;\omega)}\int_\Omega G_m(\boldsymbol{r}_d,\boldsymbol{r};\omega)a(\boldsymbol{r})\frac{1-j\omega\tau(\boldsymbol{r})}{1+[\omega\tau(\boldsymbol{r})]^2}\phi_x(\boldsymbol{r},\boldsymbol{r}_s;\omega)d^3\boldsymbol{r}\\ &=: \mathcal{F}_{\boldsymbol{r}_d,\boldsymbol{r}_s}(a)\end{aligned} \tag{4.15}$$

where $\phi_x(\boldsymbol{r}, \boldsymbol{r}_s; \omega)$ is the photon density at location $\boldsymbol{r}$ due to a source at $\boldsymbol{r}_s$ at the excitation wavelength; $G_m(\boldsymbol{r}_d, \boldsymbol{r}; \omega)$ is the Green's function of (4.9) and (4.13) at $\boldsymbol{r}_d$, due to a point source at $\boldsymbol{r}$, and $\mathcal{F}_{\boldsymbol{r}_d,\boldsymbol{r}_s}(a)$ is the non-linear operator that maps the total fluorophore concentration a to the normalized measurements Φ_m. Note

that the non-linearity in (4.15) is due to the μ_{amf} dependence of $G_m(\boldsymbol{r}_d, \boldsymbol{r}; \omega)$, and $\mu_{a(m,x)}$ dependence of ϕ_x.

We assume that: *i*) The endogenous absorption coefficients at the emission and the excitation wavelengths are approximately equal, i.e. $\mu_{ame} \approx \mu_{axe}$. This is a valid assumption for a number of different applications such as small animal and breast imaging [182]. *ii*) The diffusion coefficients at both the excitation and emission wavelengths are independent of the endogenous and exogenous absorption coefficients, i.e. $D_{x,m}(\boldsymbol{r}) \approx 1/(3\mu'_{sx,m}(\boldsymbol{r}))$. Furthermore, the diffusion coefficients are known but can be spatially varying. *iii*) The lifetime parameter, $\tau(\boldsymbol{r})$, $\boldsymbol{r} \in \Omega$, is known, and not necessarily constant.

Let N_d and N_s denote the number of detectors and sources, respectively. Let $\boldsymbol{\Phi}$ be the measurement vector formed by concatenating the measurements for each source-detector pair as follows:

$$\boldsymbol{\Phi} = [\Phi_m(\boldsymbol{r}_{d_1}, \boldsymbol{r}_{s_1}; \omega), \cdots, \Phi_m(\boldsymbol{r}_{d_{Nd}}, \boldsymbol{r}_{s_1}; \omega), \cdots, \Phi_m(\boldsymbol{r}_{d_{Nd}}, \boldsymbol{r}_{s_{Ns}}; \omega)]^T. \tag{4.16}$$

Using (4.15) and (4.16), we form the following relationship between a and $\boldsymbol{\Phi}$:

$$\boldsymbol{\Phi} =: \boldsymbol{\mathcal{F}}(a), \tag{4.17}$$

where $\boldsymbol{\mathcal{F}}$ is an operator with matrix kernel in which $\boldsymbol{\mathcal{F}}_{ij} = \mathcal{F}_{\boldsymbol{r}_{d_i}, \boldsymbol{r}_{s_j}}$ for $i = 1, \cdots, N_d$, $j = 1, \cdots, N_s$.

Note that for notational brevity, we assume a single-frequency measurement model. A multi-frequency measurement model is a straightforward extension of the single-frequency measurement model.

4.2.3 Linear Concentration-to-Measurement Map

An approximate linear map between the normalized measurements and the total fluorophore concentration can be obtained based on the assumption that the presence of exogenous fluorophores does not change the optical coefficients $\mu_{ax,m}$ and $D_{x,m}$ [145]. This assumption leads to the following relationship between the

measurements and the fluorophore concentrations:

$$\begin{aligned}\Phi_m(\boldsymbol{r}_d,\boldsymbol{r}_s;\omega) &= \frac{\ln 10\epsilon_x\gamma}{\phi_x^e(\boldsymbol{r}_d,\boldsymbol{r}_s;\omega)}\int_\Omega G_m^e(\boldsymbol{r}_d,\boldsymbol{r};\omega)a(\boldsymbol{r})\frac{1-j\omega\tau(\boldsymbol{r})}{1+[\omega\tau(\boldsymbol{r})]^2}\phi_x^e(\boldsymbol{r},\boldsymbol{r}_s;\omega)d^3\boldsymbol{r} \\ &=: \mathcal{W}_{\boldsymbol{r}_d,\boldsymbol{r}_s}(a),\end{aligned} \tag{4.18}$$

where $G_m^e(\boldsymbol{r}_d,\boldsymbol{r};\omega)$ is the Green's function of (4.9) and (4.13) when $\mu_{am}=\mu_{ame}$, $\phi_x^e(\boldsymbol{r},\boldsymbol{r}_s;\omega)$ is the predicted optical field at $\boldsymbol{r}$ due to a source located at $\boldsymbol{r}_s$ when $\mu_{ax}=\mu_{axe}$, and $\mathcal{W}_{\boldsymbol{r}_d,\boldsymbol{r}_s}(a)$ denotes the linear operator that maps the normalized measurement at $\boldsymbol{r}_d$ due to a source at $\boldsymbol{r}_s$ to the total fluorophore concentration.

Forming a measurement vector as in (4.16), we write

$$\boldsymbol{\Phi} =: \boldsymbol{\mathcal{W}}(a) \tag{4.19}$$

where $\boldsymbol{\mathcal{W}}$ is the linear operator with a matrix kernel in which $\boldsymbol{\mathcal{W}}_{ij}=\mathcal{W}_{\boldsymbol{r}_{d_i},\boldsymbol{r}_{s_j}}$ for $i=1,\cdots,N_d \quad j=1,\cdots,N_s$.

Note that the reconstruction of the pharmacokinetic-rate images that will be discussed in the subsequent sections is not tied to any specific linearization method. Alternatively, a different linear approximation to $\boldsymbol{\mathcal{F}}$ can be obtained by computing its first-order Fréchet derivative to yield a relationship between measurements and total fluorophore concentration. However, we adopted the model in (4.19) for image reconstruction using *in vivo* breast data.

4.3 Pharmacokinetic-rates-to-Measurement Map

In this section, we combine the CTM map with the spatially resolved compartmental model to obtain a mapping between the spatially resolved pharmacokinetic-rates and sequence of boundary measurements. We call this composite map the *pharmacokinetic-rate-to-measurement* (PTM) map.

Recall that

$$\dot{\boldsymbol{\mathcal{C}}}(\boldsymbol{r},t)=\boldsymbol{\mathcal{K}}(\boldsymbol{\alpha}_n(\boldsymbol{r}))\boldsymbol{\mathcal{C}}(\boldsymbol{r},t) \quad t\in[T_0,T_1], \quad \boldsymbol{r}\in\Omega. \tag{4.20}$$

Let $\boldsymbol{\Phi}(t)$ denote the measurement vector (16) and $a(\boldsymbol{r},t)$ denote the flourophore

concentration at slow-time parameter t. Combining the CTM map (4.17) with the compartmental model (4.4), we obtain the following non-linear relationship:

$$\boldsymbol{\Phi}(t) = \boldsymbol{\mathcal{F}}(\boldsymbol{\mathcal{V}}(\boldsymbol{\alpha}_n(\boldsymbol{r}))\boldsymbol{\mathcal{C}}(\boldsymbol{r},t)), \quad t \in [T_0, T_1], \quad \boldsymbol{r} \in \Omega. \tag{4.21}$$

For the linear CTM map, (4.21) becomes

$$\boldsymbol{\Phi}(t) = \boldsymbol{\mathcal{W}}(\boldsymbol{\mathcal{V}}(\boldsymbol{\alpha}_n(\boldsymbol{r}))\boldsymbol{\mathcal{C}}(\boldsymbol{r},t)) \quad t \in [T_0, T_1], \quad \boldsymbol{r} \in \Omega. \tag{4.22}$$

The equations (4.20) & (4.21) and (4.20) & (4.22) constitute the PTM map. We next discretize these equations and incorporate dynamic model uncertainties and measurement noise to the PTM map.

We use first-order Lagrange basis to discretize the domain of interest Ω (see Section 4.5.2). Let $\boldsymbol{r}_j$, $j = 1, ..., N$ be the discrete points representing the spatial location of the voxels in Ω. Let $\boldsymbol{\mathcal{C}}(\boldsymbol{r}_j, t)$ represent the concentration vector at time t in different compartments, and $\boldsymbol{\alpha}_n(\boldsymbol{r}_j)$ represent the pharmacokinetic-rates and volume fractions at the j^{th} voxel centered at $\boldsymbol{r}_j$, $j = 1, ..., N$. Assuming that the dynamic measurements are collected at time instances, $t = k\Delta$, $k = 1, ..., K$, where Δ is the sampling period, we define $\mathbf{C}(\boldsymbol{r}_j, k) = \boldsymbol{\mathcal{C}}(\boldsymbol{r}_j, k\Delta)$, and express the discrete spatially resolved compartmental model as follows:

$$\mathbf{C}(\boldsymbol{r}_j, k+1) = \mathbf{K}(\boldsymbol{\theta}_n(\boldsymbol{r}_j))\mathbf{C}(\boldsymbol{r}_j, k) + \boldsymbol{\xi}(\boldsymbol{r}_j, k), \quad k = 1, ...K, \quad j = 1, ...N, \tag{4.23}$$

where $\boldsymbol{\xi}(\boldsymbol{r}_j, k)$ is a zero-mean Gaussian process with $E[\boldsymbol{\xi}(\boldsymbol{r}_j, k_1)\boldsymbol{\xi}(\boldsymbol{r}_i, k_2)] = \delta(\boldsymbol{r}_j - \boldsymbol{r}_i)\delta(k_1 - k_2)\mathbf{Q}_n$, representing the dynamic model uncertainty; $\mathbf{K}(\boldsymbol{\theta}_n(\boldsymbol{r}_j)) := e^{\boldsymbol{\mathcal{K}}(\boldsymbol{\alpha}_n(\boldsymbol{r}_j))\Delta}$ is the discrete-time system matrix as described in [111] and, $\boldsymbol{\theta}_n(\boldsymbol{r}_j)$ represents the discrete-time parameter vector for the pharmacokinetic-rates and volume fractions. For a detailed discussion of the discretization procedure and an explicit relationship between the parameters $\boldsymbol{\theta}_n(\boldsymbol{r}_j)$ and $\boldsymbol{\alpha}_n(\boldsymbol{r}_j)$, see [25, 111].

Let $\boldsymbol{\Psi}(k) = \boldsymbol{\Phi}(k\Delta)$. Replacing $\boldsymbol{\alpha}_n(\boldsymbol{r}_j)$ with $\boldsymbol{\theta}_n(\boldsymbol{r}_j)$, (4.21) and (4.22) are

discretized as:

$$\boldsymbol{\Psi}(k) = \mathbf{F}(\mathbf{V}(\boldsymbol{\theta}_n(\boldsymbol{r}_j))\mathbf{C}(\boldsymbol{r}_j,k)) + \boldsymbol{\eta}(k), \tag{4.24}$$

$$\boldsymbol{\Psi}(k) = \mathbf{W}\mathbf{V}(\boldsymbol{\theta}_n(\boldsymbol{r}_j))\mathbf{C}(\boldsymbol{r}_j,k) + \boldsymbol{\eta}(k), \quad k=1,...K, \quad j=1,...N, \tag{4.25}$$

where $\mathbf{F}$ and $\mathbf{W}$ are the resulting operators when $\boldsymbol{\alpha}_n(\boldsymbol{r}_j)$ is replaced with $\boldsymbol{\theta}_n(\boldsymbol{r}_j)$ in (4.15) and (4.18), respectively; $\boldsymbol{\eta}(k)$ is a zero-mean Gaussian process with $E[\boldsymbol{\eta}(k_1)\boldsymbol{\eta}(k_2)] = \delta(k_1-k_2)\mathbf{R}$ representing the measurement noise, and $\mathbf{V}(\boldsymbol{\theta}_n(\boldsymbol{r}_j))$ is the vector of discrete volume fractions at $\boldsymbol{r}_j$.

For the two-compartment ICG pharmacokinetic model combined with the linear CTM map, the explicit form of (4.23) and (4.25) are given by

$$\begin{bmatrix} C_e(\boldsymbol{r}_j,k+1) \\ C_p(\boldsymbol{r}_j,k+1) \end{bmatrix} = \begin{bmatrix} \tau_{11}(\boldsymbol{r}_j) & \tau_{12}(\boldsymbol{r}_j) \\ \tau_{21}(\boldsymbol{r}_j) & \tau_{22}(\boldsymbol{r}_j) \end{bmatrix} \begin{bmatrix} C_e(\boldsymbol{r}_j,k) \\ C_p(\boldsymbol{r}_j,k) \end{bmatrix} + \begin{bmatrix} \xi_e(\boldsymbol{r}_j,k) \\ \xi_p(\boldsymbol{r}_j,k) \end{bmatrix}, \quad k=1,\ldots,K \tag{4.26}$$

$$\boldsymbol{\Psi}(k) = \mathbf{W} \begin{bmatrix} v_e(\boldsymbol{r}_j) & v_p(\boldsymbol{r}_j) \end{bmatrix} \begin{bmatrix} C_e(\boldsymbol{r}_j,k) \\ C_p(\boldsymbol{r}_j,k) \end{bmatrix} + \boldsymbol{\eta}(k), \quad k=1,\ldots,K \tag{4.27}$$

where $\mathbf{C}(\boldsymbol{r}_j,k) = [C_e(\boldsymbol{r}_j,k) \;\; C_p(\boldsymbol{r}_j,k)]^T$, $\boldsymbol{\xi}(\boldsymbol{r}_j,k) = [\xi_e(\boldsymbol{r}_j,k) \;\; \xi_p(\boldsymbol{r}_j,k)]^T$, $\mathbf{V}(\boldsymbol{\theta}_2(\boldsymbol{r}_j)) = [v_e(\boldsymbol{r}_j) \;\; v_p(\boldsymbol{r}_j)]$, $\boldsymbol{\theta}_2(\boldsymbol{r}_j) = [\tau_{11}(\boldsymbol{r}_j) \;\; \tau_{12}(\boldsymbol{r}_j) \;\; \tau_{21}(\boldsymbol{r}_j) \;\; \tau_{22}(\boldsymbol{r}_j) \;\; v_e(\boldsymbol{r}_j) \;\; v_p(\boldsymbol{r}_j)]^T$, and $\mathbf{K}(\boldsymbol{\theta}_n(\boldsymbol{r}_j))$ is the 2-by-2 system matrix in (4.26), for $j=1,...,N$ and $k=1,...,K$.

4.4 Reconstruction of Pharmacokinetic Rate and Concentration Images from the Boundary Measurements

The forward model in (4.23) and (4.24)/(4.25) forms a state-space model, (4.23) being the state equation and (4.24)/(4.25) being the measurement equation. In this section, we discuss the estimation of the system parameters, $\boldsymbol{\theta}_n(\boldsymbol{r}_j)$, and the states $\mathbf{C}_d(\boldsymbol{r}_j,k)$ for $j=1,\ldots,N$, from the measurements $\boldsymbol{\Psi}(k)$, $k=1,\ldots,K$ using the extended Kalman filtering (EKF) framework. The advantages of Kalman

filtering framework for the estimation of pharmacokinetics-rates, volume fractions and concentrations in different compartments are well discussed in the Introduction Section of this Thesis.

Note that both the fluorophore concentrations in different compartments, $\mathbf{C}(\boldsymbol{r}_j, k)$, and the system parameters, $\boldsymbol{\theta}_n(\boldsymbol{r}_j)$, are unknown. In this case, we estimate both the states and system parameters from measurements within the EKF framework. To do so, we regard the state equation in (4.23) as a non-linear equation in which the system parameters and states are combined to form the new states of the non-linear equation. We then iteratively linearize the non-linear state equation and solve for the new unknown states using the EKF framework. This approach requires use of temporal prior models on $\boldsymbol{\theta}_n(\boldsymbol{r}_j)$. We describe one such model in the following subsection.

4.4.1 A priori Model for Pharmacokinetic-rates and Volume Fractions

To impose a temporal prior model on $\boldsymbol{\theta}_n(\boldsymbol{r}_j)$, we extend our notation to $\boldsymbol{\theta}_n(\boldsymbol{r}_j, k)$, $k = 1, \ldots, K$. Note that $\boldsymbol{\theta}_n(\boldsymbol{r}_j, k)$ is a vector containing pharmacokinetic-rates and volume fractions at location $\boldsymbol{r}_j \in \Omega$ and time $k\Delta$. For each element, $\tilde{\theta_n}(\boldsymbol{r}_j, k)$, of the vector $\boldsymbol{\theta}_n(\boldsymbol{r}_j, k)$, we impose the following dynamic model:

$$\tilde{\theta_n}(\boldsymbol{r}_j, k+1) = \tilde{\theta_n}(\boldsymbol{r}_j, k) + \tilde{\varsigma_1}(\boldsymbol{r}_j, k) \tag{4.28}$$

where $\tilde{\varsigma_1}(\boldsymbol{r}_j, k)$ is a zero-mean Gaussian process with $E[\tilde{\varsigma_1}(\boldsymbol{r}_1, k_1)\tilde{\varsigma_1}(\boldsymbol{r}_2, k_2)] = \delta(\boldsymbol{r}_1 - \boldsymbol{r}_2)\delta(k_1 - k_2)z_1$, $z_1 > 0$.

Note that $\boldsymbol{\theta}_n(\boldsymbol{r}_j)$ is modeled as a time-independent parameter, and the model in (4.28) relates $\tilde{\theta_n}(\boldsymbol{r}_j, k+1)$ and $\tilde{\theta_n}(\boldsymbol{r}_j, k)$ with an all-pass filter. If, on the other hand, $\boldsymbol{\theta}_n(\boldsymbol{r}_j)$ is time-dependent, a different filter can be chosen based on *a priori* physiological information and/or robustness considerations.

In addition to the temporal prior, we impose a spatial smoothing prior on $\boldsymbol{\theta}_n(\boldsymbol{r}_j, k)$ to improve the robustness of the reconstruction with respect to measurement noise and to incorporate *a priori* physiological information into image reconstruction. This model is given as

$$\tilde{\theta_n}(\boldsymbol{r}_j,k) = \sum_{l=1(j_l\neq j)}^{M} \tilde{\beta_l}\tilde{\theta_n}(\boldsymbol{r}_{j_l},k) + \tilde{\varsigma_2}(\boldsymbol{r}_j,k), \quad j=1,\ldots,N \tag{4.29}$$

where j_l, $l=1,\ldots,M$ $(j_l \neq j)$ are the indices of the voxels in the neighborhood of the j^{th} voxel; $\tilde{\beta_l}$, $l=1,\ldots,M$ are the spatial weighting coefficients, which may be different for each pharmacokinetic-rate or volume fraction image; and $\tilde{\varsigma_2}(\boldsymbol{r}_j,k)$, is a zero-mean Gaussian process with $E[\tilde{\varsigma_2}(\boldsymbol{r}_1,k_1)\tilde{\varsigma_2}(\boldsymbol{r}_2,k_2)] = \delta(\boldsymbol{r}_1-\boldsymbol{r}_2)\delta(k_1-k_2)z_2$, $z_2>0$.

The weighting coefficients $\tilde{\beta_l}$ may be spatially varying and can be chosen based on a variety of physiological information, i.e., tumor location, size or shape. In our numerical simulations and *in vivo* data processing, we assumed that no such specific information about the tumor is available and used equal weights, i.e., $\tilde{\beta_l} = 1/M$. This choice imposes an isotropic smoothing on the $\tilde{\theta_n}(\boldsymbol{r}_j,k)$ estimates.

Inserting the right-hand side of (4.29) for $\tilde{\theta_n}(\boldsymbol{r}_j,k)$ in (4.28), we obtain the following spatio-temporal model for each entry $\tilde{\theta_n}(\boldsymbol{r}_j,k)$ of the vector $\boldsymbol{\theta}_n(\boldsymbol{r}_j,k)$:

$$\tilde{\theta_n}(\boldsymbol{r}_j,k+1) = \sum_{l=1(j_l\neq j)}^{M} \tilde{\beta_l}\tilde{\theta_n}(\boldsymbol{r}_{j_l},k) + \tilde{\varsigma}(\boldsymbol{r}_j,k), \quad k=1,...K, \;\; j=1,...N, \tag{4.30}$$

where $\tilde{\varsigma}(\boldsymbol{r}_j,k)$ is a zero-mean Gaussian process with $E[\tilde{\varsigma}(\boldsymbol{r}_1,k_1)\tilde{\varsigma}(\boldsymbol{r}_2,k_2)] = \delta(\boldsymbol{r}_1-\boldsymbol{r}_2)\delta(k_1-k_2)z$, $z>0$, and z is a function of z_1 and z_2. Figure 4.2 illustrates the resulting neighborhood system for 2D images for $M=4$.

Note that it is possible to develop alternative spatio-temporal neighborhood system taking into account the 4D nature of the measurements.

To simplify our notation, we express (4.30) in vector notation for all entries of the vector $\boldsymbol{\theta}_n(\boldsymbol{r}_j,k)$ as follows:

$$\boldsymbol{\theta}_n(\boldsymbol{r}_j,k+1) = \boldsymbol{\beta}_j(\boldsymbol{\theta}_n(\boldsymbol{r}_{j_1},k),...,\boldsymbol{\theta}_n(\boldsymbol{r}_{j_M},k)) + \boldsymbol{\varsigma}(\boldsymbol{r}_j,k), \quad k=1,...K, \;\; j=1,...N, \tag{4.31}$$

where $\boldsymbol{\beta}_j$ is a vector-valued linear function of $\boldsymbol{\theta}_n(\boldsymbol{r}_{j_l},k)$, $l=1...,M$ as defined in (4.30) and $\boldsymbol{\varsigma}(\boldsymbol{r}_j,k)$ is formed by concatenating the $\tilde{\varsigma}(\boldsymbol{r}_j,k)$ into a column vector. It

is a zero-mean Gaussian process with $E[\boldsymbol{\varsigma}(\boldsymbol{r}_1, k_1)\boldsymbol{\varsigma}(\boldsymbol{r}_2, k_2)] = \delta(\boldsymbol{r}_1 - \boldsymbol{r}_2)\delta(k_1 - k_2)\mathbf{Z}_1$.

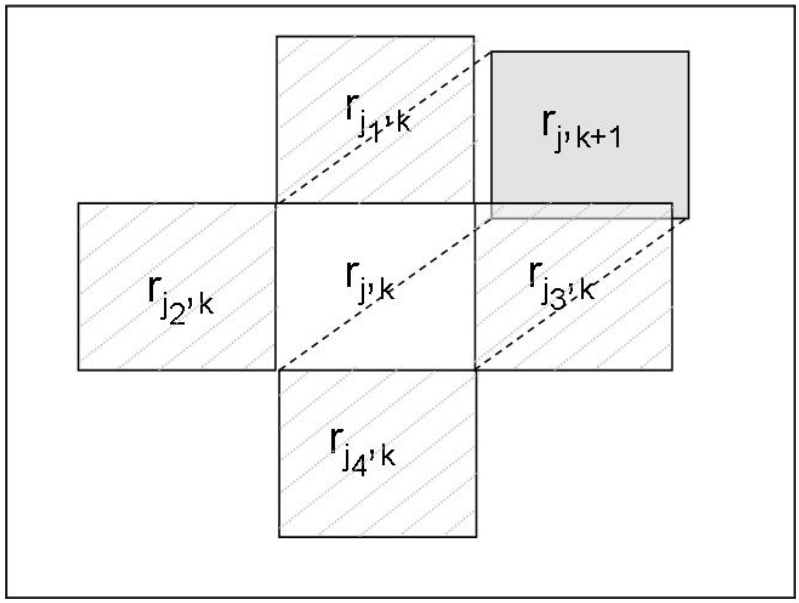

Figure 4.2: An illustration of the spatio-temporal neighborhood system for 2-D pharmacokinetic-rate and volume fraction images for M=4. Based on the model in (4.28) to (4.30) the neighborhood of the voxel at $r_{j,k+1}$ (gray square) is given by the voxels at $r_{j_1,k}$, $r_{j_2,k}$, $r_{j_3,k}$, and $r_{j_4,k}$ denoted by gray-dashed squares.

4.4.2 Estimation of Pharmacokinetic-Rate Images by Extended Kalman Filtering

Our objective is to estimate the fluorophore concentration images in different compartments, and pharmacokinetic-rate images. To do so, we first concatenate the concentration vectors $\mathbf{C}(\boldsymbol{r}_j, k)$ and the parameter vectors $\boldsymbol{\theta}_n(\boldsymbol{r}_j, k)$ for all voxels, $j = 1, ..., N$ and form the following vectors:

$$\mathbf{C}(k) = \left[\begin{array}{ccc} \mathbf{C}(\boldsymbol{r}_1, k) & \dots & \mathbf{C}(\boldsymbol{r}_N, k) \end{array} \right]^T,$$

$$\boldsymbol{\theta}_n(k) = \left[\begin{array}{ccc} \boldsymbol{\theta}_n(\boldsymbol{r}_1, k) & \dots & \boldsymbol{\theta}_n(\boldsymbol{r}_N, k) \end{array} \right]^T.$$

Next, we concatenate the vectors $\mathbf{C}(k)$ and $\boldsymbol{\theta}_n(k)$ and form the new state-space model based on (4.23) and (4.31).

$$\begin{bmatrix} \mathbf{C}(k+1) \\ \boldsymbol{\theta}_n(k+1) \end{bmatrix} = \begin{bmatrix} \mathbf{K}(\boldsymbol{\theta}_n(k))\mathbf{C}(k) \\ \boldsymbol{\beta}(\boldsymbol{\theta}_n(k)) \end{bmatrix} + \begin{bmatrix} \boldsymbol{\xi}(k) \\ \boldsymbol{\varsigma}(k) \end{bmatrix} \tag{4.32}$$

$$\boldsymbol{\Psi}(k) = \begin{bmatrix} \mathbf{F}(\mathbf{V}(\boldsymbol{\theta}_n(k))\mathbf{C}(k)) & 0 \end{bmatrix} \begin{bmatrix} 1 \\ \boldsymbol{\theta}_n(k) \end{bmatrix} + \boldsymbol{\eta}(k) \tag{4.33}$$

$$\boldsymbol{\Psi}(k) = \begin{bmatrix} \ln 10\epsilon_x \mathbf{W}\mathbf{V}(\boldsymbol{\theta}_n(k))\mathbf{C}(k) & 0 \end{bmatrix} \begin{bmatrix} 1 \\ \boldsymbol{\theta}_n(k) \end{bmatrix} + \boldsymbol{\eta}(k) \tag{4.34}$$

where

$$\begin{aligned} \mathbf{K}(\boldsymbol{\theta}_n(k))\mathbf{C}(k) &= \begin{bmatrix} \mathbf{K}(\boldsymbol{\theta}_n(\boldsymbol{r}_1,k))\mathbf{C}(\boldsymbol{r}_1,k) & \dots & \mathbf{K}(\boldsymbol{\theta}_n(\boldsymbol{r}_N,k))\mathbf{C}(\boldsymbol{r}_N,k) \end{bmatrix}^T \\ \boldsymbol{\beta}(\boldsymbol{\theta}_n(k)) &= \begin{bmatrix} \boldsymbol{\beta}_1(\boldsymbol{\theta}_n(\boldsymbol{r}_1,k),...) & \dots & \boldsymbol{\beta}_N(\boldsymbol{\theta}_n(\boldsymbol{r}_N,k),...) \end{bmatrix}^T \\ \mathbf{F}(\mathbf{V}(\boldsymbol{\theta}_n(k))\mathbf{C}(k)) &= \begin{bmatrix} \mathbf{F}(\mathbf{V}(\boldsymbol{\theta}_n(\boldsymbol{r}_1,k))\mathbf{C}(\boldsymbol{r}_1,k)) & \dots & \mathbf{F}(\mathbf{V}(\boldsymbol{\theta}_n(\boldsymbol{r}_N,k))\mathbf{C}(\boldsymbol{r}_N,k)) \end{bmatrix}^T \\ \boldsymbol{\xi}(k) &= \begin{bmatrix} \boldsymbol{\xi}(\boldsymbol{r}_1,k) & \dots & \boldsymbol{\xi}(\boldsymbol{r}_N,k) \end{bmatrix}^T \\ \boldsymbol{\varsigma}(k) &= \begin{bmatrix} \boldsymbol{\varsigma}(\boldsymbol{r}_1,k) & \dots & \boldsymbol{\varsigma}(\boldsymbol{r}_N,k) \end{bmatrix}^T \end{aligned} \tag{4.35}$$

where $\boldsymbol{\xi}(k)$ and $\boldsymbol{\varsigma}(k)$ are zero-mean Gaussian processes with covariance matrices $\mathbf{Q}$ and $\mathbf{Z}$, respectively. $\boldsymbol{\eta}(k)$ is the zero-mean Gaussian process with covariance matrix $\mathbf{R}$ as defined before.

Note that although $\boldsymbol{\beta}$ is linear in $\boldsymbol{\theta}_n(\boldsymbol{r}_j,k)$, $j=1,..,N$, (4.32) is non-linear in new states. Furthermore, the state equation (4.32) is not block diagonal.

We next utilize the EKF machinery to estimate the fluorophore concentration images in different compartments and pharmacokinetic-rates based on (4.32) to (4.35). Table 4.1 tabulates the steps of the EKF algorithm. The terms in Table 4.1 are defined as follows: $\hat{\mathbf{C}}(k|k-1)$ and $\hat{\boldsymbol{\theta}}_n(k|k-1)$ are the concentration and parameter estimates at time k given all the measurements up to time $k-1$, respectively. Similarly, $\hat{\mathbf{C}}(k)$ and $\hat{\boldsymbol{\theta}}_n(k)$ are the concentration and parameter estimate updates at time k, respectively. $\mathbf{P}_{k,k-1}$ denotes the error covariance propagation at time k given

Table 4.1: EKF algorithm for the simultaneous estimation of fluorophore concentration, pharmacokinetic-rate and volume fraction images.

System Model	$\begin{bmatrix} \mathbf{C}(k+1) \\ \boldsymbol{\theta}_n(k+1) \end{bmatrix} = \begin{bmatrix} \mathbf{K}(\boldsymbol{\theta}_n(k))\mathbf{C}(k) \\ \boldsymbol{\beta}(\boldsymbol{\theta}_n(k)) \end{bmatrix} + \begin{bmatrix} \boldsymbol{\xi}(k) \\ \boldsymbol{\varsigma}(k) \end{bmatrix}$
Measurement Model	$\boldsymbol{\Psi}(k) = \begin{bmatrix} \mathbf{F}(\mathbf{V}(\boldsymbol{\theta}_n(k))\mathbf{C}(k)) & 0 \end{bmatrix} \begin{bmatrix} 1 \\ \boldsymbol{\theta}_n(k) \end{bmatrix} + \boldsymbol{\eta}(k)$
Initial Conditions	$\begin{bmatrix} \hat{\mathbf{C}}(1) \\ \hat{\boldsymbol{\theta}}_n(1) \end{bmatrix} = \begin{bmatrix} E(\mathbf{C}(1)) \\ \hat{\boldsymbol{\theta}}_n(1) \end{bmatrix}, \qquad \mathbf{P}_{1,1} = \begin{bmatrix} Var(\mathbf{C}(1)) & 0 \\ 0 & \mathbf{Z} \end{bmatrix}$
State Est. Propagation	$\begin{bmatrix} \hat{\mathbf{C}}(k\|k-1) \\ \hat{\boldsymbol{\theta}}_n(k\|k-1) \end{bmatrix} = \begin{bmatrix} \mathbf{K}(\hat{\boldsymbol{\theta}}_n(k-1))\hat{\mathbf{C}}(k-1) \\ \boldsymbol{\beta}(\hat{\boldsymbol{\theta}}_n(k-1)) \end{bmatrix}$
Error Cov. Propagation	$\mathbf{P}_{k,k-1} = \mathbf{J}_{k-1}\mathbf{P}_{k-1,k-1}\mathbf{J}_{k-1}^T + \begin{bmatrix} \mathbf{Q} & 0 \\ 0 & \mathbf{Z} \end{bmatrix}$
State Est. Update	$\begin{bmatrix} \hat{\mathbf{C}}(k) \\ \hat{\boldsymbol{\theta}}_n(k) \end{bmatrix} = \begin{bmatrix} \hat{\mathbf{C}}(k\|k-1) \\ \boldsymbol{\beta}(\hat{\boldsymbol{\theta}}_n(k\|k-1)) \end{bmatrix} + \mathbf{H}_k[\boldsymbol{\Psi}(k) - \mathbf{F}(\mathbf{V}(\hat{\boldsymbol{\theta}}_n(k\|k-1))\hat{\mathbf{C}}(k\|k-1))]$
Error Cov. Update	$\mathbf{P}_{k,k} = [\mathbf{I} - \mathbf{H}_k\boldsymbol{\Lambda}_{k\|k-1}]\mathbf{P}_{k,k-1}$
Kalman Gain	$\mathbf{H}_k = \mathbf{P}_{k,k-1}\boldsymbol{\Lambda}_{k\|k-1}^T[\boldsymbol{\Lambda}_{k\|k-1}\mathbf{P}_{k,k-1}\boldsymbol{\Lambda}_{k\|k-1}^T + \mathbf{R}]^{-1}$
Definitions	$\mathbf{J}_{k-1} = \begin{bmatrix} \mathbf{K}(\hat{\boldsymbol{\theta}}_n(k-1)) & \frac{\partial}{\partial \boldsymbol{\theta}}(\mathbf{K}(\hat{\boldsymbol{\theta}}_n(k-1))\hat{\mathbf{C}}(k-1)) \\ \frac{\partial}{\partial \mathbf{C}}\boldsymbol{\beta}(\hat{\boldsymbol{\theta}}_n(k-1) & \frac{\partial}{\partial \boldsymbol{\theta}_n}\boldsymbol{\beta}(\hat{\boldsymbol{\theta}}_n(k-1)) \end{bmatrix}$
	Non-linear Case $\boldsymbol{\Lambda}_{k\|k-1} = \begin{bmatrix} \frac{\partial}{\partial \mathbf{C}}\mathbf{F}(\mathbf{V}(\hat{\boldsymbol{\theta}}_n(k\|k-1))\hat{\mathbf{C}}(k\|k-1)) \\ \frac{\partial}{\partial \boldsymbol{\theta}_n}\mathbf{F}(\mathbf{V}(\hat{\boldsymbol{\theta}}_n(k\|k-1))\hat{\mathbf{C}}(k\|k-1)) \end{bmatrix}^T$
	Linear Case $\boldsymbol{\Lambda}_{k\|k-1} = \begin{bmatrix} \ln 10\epsilon_x\mathbf{W}\frac{\partial}{\partial \mathbf{C}}(\mathbf{V}(\hat{\boldsymbol{\theta}}_n(k\|k-1))\hat{\mathbf{C}}(k\|k-1)) \\ \ln 10\epsilon_x\mathbf{W}\frac{\partial}{\partial \boldsymbol{\theta}_n}(\mathbf{V}(\hat{\boldsymbol{\theta}}_n(k\|k-1))\hat{\mathbf{C}}(k\|k-1)) \end{bmatrix}^T$

all the measurements up to time $k-1$; $\mathbf{P}_{k,k}$ is the error covariance update at time k. $\mathbf{H}_k$ is the recursive Kalman gain matrix at time k and $\mathbf{I}$ is the identity matrix. $\mathbf{J}_{k-1}$ is the Jacobian matrix due to iterative linearization of the (4.32) around $\hat{\mathbf{C}}(k-1)$ and $\hat{\boldsymbol{\theta}}_n(k-1)$. $\boldsymbol{\Lambda}_{k|k-1}$ is the matrix formed by the discretized Fréchet derivatives of $\boldsymbol{\mathcal{F}}$ with respect to $\boldsymbol{\mathcal{C}}$ and $\boldsymbol{\theta}_n$ at the updates $\hat{\mathbf{C}}(k|k-1)$ and $\hat{\boldsymbol{\theta}}_n(k|k-1)$. In Table 4.1, the EKF algorithm is presented for non-linear case. For the linear case, the the non-linear operator $\mathbf{F}$ is replaced by the linear operator $\mathbf{W}$.

The first-order Fréchet derivative of $\boldsymbol{\mathcal{F}}$ (or $\mathcal{F}_{\boldsymbol{r}_d,\boldsymbol{r}_s}$) with respect to the fluorophore concentration a at the EKF total concentration estimate at the $(k|k-1)^{th}$ step is given by [27, 28, 190]

$$\begin{aligned}\partial\mathcal{F}_{\boldsymbol{r}_d,\boldsymbol{r}_s}(\delta a) \;=\; & \frac{\ln 10\epsilon_x}{\Phi_x^{k|k-1}(\boldsymbol{r}_d,\boldsymbol{r}_s;\omega)}\Bigg(\int_\Omega G_m^{k|k-1}(\boldsymbol{r}_d,\boldsymbol{r};\omega)\Phi_x^{k|k-1}(\boldsymbol{r},\boldsymbol{r}_s;\omega)\frac{1-j\omega\tau(\boldsymbol{r})}{1+[\omega\tau(\boldsymbol{r})]^2}\gamma\delta a(\boldsymbol{r})d\boldsymbol{r} \\ & -\int_\Omega G_m^{k|k-1}(\boldsymbol{r}_d,\boldsymbol{r};\omega)\Phi_m^{k|k-1}(\boldsymbol{r},\boldsymbol{r}_s;\omega)\frac{1-j\omega\tau(\boldsymbol{r})}{1+[\omega\tau(\boldsymbol{r})]^2}\frac{\epsilon_m}{\epsilon_x}\delta a(\boldsymbol{r})d\boldsymbol{r} \\ & -\int_\Omega G_{mx}^{k|k-1}(\boldsymbol{r}_d,\boldsymbol{r};\omega)\Phi_x^{k|k-1}(\boldsymbol{r},\boldsymbol{r}_s;\omega)\frac{1-j\omega\tau(\boldsymbol{r})}{1+[\omega\tau(\boldsymbol{r})]^2}\delta a(\boldsymbol{r})d\boldsymbol{r}\Bigg) \qquad (4.36)\end{aligned}$$

where we define $\Phi_x^{k|k-1}(\boldsymbol{r},\boldsymbol{r}_s;\omega)$ as the solution of (4.8) and (4.12), $\Phi_m^{k|k-1}(\boldsymbol{r},\boldsymbol{r}_s;\omega)$ as the solution of (4.9) and (4.13), $G_m^{k|k-1}(\boldsymbol{r}_d,\boldsymbol{r};\omega)$ as the Green's function of (4.9) and (4.13), and $G_{mx}^{k|k-1}(\boldsymbol{r}_d,\boldsymbol{r};\omega)$ as the solution of (4.8) and (4.12) where $S(\boldsymbol{r},\omega)$ in (4.8) is replaced by $\gamma\mu_{axf}G_m^{k|k-1}(\boldsymbol{r}_d,\boldsymbol{r};\omega)$ given the EKF estimates of the fluorophore concentrations at different compartments at the $(k|k-1)^{th}$ step [27]. In (4.36), the first integral results from the right-hand side of (4.9), while the second and third integrals originate from the dependence of μ_{am} and μ_{ax}, respectively, on the unknown fluorophore absorption coefficient. We note that the kernels of the second and thirds integrals are much smaller than the kernel of the first integral. Therefore, the first integral in (4.36) dominates and the rest can be neglected. As a result, The first-order Fréchet derivative of $\boldsymbol{\mathcal{F}}$ (or $\mathcal{F}_{\boldsymbol{r}_d,\boldsymbol{r}_s}$) with respect to the fluorophore concentration a at the EKF total concentration estimate at the $(k|k-1)^{th}$ step can

be approximated by

$$\partial\mathcal{F}_{\boldsymbol{r}_d,\boldsymbol{r}_s}(\delta a) = \frac{\ln 10\gamma\epsilon_x}{\Phi_x^{k|k-1}(\boldsymbol{r}_d,\boldsymbol{r}_s;\omega)}\int_\Omega G_m^{k|k-1}(\boldsymbol{r}_d,\boldsymbol{r};\omega)\Phi_x^{k|k-1}(\boldsymbol{r},\boldsymbol{r}_s;\omega)\frac{1-j\omega\tau(\boldsymbol{r})}{1+[\omega\tau(\boldsymbol{r})]^2}\delta a(\boldsymbol{r})d\boldsymbol{r}, \tag{4.37}$$

Based on the assumptions *i*)-*iii*) in Section 4.3.1, the terms in the kernel of (4.37) can be computed as follows: Based on the assumption *i*), $\mu_{axe} \approx \mu_{ame}$. Furthermore, μ_{amf} and μ_{axf} are linearly dependent by (4.14). Thus, given the μ_{axe} reconstruction based on (4.8) and (4.12) at the k^{th} step, and μ_{amf} obtained via EKF estimates (fluorophore concentrations at different compartments and volume fractions) at the $(k|k-1)^{th}$ step, $G_m^{k|k-1}(\boldsymbol{r}_d,\boldsymbol{r};\omega)$ can be computed using (4.9) and (4.13). Similarly, given the μ_{axe} reconstruction based on (4.8) and (4.12) at the k^{th} step, and μ_{axf} estimate obtained via the EKF estimates of fluorophore concentrations at different compartments and volume fractions at the $(k|k-1)^{th}$ step, $\Phi_x^{k|k-1}(\boldsymbol{r}_d,\boldsymbol{r}_s;\omega)$ can be computed as the solution of (4.8) and (4.12). Finally, we assume that $\frac{1-j\omega\tau(\boldsymbol{r})}{1+[\omega\tau(\boldsymbol{r})]^2}$ is known.

Note that the calculation of the Fréchet derivative can be simplified under some additional assumptions. If μ_{axe} does not vary with the slow-time variable k, and that $\mu_{amf} \ll \mu_{ame}$, then $G_m(\boldsymbol{r}_d,\boldsymbol{r};\omega)$ can be computed with respect to μ_{axe} and remains invariant with respect to the slow-time variable k.

Using the chain rule, the first-order Fréchet derivative of $\mathcal{F}_{\boldsymbol{r}_d,\boldsymbol{r}_s}$ with respect to each element of $\boldsymbol{\mathcal{C}}$ is given by

$$\partial\mathcal{F}_{\boldsymbol{r}_d,\boldsymbol{r}_s}(\delta\mathcal{C}_i) = \frac{\ln 10\gamma\epsilon_x}{\Phi_x^{k|k-1}(\boldsymbol{r}_d,\boldsymbol{r}_s;\omega)}\int_\Omega G_m^{k|k-1}(\boldsymbol{r}_d,\boldsymbol{r};\omega)\Phi_x^{k|k-1}(\boldsymbol{r},\boldsymbol{r}_s;\omega)\frac{1-j\omega\tau(\boldsymbol{r})}{1+[\omega\tau(\boldsymbol{r})]^2}\delta\mathcal{C}_i v_i(\boldsymbol{r})d\boldsymbol{r}, \tag{4.38}$$

where $v_i, i = 1, 2, ..., n$, denotes the volume fractions.

Similarly, the first-order Fréchet derivative of $\mathcal{F}_{\boldsymbol{r}_d,\boldsymbol{r}_s}$ with respect to each element of $\boldsymbol{\alpha}_n$ is given by

$$\partial\mathcal{F}_{\boldsymbol{r}_d,\boldsymbol{r}_s}(\delta\boldsymbol{\alpha}_n) = \frac{\ln 10\gamma\epsilon_x}{\Phi_x^{k|k-1}(\boldsymbol{r}_d,\boldsymbol{r}_s;\omega)}\int_\Omega G_m^{k|k-1}(\boldsymbol{r}_d,\boldsymbol{r};\omega)\Phi_x^{k|k-1}(\boldsymbol{r},\boldsymbol{r}_s;\omega)\frac{1-j\omega\tau(\boldsymbol{r})}{1+[\omega\tau(\boldsymbol{r})]^2}\delta v_i(\boldsymbol{r})\mathcal{C}_i(\boldsymbol{r})dr. \tag{4.39}$$

Note that $\boldsymbol{\alpha}_n$ contains both pharmacokinetic-rate and volume fraction parameters.

However, the Fréchet derivative of $\boldsymbol{\mathcal{F}}$ with respect to pharmacokinetic-rates is zero since $\boldsymbol{\mathcal{F}}$ depends only on the volume fractions.

In our numerical simulations, we used finite elements with piece-wise linear first-order Lagrange polynomials to discretize the domain Ω and thus to discretize the Fréchet derivatives given in (4.38) and (4.39).

The EKF algorithms for the estimation of concentration and parameter images are different for the linear and non-linear measurement models given in (4.15) and (4.18). When the linearized measurement model (4.18) is employed, the operator $\boldsymbol{\mathcal{W}}$ is assumed to be constant throughout the dynamic update of the fluorophore concentration. This leads to the inherent assumption that the dynamic changes in the fluorophore concentration can be modeled as a perturbation on the endogenous chromophore concentrations. For the non-linear measurement model (4.15), on the other hand, the Fréchet derivative is updated at every iteration of the EKF algorithm based on the $(k|k-1)^{th}$ update of the concentration and volume fraction estimates. While computationally more intense, the EKF algorithm based on the non-linear measurement model eliminates the limiting assumption of restricting the dynamic changes to perturbations from a constant endogenous chromophore concentration.

4.4.3 Convergence and Initialization of EKF

In general, the convergence of EKF depends on proper choices of the initial values of $\boldsymbol{\theta}_n$ and $\mathbf{C}$, and proper selection of the noise covariance matrices $\mathbf{Z}$, $\mathbf{Q}$, and $\mathbf{R}$ [171]. The main cause of divergence in EKF is due to the fact that a change in the parameter vector, $\boldsymbol{\theta}_n$, has a direct effect on the Kalman gain; in other words, there is lack coupling term between the Kalman gain and the parameter vector [115, 172]. The covariance matrix $\mathbf{R}$ controls the convergence of the Kalman gain $\mathbf{G}_k$. To ensure stability, we set $\mathbf{R}$ much higher than the $\boldsymbol{\Lambda} P_{k|k-1} \boldsymbol{\Lambda}^T$ term in Table 4.1. However, setting very high values of $\mathbf{R}$ leads to slow convergence of the Kalman gain $\mathbf{H}_k$. It has been shown that if $\mathbf{Q}$, $\mathbf{Z}$ and $\mathbf{R}$ are selected less than the actual values, it leads to overconfidence in the accuracy of the estimates of the error covariance matrix [170]. Hence, we regard the initial values of these matrices (which are nothing but the multiples of identity matrix, i.e., $\sigma\mathbf{I}$) as tuning parameters.

Theoretically, the state estimates can be initialized at the expected value of the ICG concentrations, i.e. $E[\mathbf{C}(1)]$. One approach to the initialization of the parameters is to utilize the state-space presentation given in (4.23)-(4.25). Since $E(\mathbf{\Psi}(1)) = \epsilon \mathbf{W}\mathbf{V}_d(\boldsymbol{\theta}_n(1))E[\mathbf{C}(1)]$, $\mathbf{\Psi}(1) - \epsilon \mathbf{W}\mathbf{V}(\boldsymbol{\theta}_n(1))E[\mathbf{C}(1)]$ is a zero-mean random vector. If we express the variance of the measurement $\mathbf{\Psi}(1)$ in terms of the variance of $\mathbf{C}(1)$ using the measurement model in (4.25), and solve for $\boldsymbol{\theta}_n$, we get the estimate $\hat{\boldsymbol{\theta}}_n(1)$ as the most appropriate value for initialization. In depth discussion on the convergence properties of the EKF, and the initialization of parameters and covariance matrices can be found in [25, 115, 170–172, 191].

4.4.4 Computational Complexity of the EKF based Reconstruction Algorithms

In this subsection, we derive the computational complexity of the EKF based direct reconstruction algorithms based on the linear and non-linear models in (4.33) and (4.34) under the assumptions outlined in Sections 4.6.1 and 4.6.2. We next derive the computational complexity of the EKF based voxel-by-voxel pharmacokinetic-rate and concentration image reconstruction algorithm that we introduced in [179] and compare it with the computational complexity of the algorithms introduced in this chapter.

The computational complexity of one recursion of the EKF is $\mathcal{O}(2m^2h) + \mathcal{O}(2mh^2) + \mathcal{O}(m^3) + \mathcal{O}(h^3)$, where m denotes the dimension of the measurement vector, and h denotes the dimension of the states [30].

For the EKF based direct reconstruction algorithm based on the linear measurement model (4.34), the number of states h is $n(n+2)N$, where n is the number of compartments, and N is the number of voxels. Typical values of n, K, N, and m are tabulated in Table 4.2. Thus, assuming that $2m^2n(n+2) \sim N^2$, $2mn^2(n+2)^2 \sim N^{3/2}$, $m^3 \sim N^{5/2}$, and $n^3(n+2)^3 \sim N$, the computational complexity of direct reconstruction algorithm for one recursion of the EKF algorithm is given by $\mathcal{O}(N^3) + \mathcal{O}(N^3) + \mathcal{O}(N^2) + \mathcal{O}(N^4)$, which is dominated by the $\mathcal{O}(N^4)$ term. For the non-linear measurement model (4.33), the Fréchet derivative of $\boldsymbol{\mathcal{F}}$ has to be computed at every recursion, which has a computational complexity of

$\mathcal{O}(N_d N^2 + N_s N^2)$ [166]. Assuming that N_d and $N_s \ll N^2$, the computational complexity of every recursion of the EKF algorithm using the non-linear measurement model is $\mathcal{O}(N^4)$. Hence, the EKF based direct reconstruction algorithms using either the non-linear or linear measurement model have the computational complexity of $\mathcal{O}(N^4)$.

Table 4.2: Possible range of values of the parameters used for complexity analysis

Number of compartments, n	$2-4$
Total number of voxels, N	$576-649$
Size of measurement vector, m	$128-256$
Total number of steps, K	$50-100$

For the EKF based voxel-by-voxel construction algorithm that we introduced in [179], the number of states, h, is $n(n+2)$ and $m = 1$. In this algorithm, the absorption coefficient images are reconstructed prior to pharmacokinetic-rate images. In general, the computational complexity of this step is $\mathcal{O}(N^3 K)$ for a linear reconstruction algorithm, where K is the number of slow-time steps. Assuming that, $2n(n+2) \sim N^{1/2}$, $2n^2(n+2)^2 \sim N$, and $n^3(n+2)^3 \sim N^{3/2}$, the computational complexity of the voxel-by-voxel reconstruction algorithm for one recursion of the EKF is given by $\mathcal{O}(N^3 K) + \mathcal{O}(N^{3/2}) + \mathcal{O}(N^2) + \mathcal{O}(N) + \mathcal{O}(N^{5/2})$, which is dominated by the $\mathcal{O}(N^3 K)$ term. For the non-linear measurement model, the computational complexity of reconstructing the absorption images of fluorophore is $\mathcal{O}(N^3 K p)$ where p is the number of iterations performed in Born-type non-linear iterative reconstruction schemes. Clearly, if the number of slow-time samples multiplied with the iteration number, Kp, is of higher order than the total number of voxels, N, then, the computational complexity of the direct reconstruction algorithm is smaller than that of the voxel-by-voxel algorithm. However, for the current dynamic imaging systems, Kp, is smaller than N.

For the direct reconstruction framework, the algorithm stores three covariance matrices $\mathbf{Q}$, $\mathbf{R}$, and $\mathbf{Z}$ each has size $nN \times nN$, $m \times m$, and $n(n+1)N \times n(n+1)N$, respectively. For each iteration, the algorithm stores measurement matrix of size $m \times 1$, stores and updates the error covariance matrix, $\mathbf{P}$, of size $n(n+2)N \times n(n+2)N$, the Kalman gain, $\mathbf{H}$, of size $n(n+2)N \times m$, the matrices of size $\mathbf{\Lambda}$ and $\mathbf{J}$,

$m \times n(n+2)N$, and $n(n+2)N \times n(n+2)N$, respectively. The algorithm also stores all the updates of the concentrations and parameters of size $n(n+2)N \times 1$.

4.5 Numerical Simulations and Pharmacokinetic-rate Image Reconstruction from *in vivo* Breast Data

We tested the performance of our approach using simulated data, and *in vivo* data acquired from three patients with breast tumor. We first present the numerical simulations and compare the performance of direct reconstruction algorithm (for both the linear and non-linear measurement models) with that of voxel-by-voxel reconstruction algorithm presented in [179]. Next, we present the pharmacokinetic-rate images reconstructed from *in vivo* breast data.

4.5.1 Numerical Simulations

We performed a simulation study using the two-compartment model for ICG pharmacokinetics described in Section 4.2.2 and the light propagation model described in Section 4.3.1. Using physiologically relevant values for the pharmacokinetic rates, k_{in}, k_{out}, k_{elm}, and volume fractions, v_e, v_p, given in Table 4.3, we simulated the boundary measurements, $\mathbf{\Psi}(k)$, $k = 1, \ldots, K$, for a tissue-like 2-D phantom. The maximum transition rates of k_{in} and k_{out} are simulated at the center of the image and smoothly decreased towards the boundaries based on the results given in [95, 179]. The fluorescence quantum efficiency and lifetime of ICG are assumed to be constant and set to 0.016 and 0.56 ns, respectively. The modulation frequency was set to 300 MHz. The physical dimension of the 2-D phantom was chosen 6 cm by 6 cm. The image domain was discretized into 24 by 24 pixels each of size 0.25cm by 0.25 cm. As a prior model, we employed a four-pixel neighborhood model $\beta = 1/4$ due to rectangular nature of the geometry. 24 sources and 24 detectors along the boundary of the phantom were used to generate simulated data as shown in Figure 4.3. The values of k_{elm}, v_e and v_p in Table 4.3 correspond to the average values of the heterogeneities from the 24 by 24 pixel phantom images.

We tested the EKF based direct reconstruction algorithm based on both the non-linear (4.33) and linear (4.34) measurement models. In the linear model, we

Table 4.3: Physiological values for numerical simulations

Maximum value of k_{in}	0.037 sec^{-1}
Maximum value of k_{out}	0.029 sec^{-1}
k_{elm}	0.0054 sec^{-1}
v_e	0.3
v_p	0.04
μ_{axe}	0.05 cm^{-1}
$\mu_{sx}^{`}$	8 cm^{-1}

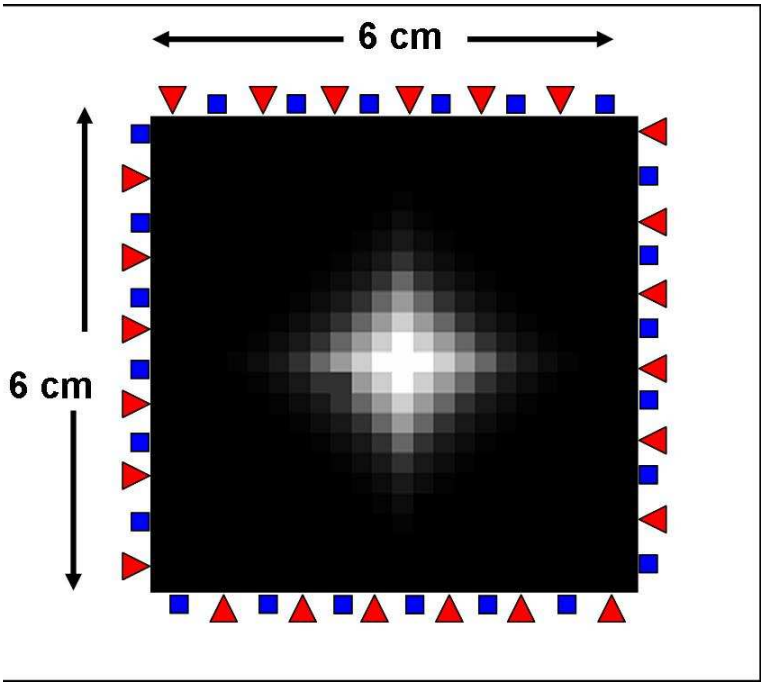

Figure 4.3: The source detector configuration for the numerical phantom. Rectangular shapes present the detectors and the triangular ones present the sources.

computed the matrix $\mathbf{W}$ based on the background $\mu_{ax,m}$, and assumed that it is constant throughout the dynamic update of the fluorophore concentrations. For the non-linear model, we updated the Fréchet derivative of $\mathbf{F}$, at every iteration of the EKF algorithm based on the $(k|k-1)^{th}$ update of the concentration and volume fraction estimates as defined in (4.37)-(4.39). In the update of the Fréchet derivatives, we assumed that μ_{axe} is constant, and $\mu_{ame} \gg \mu_{amf}$. As a result, we

computed $G_m(\boldsymbol{r}_d, \boldsymbol{r}; \omega)$ once, and did not update at every recursion, but updated the $\Phi_x^{k|k-1}(\boldsymbol{r}, \boldsymbol{r}_s; \omega)$ at every recursion as described in Section 4.5.1. We chose the initial values of concentrations, pharmacokinetic-rates and volume fractions that lead to minimum norm of error covariance matrix within biological limits.

Figures 4.5a and Fig. 4.6a show the phantom images of the pharmacokinetic-rates k_{in} and k_{out}. Fig. 4.5b and Fig. 4.6b display the corresponding k_{in} and k_{out} images reconstructed by the EKF based direct reconstruction algorithm with the non-linear measurement model. Fig. 4.5c and Fig. 4.6c display the corresponding k_{in} and k_{out} images obtained by the direct reconstruction with the linear measurement model. Figures 4.5d and 4.6d display the corresponding k_{in} and k_{out} images using the voxel-by-voxel algorithm introduced in [179]. We observe that there is a good agreement between the true and the estimated images in terms of localization of the heterogeneities. In all three reconstruction algorithms, the center of the heterogeneity is consistent with the ones in the original phantom images. Visual inspection of reconstructed images shows that the EKF based direct reconstruction algorithm leads to smoother and less noisy images than that of the voxel-by-voxel reconstruction.

To quantify the difference between the reconstructed and true images, we used the normalized mean square error (NMSE):

$$\text{NMSE} = 20\log_{10}\frac{||X_{recon} - X_{true}||^2}{||X_{true}||^2}.$$

Note that NMSE $= -$SNR where SNR stands for signal-to-noise-ratio. Table 4.4 tabulates the NMSE values for k_{in} and k_{out} images for three different reconstruction methods. For the direct reconstruction algorithm with the non-linear measurement model, the NMSE for k_{in} and k_{out} images are -19.77 dB and -18.49 dB, respectively. For the direct reconstruction algorithm with the linear measurement model, the NMSE for k_{in} and k_{out} images are -18.45 dB and -17.65 dB, respectively. Finally, for the voxel-by-voxel construction algorithm, the error for k_{in} and k_{out} images are -16.88 dB and -15.90 dB, respectively.

Next, we studied the effect of measurement noise in the performance of the direct reconstruction algorithm and compared it with that of the voxel-by-voxel al-

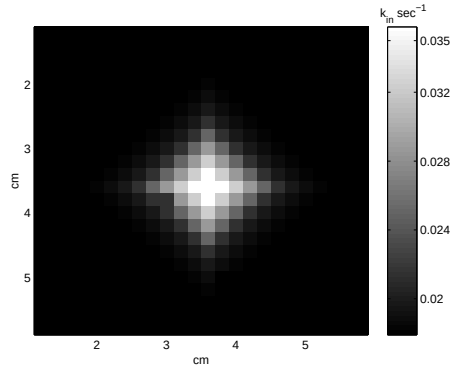

(a) Original phantom image

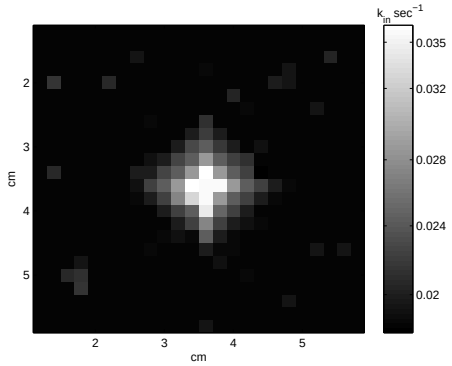

(b) EKF based direct reconstruction using the non-linear measurement model.

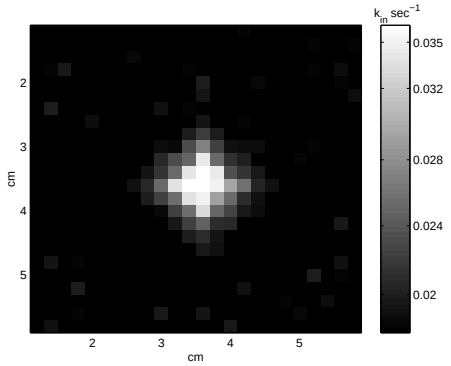

(c) EKF based direct reconstruction using the linear measurement model.

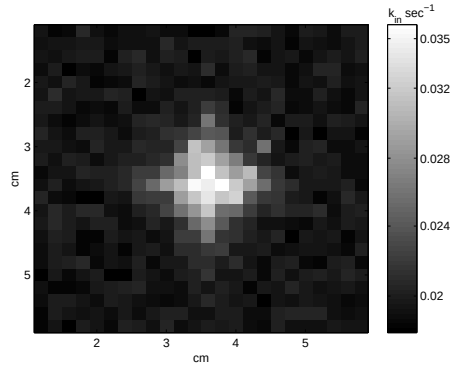

(d) EKF based voxel-by-voxel reconstruction.

Figure 4.4: Pharmacokinetic-rate images of k_{in} for three different reconstruction algorithms.

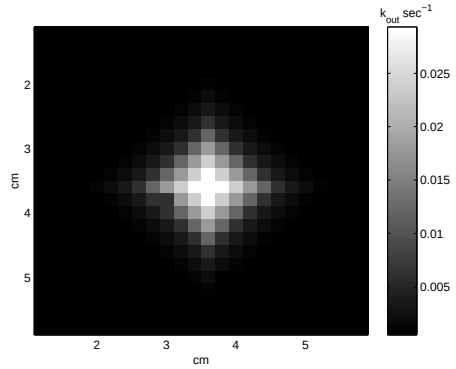

(a) Original phantom image

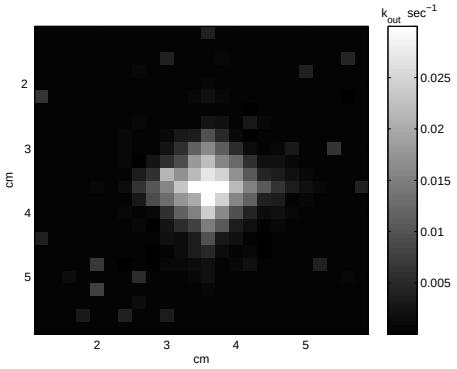

(b) EKF based direct reconstruction using the non-linear measurement model.

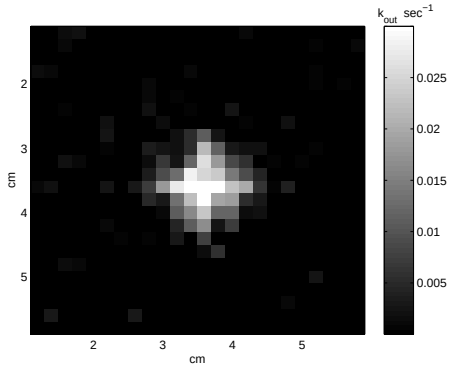

(c) EKF based direct reconstruction using the linear measurement model.

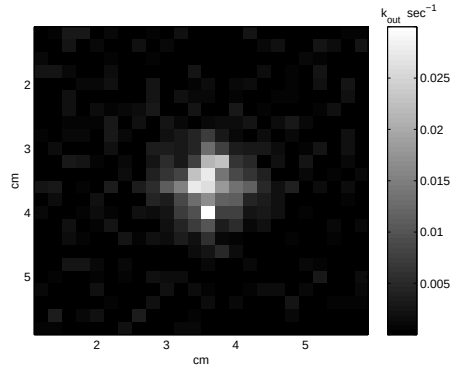

(d) EKF based voxel-by-voxel reconstruction.

Figure 4.5: Pharmacokinetic-rate images of k_{out} for three different reconstruction algorithms.

Table 4.4: NMSE values for k_{in} and k_{out} images for three different reconstruction methods

	k_{in} NMSE (dB)	k_{out} NMSE (dB)
Direct Reconstruction (Non-linear)	**-19.77**	**-18.49**
Direct Reconstruction (Linear)	**-18.45**	**-17.65**
Voxel-by-voxel Reconstruction	**-16.88**	**-15.90**

gorithm. We added zero-mean white Gaussian noise with standard deviation equal to 5% to 15% of the average of the measurements with a step size of 2.5%. We generated 15 realizations of the Gaussian noise at each level and determined NMSE based on 15 reconstructions. Fig. 4.6(a) and (b) show the NMSE versus the measurement noise for 5 different noise levels for k_{in} and k_{out} images, respectively. Clearly, the NMSE in the reconstructed k_{in} and k_{out} images increases as the measurement noise increases. The pharmacokinetic-rate images obtained with the direct reconstruction algorithm (both linear and non-linear cases) together with the *a prior* information results in smaller error values as compared to the voxel-by-voxel reconstruction algorithm. Moreover, the direct reconstruction algorithm using the non-linear measurement model resulted in smaller error values as compared to the direct reconstruction algorithm with the linear measurement model.

In general, the improvements in the direct reconstructed images can be attributed to; (*i*) the use of spatio-temporal prior model for the pharmacokinetic-rate images which leads to more robust algorithms and smoother images; (*ii*) efficient use of the inherent temporal correlations in NIR measurements by combining spatial (photon propagation) and temporal (compartmental) models.

We also studied, the effect of initialization of the covariance matrices $\mathbf{R}$, $\mathbf{Q}$, and $\mathbf{Z}$ in the reconstructed pharmacokinetic-rate images. We chose the initial values of concentrations, pharmacokinetic-rates, volume fractions and $\mathbf{R}$, $\mathbf{Q}$ and $\mathbf{Z}$ matrices that lead to minimum norm of error covariance matrix within biological limits. Let $\mathbf{R} = \alpha_1\mathbf{I}$, $\mathbf{Q} = \alpha_2\mathbf{I}$, and $\mathbf{Z} = \alpha_3\mathbf{I}$, where $\mathbf{I}$ is an identity matrix, and $\boldsymbol{\alpha} = [\alpha_1 \;\; \alpha_2 \;\; \alpha_3]$. Table 4.5 presents the NMSE values for k_{in} and k_{out} for different values of $\boldsymbol{\alpha}$ using both linear and non-linear direct reconstruction algorithms. The optimal

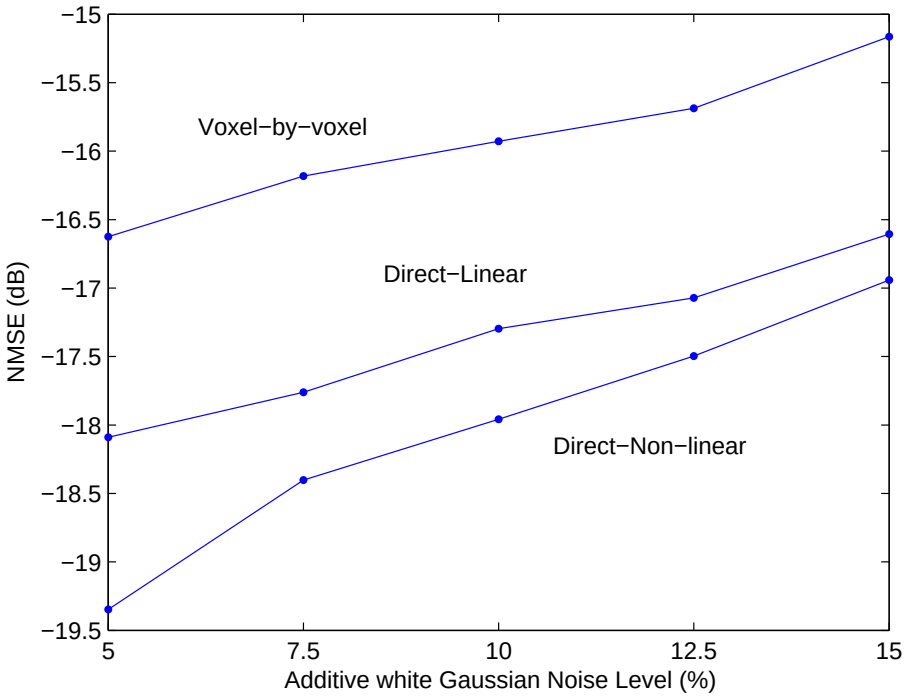

(a)

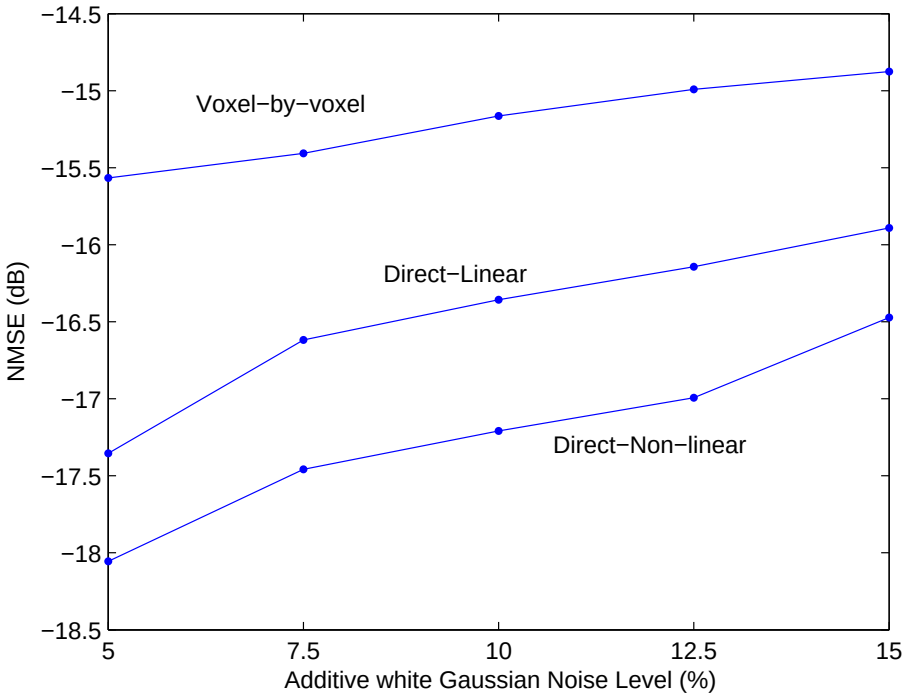

(b)

Figure 4.6: NMSE vs measurement noise levels for the direct and voxel-by-voxel reconstruction algorithms (a) k_{in} images, (b) k_{out} images.

$\boldsymbol{\alpha}$ is [0.012 0.051 0.0025]. We observed that optimal $\boldsymbol{\alpha}$ results in visually better quality images than that of other $\boldsymbol{\alpha}$ values.

Table 4.5: NMSE values for k_{in} and k_{out} images for different initial values of covariance matrices, $\boldsymbol{\alpha}$ = [0.012 0.051 0.0025]

	LINEAR		NON-LINEAR	
	k_{in} NMSE (dB)	k_{out} NMSE (dB)	k_{in} NMSE (dB)	k_{out} NMSE(dB)
$\boldsymbol{\alpha}/10$	-7.51	-7.21	-8.35	-7.66
$\boldsymbol{\alpha}/5$	-10.57	-10.14	-11.60	-10.54
$\boldsymbol{\alpha}/2$	-12.99	-12.36	-14.66	-13.23
$\boldsymbol{\alpha}$	**-18.07**	**-17.38**	**-19.47**	**-18.14**
$2\boldsymbol{\alpha}$	-12.07	-11.46	-12.84	-12.21
$3\boldsymbol{\alpha}$	-8.29	-7.70	-8.77	-9.19

We also include the reconstructed images for $\boldsymbol{\alpha}/2$. Figures 4.7 and 4.8 represents the reconstructed pharmacokinetic-rate images of k_{in} and k_{out} for $\boldsymbol{\alpha}$ and $\boldsymbol{\alpha}/2$. From Figures 4.7 and 4.8, we can see that the decrease in NMSE value effects the visual quality of the reconstructed pharmacokinetic-rate images.

4.5.2 Pharmacokinetic-rate Images from in vivo Breast Data

We used *in vivo* breast data acquired by a continuous wave (CW) NIR imaging apparatus to reconstruct the pharmacokinetic-rate images of ICG. The apparatus has 16 light sources and 16 detectors located on a circular holder at an equal distance from each other with 22.5 degrees apart. Sources and detectors were collocated and were in the same plane. The breast was arranged in a pendular geometry with the source-detector probes gently touching its surface. A set of measurement for each source was collected at every 500 ms. The total time for the whole scan of the breast including 16 sources and 16 detectors was 8.8 seconds. The detectors used the same positions as the sources to collect the light originating from one source at a time. Only the measurements from the farthest 11 detectors with high SNR were used in image reconstruction (115 measurements out of 256 measurements for each time instant). ICG was injected intravenously by bolus with a concentration of 0.25 mg

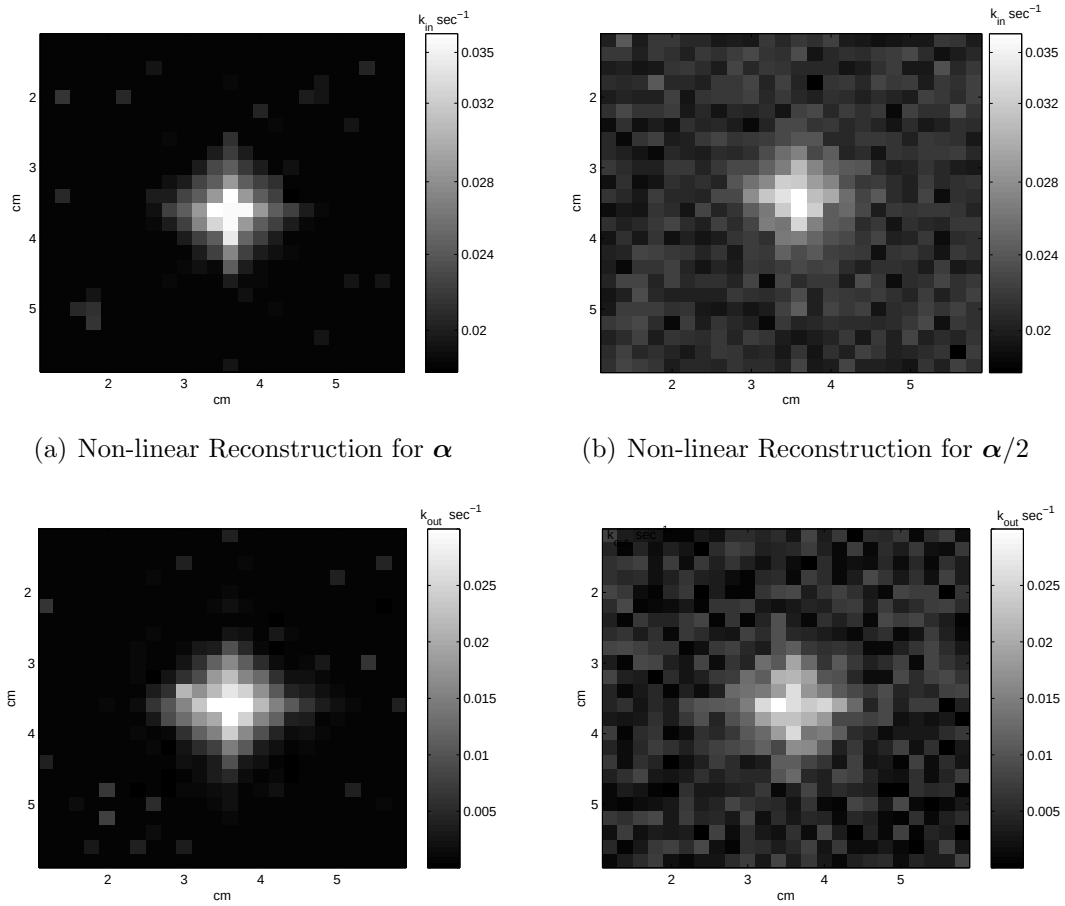

(a) Non-linear Reconstruction for $\boldsymbol{\alpha}$

(b) Non-linear Reconstruction for $\boldsymbol{\alpha}/2$

(c) Non-linear Reconstruction for $\boldsymbol{\alpha}$

(d) Non-linear Reconstruction for $\boldsymbol{\alpha}/2$

Figure 4.7: Non-linear Reconstruction: Pharmacokinetic-rate images of k_{in} and k_{out} for $\boldsymbol{\alpha}$ and $\boldsymbol{\alpha}/2$.

per kg of body weight. Data acquisition started before the injection of ICG and continued for 10 minutes.

Three patients with different tumor types were included in the study. First case, Case 1, is a fibroadenoma, which corresponds to a mass estimated to be $1-2$ cm in diameter, and located 1 cm below the skin. Second case, Case 2, is an adenocarcinoma corresponding to a tumor estimated to be $2-3$ cm in diameter, and located approximately 2 cm below the skin. Third case, Case 3, is an invasive ductal carcinoma, which corresponds to a mass estimated to be $3-4$ cm in diameter, and located 2 cm below the skin. Diagnostic information was obtained by biopsy after data acquisition. A more detailed explanation of the apparatus, the data collection

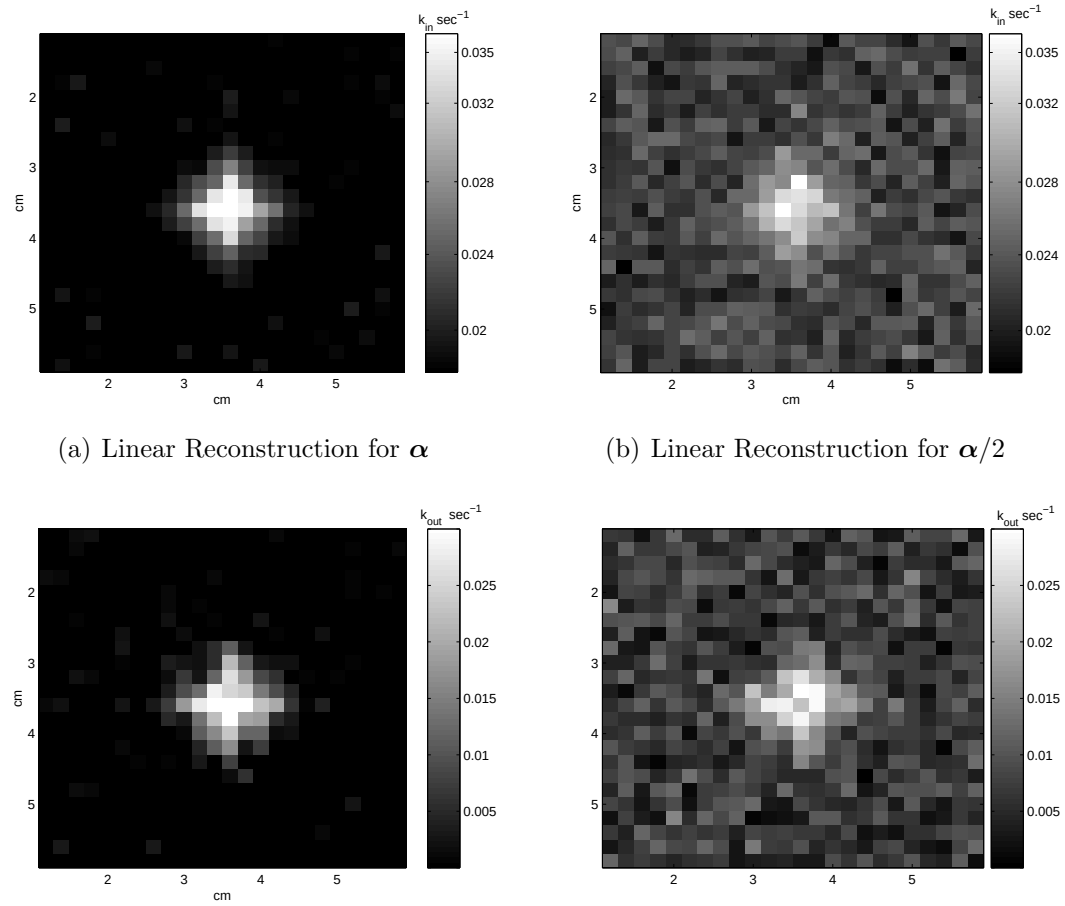

(a) Linear Reconstruction for $\boldsymbol{\alpha}$

(b) Linear Reconstruction for $\boldsymbol{\alpha}/2$

(c) Linear Reconstruction for $\boldsymbol{\alpha}$

(d) Linear Reconstruction for $\boldsymbol{\alpha}/2$

Figure 4.8: Linear Reconstruction: Pharmacokinetic-rate images of k_{in} and k_{out} for $\boldsymbol{\alpha}$ and $\boldsymbol{\alpha}/2$.

protocol and tumor information can be found in [97].

We used a two-compartment model for the ICG pharmacokinetics as described in (4.5), (4.6) and (4.7). We combined the two-compartment model with the linear measurement model (4.18). We made the following simplifying assumptions: The diffusion coefficient D_x is constant and is equal to 0.0416 cm. The endogenous absorption coefficient at the excitation and emission wavelength are approximately the same, $\mu_{ame} \approx \mu_{axe}$. Thus, we determined G_m^e and ϕ_x^e based on (4.9) using the excitation measurements prior to ICG injection. We next set the left hand side of (4.18) to excitation measurements after the ICG injection and reconstructed two-dimensional ICG pharmacokinetic-rate and concentration images based on (4.32)

and (4.34). The resulting measurement model is known as the differential diffuse optical tomography model. A more detailed description of the model can be found in [97,179,189]. As a prior model, we employed a six-pixel neighborhood model $\beta = 1/6$ due to circular nature of the geometry. The initial values for the pharmacokinetic-rates and covariance matrices were regarded as tuning parameters and the values that lead to minimum norm error covariance matrix were chosen as initial values.

The resulting ICG pharmacokinetic-rate images are shown in Fig. 4.9, 4.10 and 4.11. The images show that there is a good agreement with the location of the heterogeneity in the images and the physical location of the tumors. Our results show that the pharmacokinetic-rates are higher around the tumor region agreeing with the fact that permeability increases around the tumor region due to compromised capillaries of tumor vessels [60, 61]. Additionally, we reconstructed the ICG concentration images for plasma and the EES compartments. Figures 4.11-4.16 show the ICG concentration in plasma and the EES for 3 different time instants for Case 1, 2, and 3, respectively. We observed that ICG concentrations in plasma and the EES compartments are higher around the tumors agreeing with the hypothesis that around the tumor region ICG may act as a diffusible extravascular flow in leaky capillary of tumor vessels. Although the number of available patient data is limited, our results indicate that the pharmacokinetic-rate imaging may provide new approaches to evaluate and improve breast cancer diagnosis and staging. Such approaches may include extraction of new quantitative features from ICG pharmacokinetic-rate images, and statistical analysis of spatial distribution of pharmacokinetic-rates.

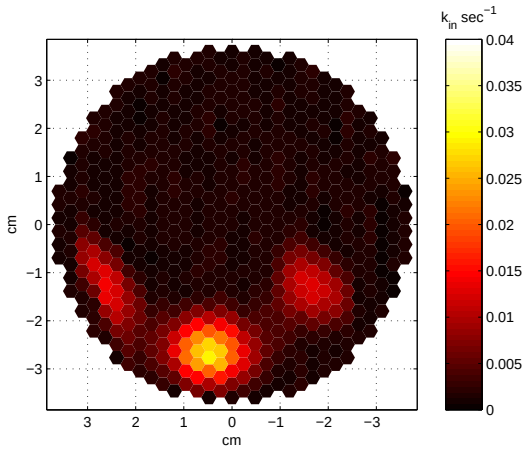

(a)

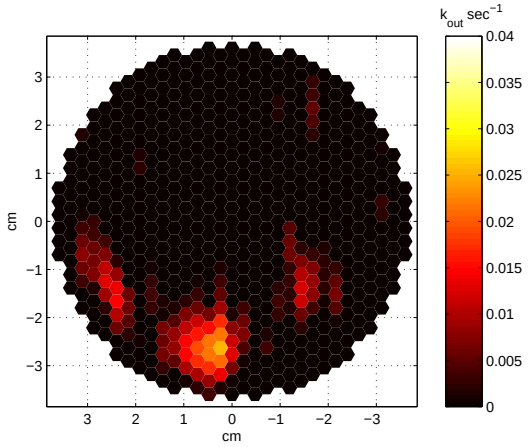

(b)

Figure 4.9: Case 1: Direct reconstructed pharmacokinetic-rate images of (a) k_{in}, (b) k_{out}.

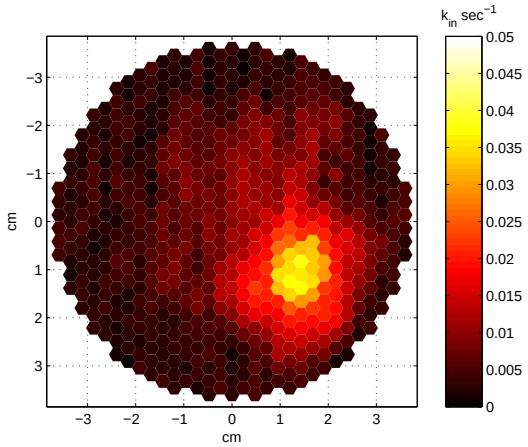

(a)

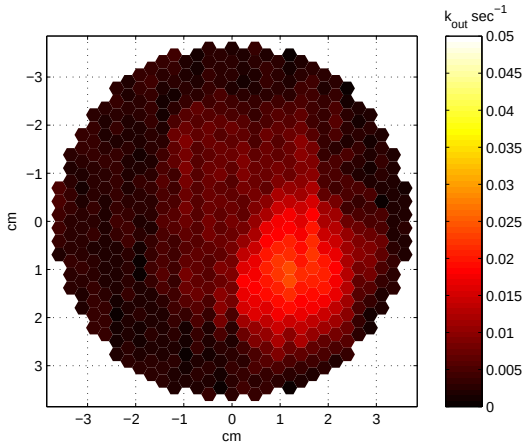

(b)

Figure 4.10: Case 2: Direct reconstructed pharmacokinetic-rate images of (a) k_{in}, (b) k_{out}.

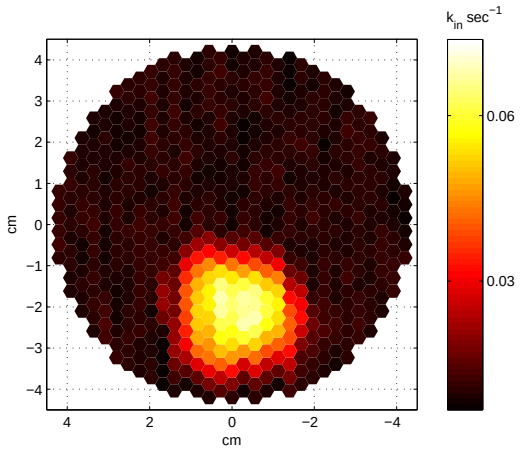

(a)

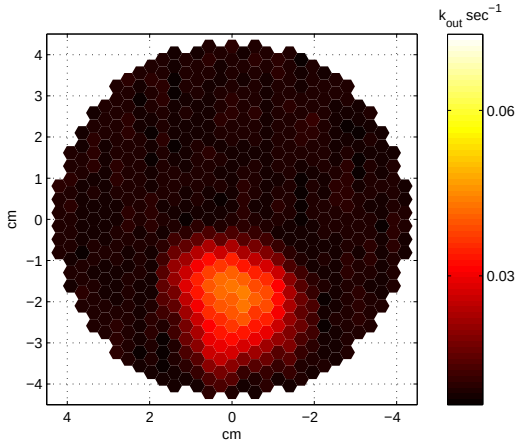

(b)

Figure 4.11: Case 3: Direct reconstructed pharmacokinetic-rate images of (a) k_{in}, (b) k_{out}.

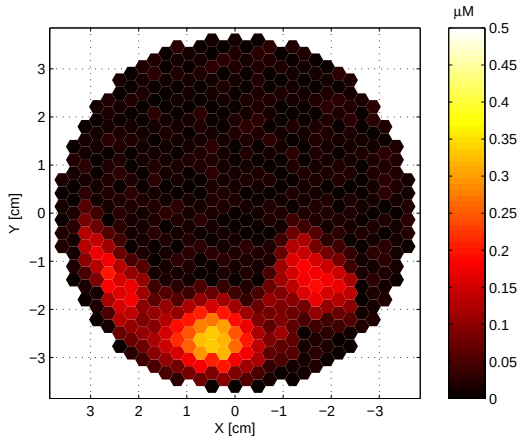

(a)

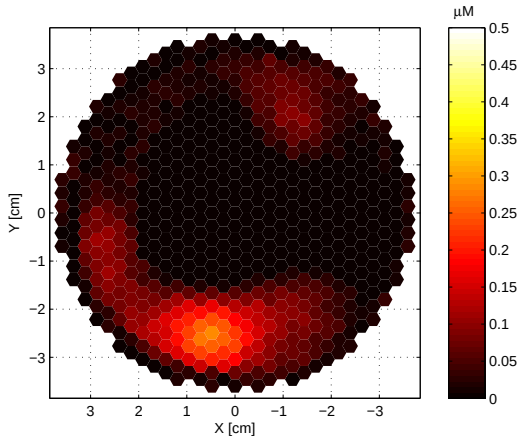

(b)

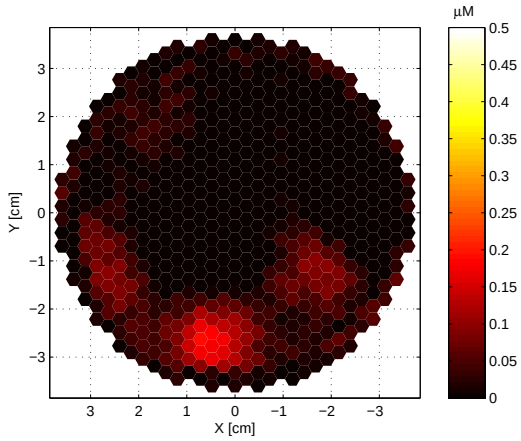

(c)

Figure 4.12: Direct reconstructed ICG concentration images in plasma for Case 1 for (a) 246.4^{th}, (b) 334.4^{th}, and (c) 422.4^{th} seconds.

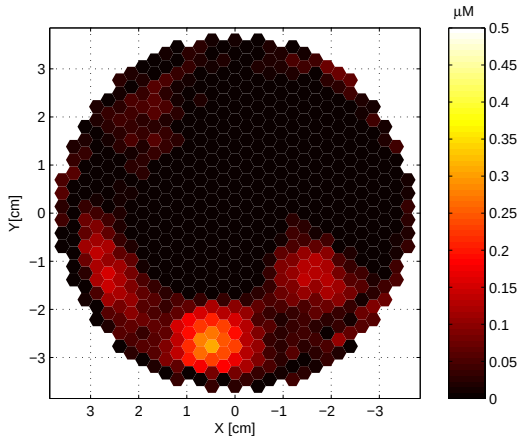

(a)

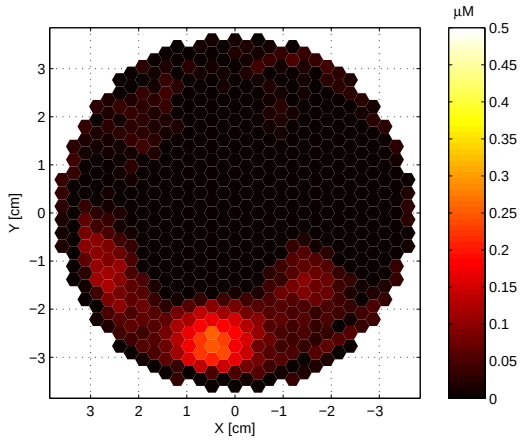

(b)

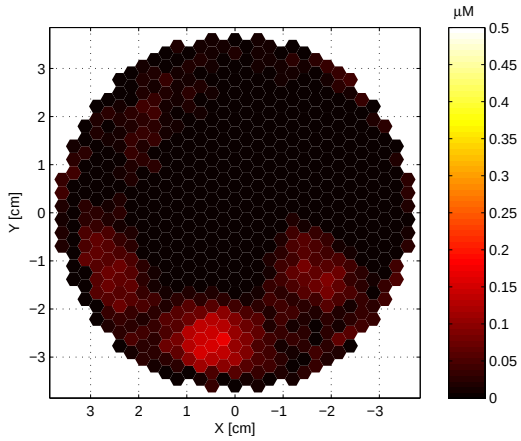

(c)

Figure 4.13: Direct reconstructed ICG concentration images in the EES for Case 1 for (a) 246.4^{th}, (b) 334.4^{th}, and (c) 422.4^{th} seconds.

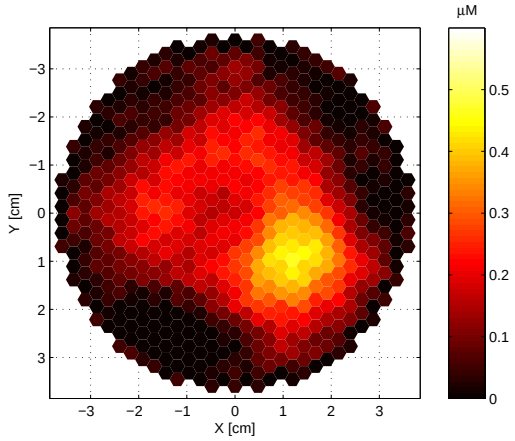

(a)

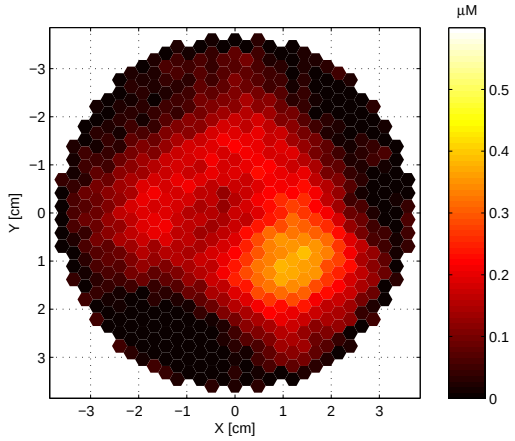

(b)

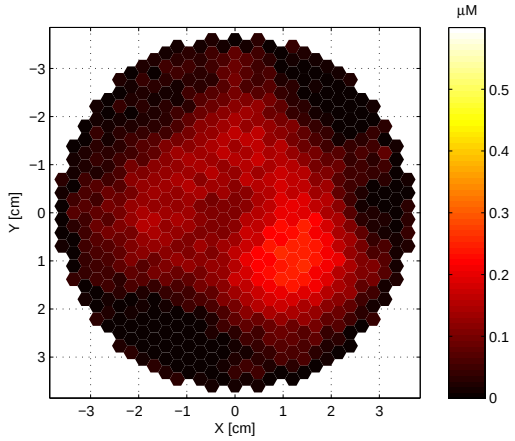

(c)

Figure 4.14: Direct reconstructed ICG concentration images in plasma for Case 2 for (a) 228.8^{th}, (b) 316.8^{th}, and (c) 404.8^{th} seconds.

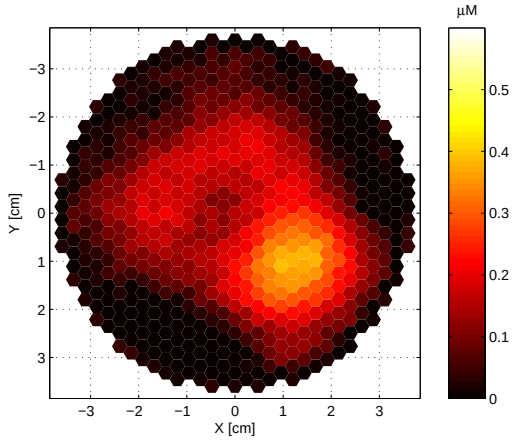

(a)

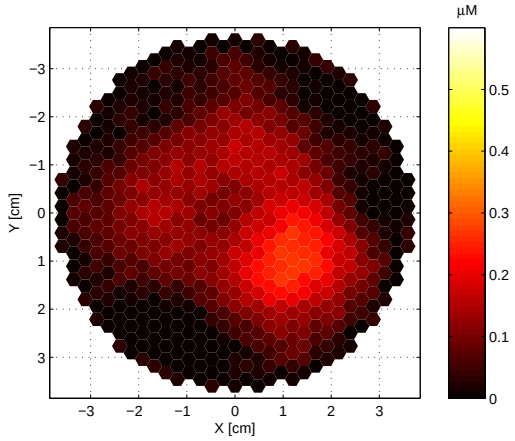

(b)

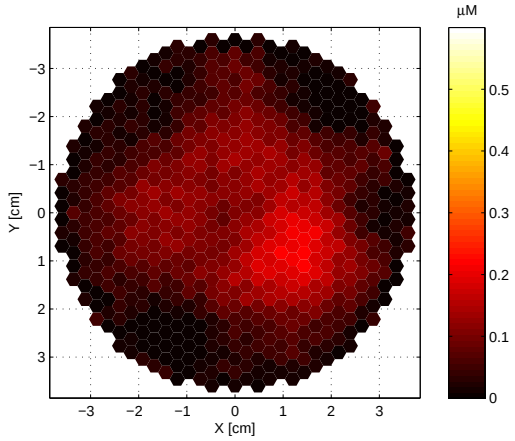

(c)

Figure 4.15: Direct reconstructed ICG concentration images in the EES for Case 2 for (a) 228.8^{th}, (b) 316.8^{th}, and (c) 404.8^{th} seconds.

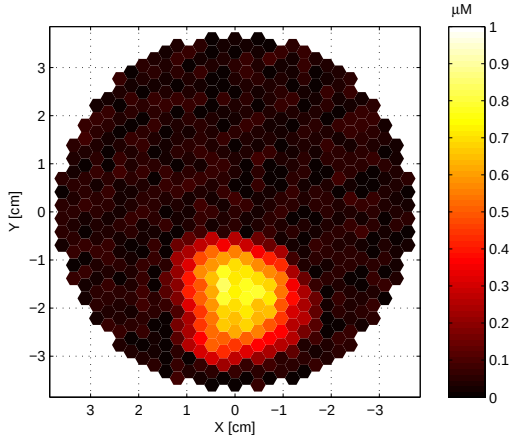

(a)

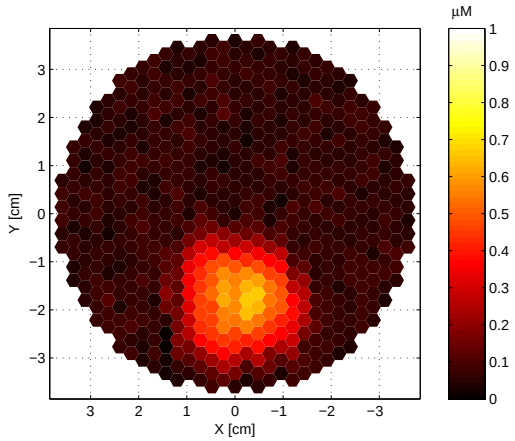

(b)

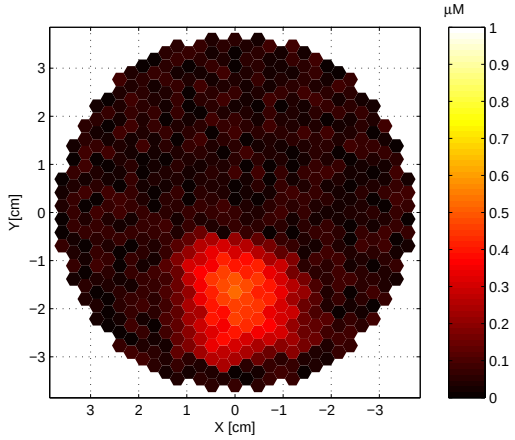

(c)

Figure 4.16: Direct reconstructed ICG concentration images in the plasma for Case 3 for (a) 246.4^{th}, (b) 378.4^{th}, and (c) 510.4^{th} seconds.

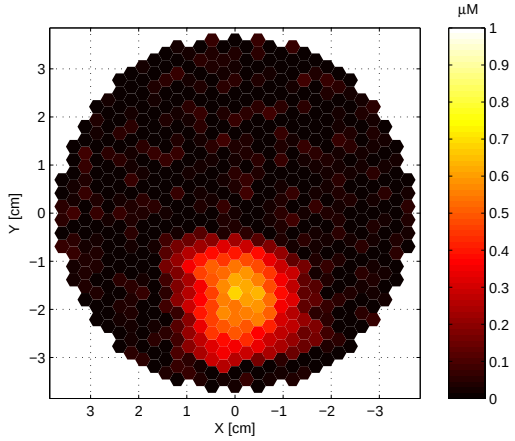

(a)

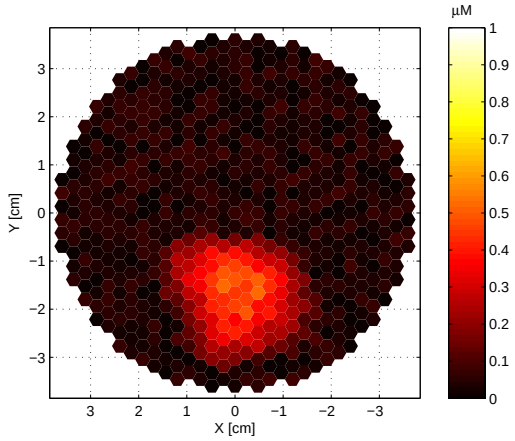

(b)

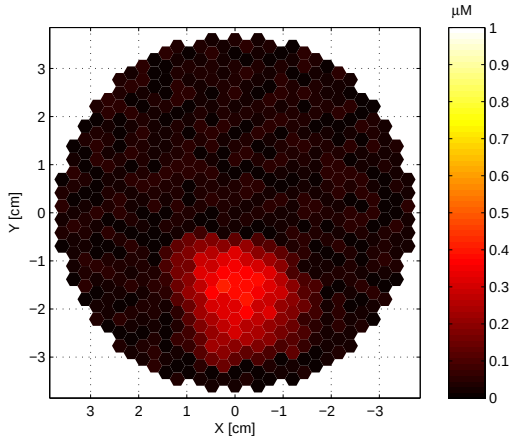

(c)

Figure 4.17: Direct reconstructed ICG concentration images in the EES for Case 3 for (a) 246.4^{th}, (b) 378.4^{th}, and (c) 510.4^{th} seconds.

CHAPTER 5
Evaluation of NIR Optical Features for Breast Cancer Diagnosis using *in vivo* Patient Data

In this work, we evaluated the diagnostic capability of optical features extracted from *in vivo* near-infrared spectroscopy data. Our evaluation criteria is based on statistical classification techniques, and receiver operating characteristics (ROC) methodology. Three features, namely, relative blood volume concentration, ΔBV, oxygenation desaturation, $\Delta Deoxy$, and the size of the tumor, S, were used to characterize benign and malignant tumors. The performance of the proposed set of features were evaluated using nearest mean, neural network, support vector, Parzen, and normal density based classifiers on 44 patients with malignant tumors, and 72 patients with benign tumors. The area under the ROC curve of the scaled nearest mean classifier using the three features yields the best value of 0.91.

The rest of the chapter is organized as follows: In Section 5.2, we present the NIR apparatus, and data collection protocol and optical features. In Section 5.3 we present feature analysis and tumor classification. In Section 5.4, we present statistical analysis of the data.

5.1 Materials and Methods

5.1.1 Apparatus

In this study, a continuous wave (CW) near infra red spectrometer (NIRS) is used (Figure 5.1) [231]. In the center of the probe there is a 3-wavelength LED. The LED intensity is low, 10-15 mA. The probe consisted of one multi-wavelength LED as a light source and 8 silicon diodes as detectors (Figure 5.2). These 8 detectors surround the LED at 4 cm distance, so that 8 locations over a 9 cm diameter area from a breast can be measured. The light sources are flashed alternately 100 times per second and electronic circuits are designed to amplify and time separate the signals in a sample and hold circuit which integrates the signals over an interval of a few seconds sufficiently rapidly to follow the movements of the sensor over the

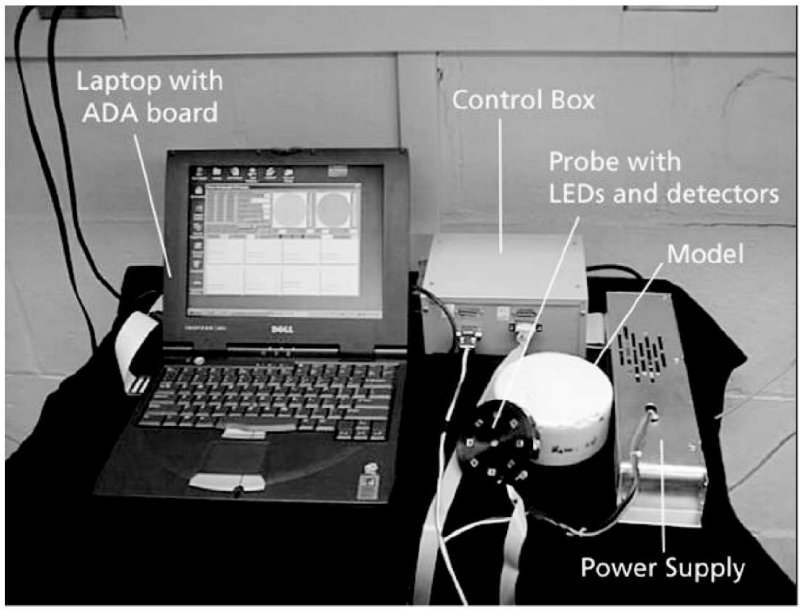

Figure 5.1: A photograph of the whole apparatus illustrates the handheld puck or probe, the coupling to the circuit box which contains the drivers for the LED, the amplifiers for the OPTI-101s, the digitally controlled gain adjustment amplifier, the electronic switch which decodes the light pulses and stores the information in a memory capacitor, the second set of switches which sample the memory capacitor at a rate compatible with the computer ADC, the software for computing blood concentration and blood saturation and the display on the computer which serves to normalize the signals through the digitally controlled amplifier.

breast, allowing usually 10 seconds for any particular sensor position. The data are then digitized and presented as a running time display so that the operator can be sure that stable readings are reached at each position of the sensor. The light intensity from the 8 detectors were adjusted to be near 1 volt by gains set and calibrated with a phantom with known absorption and scattering coefficients (μ_a = 0.04 to 0.07 and $\mu_s' = 8\ cm^{-1}$).

5.1.2 Patients and Protocol

The *in vivo* data was collected at two centers, the Abramson Family Cancer Research Institute, Department of Radiology of the Hospital of University of Penn-

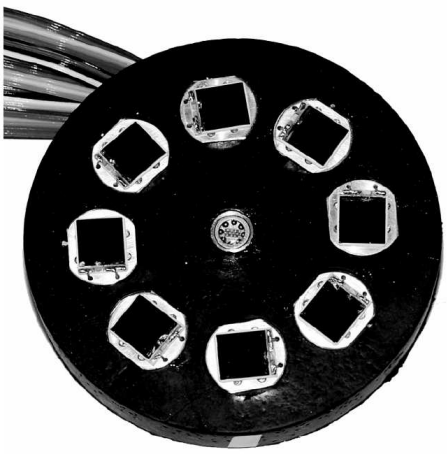

Figure 5.2: The NIR probe with a multi-wavelength LED and 8 silicon diodes as detectors.

sylvania (HUP), and the Department of Gynecology of Leipzig University (DGLU). HUP provided 24 patients with malignant and 64 patients with benign tumors. DGLU provided 20 patients with malignant and 8 patients with benign tumors.

The measurements were taken on the tumor-free contralateral breast to include the mirror image location of the suspected tumor. The probe was then transferred to the breast with suspected tumor. The detectors giving the largest changes with respect to the contralateral breast were assumed to be related to tumor and used for diagnosis. The procedure requires less than 10 minutes.

5.1.3 Optical Features

In this study, three features, namely, relative blood volume concentration, ΔBV, oxygenation desaturation, $\Delta Deoxy$, and the size of the tumor, S, are used.

ΔBV, and $\Delta Deoxy$ values are obtained based on a lipid blood oxygen model [231]. Thus, the change in BV and $Deoxy$ are relative to the contralateral breast:

$$\Delta BV = \Delta BV_{tumor} - \Delta BV_{contra} \tag{5.1}$$

$$\Delta Deoxy = \Delta Deoxy_{tumor} - \Delta Deoxy_{contra} \tag{5.2}$$

where ΔBV_{tumor}, ΔBV_{contra} are relative blood volume concentration in the tu-

mor breast with respect to the contralateral breast, respectively, and $\Delta Deoxy_{tumor}$, $\Delta Deoxy_{contra}$ are relative oxygenation desaturation in the tumor breast with respect to the contralateral breast, respectively.

The relative blood volume concentration, ΔBV, and the oxygenation desaturation, $\Delta Deoxy$, can be approximated at two different wavelengths by

$$\Delta BV \propto \gamma \Delta OD_{730} + \Delta OD_{850} \tag{5.3}$$

$$\Delta Deoxy \propto \beta \Delta OD_{730} + \Delta OD_{850} \tag{5.4}$$

where ΔOD_{730}, and ΔOD_{850} denote the relative changes in optical density at 730 nm and 850 nm, respectively, $\gamma = 0.3$, and $\beta = 1.3$ are the matching constants, and ΔOD is the differential optical density given by

$$\Delta OD = log \frac{I_0}{I} \tag{5.5}$$

where I is light intensity after absorption and scattering, and I_0 is the baseline light intensity obtained from the contralateral breast.

To demonstrate the utility of equations (5.3) and (5.4), and obtain the matching constants, ΔBV and $\Delta Deoxy$ were calculated using:

$$\Delta BV \propto \Delta[Hb] + \Delta[HbO_2] \tag{5.6}$$

$$\Delta Deoxy \propto \Delta[HbO_2] - \Delta[Hb] \tag{5.7}$$

where $\Delta[Hb]$ and $\Delta[HbO_2]$ denote the relative change in deoxyhemoglobin (Hb) and oxyhemoglobin ($Hb0_2$) with respect to the collateral breast.

The concentrations of $\Delta[Hb]$ and $\Delta[HbO_2]$ were calculated using:

$$\Delta OD = \varepsilon \Delta C \Delta L \tag{5.8}$$

where OD is the optical density, ε is the known extinction coefficients of Hb, HbO_2, C is the concentration, L is the mean path-length of photons. Here, $\varepsilon \approx 1$ cm^{-1}, and $\Delta L = 4$ cm for a differential path-length factor of 7-8 [231, 232].

5.2 Feature Analysis and Tumor Classification

In this section, we present the classifiers, training techniques, statistical analysis of the dataset, and the malignancy differentiation criteria. Before we begin our discussion, note that, in our context, dataset is the set which contains all malignant and benign cases; training and test sets are subsets of the dataset.

Figure 5.3 shows the distribution of the three features for 116 patients. Blue circles indicate malignant cases and pink circles indicates benign cases. Note that the malignant class has a large spread as compared to benign class.

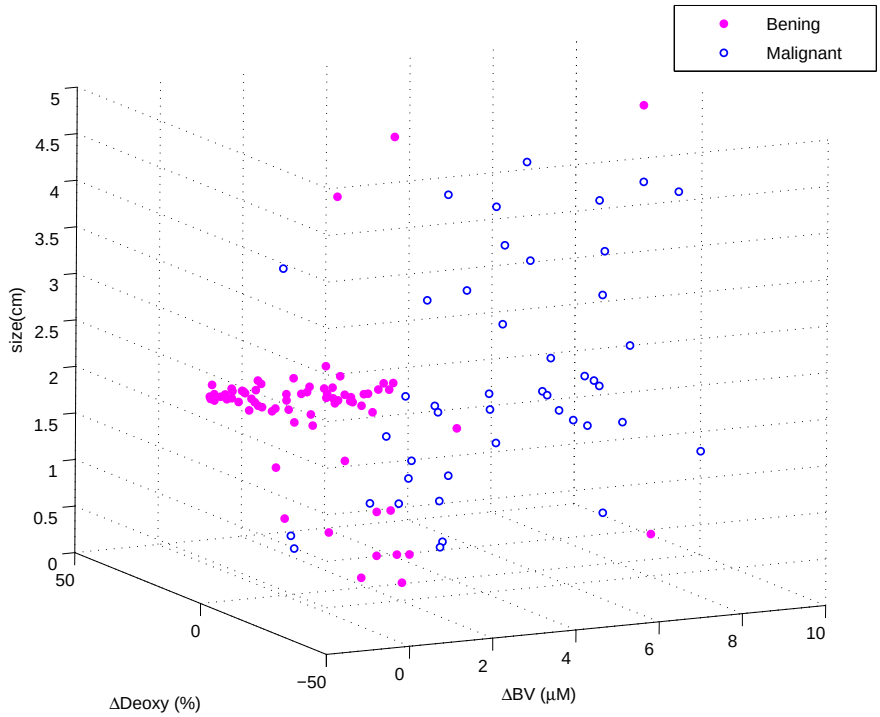

Figure 5.3: Distribution of three features, ΔBV, $\Delta Deoxy$, and S for 116 patients. Blue circles indicate malignant cases and pink circles indicates benign cases.

5.2.1 Classifiers

We evaluate the malignancy differentiation capability of the individual features and various combinations of the these features using 5 different classifiers, namely, Parzen density-based classifier (PAR), neural network classifier (NEURC), support

vector classifier (SVC), normal densities-based quadratic classifier (NDC), scaled nearest mean classifier (NMSC) [207, 233–236]. In neural network classifier, the neural network consists of units (neurons), arranged in layers, which convert an input vector into some output. Each unit takes an input, applies a (often nonlinear) function to it and then passes the output on to the next layer. Generally the networks are defined to be feed-forward: a unit feeds its output to all the units on the next layer, but there is no feedback to the previous layer. Weighings are applied to the signals passing from one unit to another, and it is these weighings which are tuned in the training phase to adapt a neural network to the particular problem at hand which is the learning phase [207, 236]. In Parzen density-based classification technique, given a kernel function, the probability distribution of the training set is approximated via a linear combination of kernels and a test set is assigned to the class with maximal posterior probability [236]. The support vector classifiers are based on support vector machines. In support vector machine based classification, each data point in the dataset is represented by a k-dimensional vector. Assuming, each data point belongs to only one of two classes, the support vector classifier separate the dataset with a $k-1$ dimensional hyperplane with maximum separation between the two classes. In other words, the nearest distance between a data point in one hyperplane and a data point in the other hyperplane is maximized [233–235]. The NDC is based on computation of a quadratic discriminant functional for the classes in the dataset using normal densities [207, 236]. Similarly, NMSC uses a linear discriminant functional for the classes in the dataset assuming equal class variances [236].

5.2.2 Classifier Training Techniques

The classifiers are trained by using three different training techniques, namely, hold-out, n-fold cross validation, and leave-one-out techniques [207, 228, 236]. In hold-out technique the original dataset (malignant and benign cases) is split into training and test sets randomly. The training set is used for generating the classification model and the test set is used to test the classification performance of the classifier. To obtain more reliable results for hold-out training technique, we

repeated the classification with different sub-samples, i.e., in each repetition, a certain proportion is randomly selected for training, the rest of data is used for testing. The error rates on different repetitions are averaged to yield an overall performance of the classifier. In the hold-out technique different test sets overlap hence it is not optimal. In order to prevent overlapping, we used the n-fold cross-validation training technique with training set size equal to $N - N/n$ and test set size N/n. Here n is the number of subsets and N is the total number of the cases including both malignant and being cases. In this technique, we split the total number of cases into $n = 10$ subsets of equal size and use each subset for testing and the remainder subset for training. The results are then averaged to get and overall classification performance. To improve our results further, we use a special case of cross-validation technique, the leave-one-out technique, with $n = N$. In this technique, one sample is used for testing, and the remanning N-1 samples are used for training the classifier. More detailed discussions on these classifiers and training techniques can be found in [207, 228, 236].

We evaluated the malignancy differentiation capability of the following individual (ΔBV, $\Delta Deoxy$, S,) and combined features (ΔBV-$\Delta Deoxy$, ΔBV- $\Delta Deoxy$-S).

5.3 Statistical Analysis of Clinical Data

We evaluated the diagnostic capability of different combinations of optical features based on receiver operating characteristics (ROC) methodology using different classifiers and training techniques [218–220]. The ROC curve is obtained by plotting the probability of false positive rate versus the probability of detection. The evaluation of classification method is done using area under the ROC curve (AUC).

First, we evaluated the classification performance of all three features combined. Table 5.1 presents the AUC values for 5 different classifiers using three different training techniques. The AUC values of 5 different classifiers using leave-one-out training technique range from 0.8864 to 0.9098 with NMSC performing the best.

Next, we evaluated the performance of the two features measured by NIR spectroscopy, namely ΔBV and $\Delta Deoxy$. Table 5.2 presents the AUC values for 5

Table 5.1: AUC values for different classifiers for ΔBV-$\Delta Deoxy$-S

	NMSC	PAR	SVC	NDC	NEURC
Leave-one-out	**0.9098**± 0.0065	0.9041± 0.0048	0.9011±0.0057	0.8984±0.0038	0.8864±0.0051
Cross-validation	**0.8905**±0.0044	0.8863±0.0039	0.8802±0.0066	0.8737±0.0029	0.8709±0.0072
Hold-out	**0.8839**±0.0040	0.8785±0.0058	0.8743±0.0027	0.8705±0.0062	0.8681±0.0066

Table 5.2: AUC values for different classifiers for ΔBV-$\Delta Deoxy$

	NMSC	PAR	SVC	NDC	NEURC
Leave-one-out	**0.9001**±0.0029	0.8993±0.0043	0.8902±0.0026	0.8908±0.0073	0.8792±0.0048
Cross-validation	**0.8896**±0.0054	0.8853±0.0070	0.8830±0.0019	0.8847±0.0062	0.8703±0.0071
Hold-out	**0.8802**±0.0048	0.8761±0.0055	0.8712±0.0091	0.8698±0.0047	0.8622±0.0063

different classifiers. The AUC values of 5 different classifiers range from 0.8792 to 0.9001 using leave-one-out training technique. Figure 5.4 show the distribution of features ΔBV, and $\Delta Deoxy$ extracted from benign and malignant tumors together with 5 different classifiers.

We next evaluated the individual classification performance of the three features. Table 5.3 presents the AUC values for 5 different classifiers for the feature ΔBV. The NMSC has the best performance in terms of classification with a AUC value of 0.8817. Table 5.4 presents the results 5 different classifiers for the feature $\Delta Deoxy$. The NMSC has the best performance in terms of classification with a AUC value of 0.8787. Table 5.5 presents the results of 5 different classifiers for the feature S. The NDC has the best performance in terms of classification with a AUC value of 0.5612.

As it can be seen from Table 5.1, the best performing feature set is the combination of the three features. However, the combination set of optical features, obtained using optical spectroscopy, can differentiate breast tumors with a relatively high precision with a AUC value of 0.9001 (Table 5.2). Similarly, optical

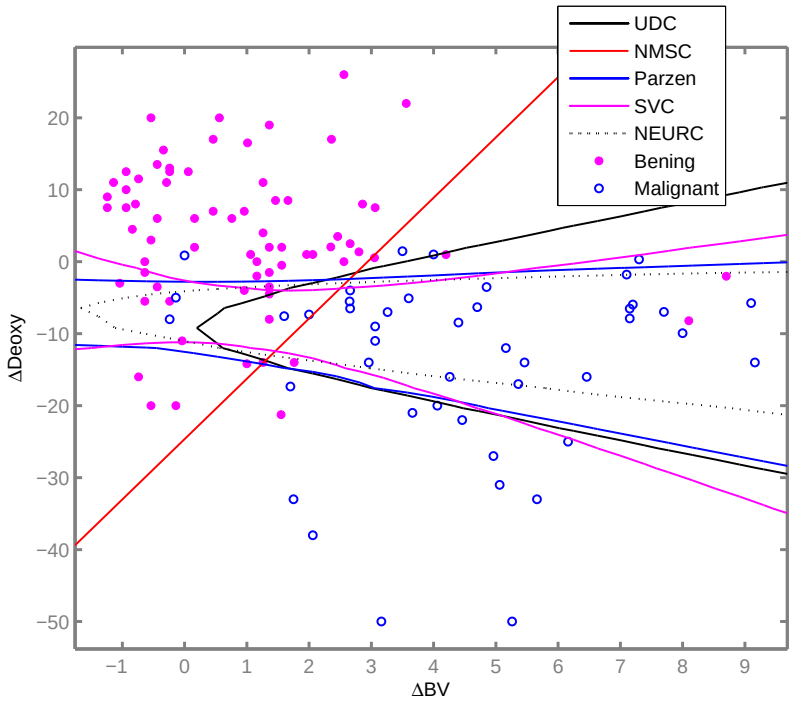

Figure 5.4: 5 different classifiers and ΔBV-$\Delta Deoxy$ 2-D data clustering.

features, ΔBV and $\Delta Deoxy$, also performed well with AUC values of 0.8817 and 0.8787, respectively (Tables 5.3 and 5.4). We can also conclude from Table 5.5 that, the tumor size alone is not informative in differentiating benign and malignant tumors.

Table 5.3: AUC values for different classifiers for ΔBV

	NMSC	PAR	SVC	NDC	NEURC
Leave-one-out	**0.8817**±0.0036	0.8802±0.0060	0.8794±0.0047	0.8779±0.0032	0.8513±0.0051
Cross-validation	**0.8742**±0.0058	0.8719±0.0069	0.8715±0.0061	0.8693±0.0070	0.8461±0.0038
Hold-out	**0.8703**±0.0021	0.8657±0.0042	0.8634±0.0018	0.8617±0.0081	0.8399±0.0067

Figure 5.5 presents, the ROC curves for all three features, and the best two features, namely, $\Delta Deoxy$ and ΔBV using the scaled nearest mean classifier. The

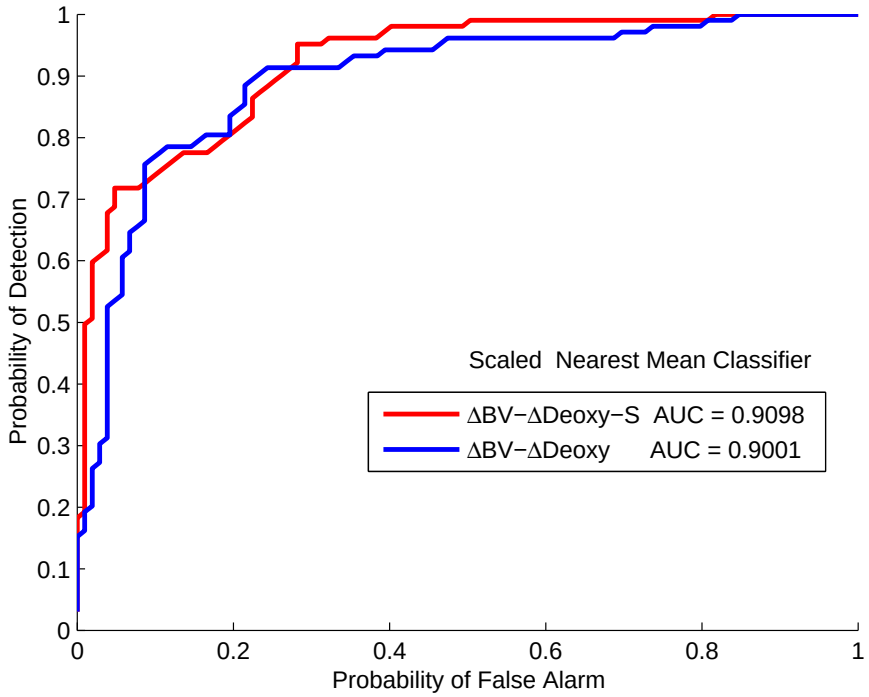

Figure 5.5: ROC curves for ΔBV-$\Delta Deoxy$-S and ΔBV-$\Delta Deoxy$ using NMSC classifier.

observed area under the ROC curve for ΔBV-$\Delta Deoxy$-S, and ΔBV-$\Delta Deoxy$ are 0.9098, and 0.9001, respectively. Figure 5.6 presents the ROC curves for individual features ΔBV, and $\Delta Deoxy$ using the scaled nearest mean classifier. The observed AUC for ΔBV, and $\Delta Deoxy$ are 0.8817 and 0.8787, respectively.

Next, we checked whether the AUC values obtained for different combinations of features are statistically different or not. If so, we can declare that some combination of features are more informative than the others for diagnostic purposes. To check the statistical difference in performance, we set up a two class hypothesis testing problem. The null hypothesis corresponds to the case of $\mathrm{AUC}_1 = \mathrm{AUC}_2$ while the alternative hypothesis corresponds to $(\mathrm{AUC}_1 \neq \mathrm{AUC}_2)$. The hypothesis test described above is reexpressed as follows:

$$H_0 \ : \Longrightarrow \quad \mathrm{AUC}_1 = \mathrm{AUC}_2 \qquad \text{(No difference in performance)}$$

$$H_1 \ : \Longrightarrow \quad \mathrm{AUC}_1 \neq \mathrm{AUC}_2 \qquad \text{(Statistical difference in performance)}$$

We assume that the features are jointly Gaussian distributed and computed

Table 5.4: AUC values for different classifiers for $\Delta Deoxy$

	NMSC	PAR	SVC	NDC	NEURC
Leave-one-out	**0.8787**±0.0044	0.8764±0.0053	0.8730±0.0069	0.8711±0.0032	0.8491±0.0060
Cross-validation	**0.8703**±0.0032	0.8688±0.0048	0.8604±0.0076	0.8598±0.0059	0.8412±0.0082
Hold-out	**0.8656**±0.0056	0.8602±0.0041	0.8567±0.0058	0.8504±0.0071	0.8389±0.0046

Table 5.5: AUC values for different classifiers for S

	NMSC	PAR	SVC	**NDC**	NEURC
Leave-one-out	0.5123±0.0101	0.5292±0.0088	0.5291±0.0074	**0.5612**±0.0081	0.5382±0.0092
Cross-validation	0.5057±0.0069	0.5233±0.0084	0.5204±0.0069	**0.5585**±0.0072	0.5301±0.0113
Hold-out	0.5001±0.0078	0.5184±0.0061	0.5178±0.0091	**0.5478**±0.0046	0.5267±0.0082

the z-statistics as:

$$z = \frac{AUC_1 - AUC_2}{\sqrt{\sigma_1^2 + \sigma_2^2 - 2r\sigma_1\sigma_2}} \tag{5.9}$$

where r is the correlation coefficient of AUC_1 and AUC_2, σ_1^2, and σ_2^2 are the variance of AUC_1 and AUC_2, respectively.

Next, we calculated the p-value based on the z-statistics [229, 230]. We reject the null hypothesis H_0 if the p-value is smaller than 0.05 (a predefined significance level), otherwise we accept the null hypothesis.

We first compared the AUC values of combined features ΔBV- $\Delta Deoxy$-S, AUC (ΔBV-$\Delta Deoxy$-S), with AUC (ΔBV-$\Delta Deoxy$) obtained by using the NMSC classifier trained with leave-one-out technique. The p-value is calculated to be 0.144. Using the hypothesis test described above, we conclude that there is no significant difference in performance using the tumor size information together with the optical features, ΔBV and $\Delta Deoxy$. We next compared the AUC values of AUC(ΔBV) and AUC($\Delta Deoxy$) obtained by using NMSC classifier. The p-value is calculated to be 0.361. Again, we found out that there is no significant difference between

the diagnostic capability of ΔBV and $\Delta Deoxy$. We also compared the values of AUC(ΔBV-$\Delta Deoxy$) with that of AUC(ΔBV) and AUC($\Delta Deoxy$). The p-values are 0.0371, and 0.0401. Using these values, based on the hypothesis testing, we can conclude that combination of optical features has better diagnostic capability then that of individual features ΔBV and $\Delta Deoxy$. Finally, we compared the AUC values of AUC(ΔBV) and AUC($\Delta Deoxy$) with the AUC value of AUC(S) obtained by using NMSC classifier. The p-values are 0.0103 and 0.0178, respectively. Using the hypothesis test, there is a significant difference in the classification performance of the optical features, ΔBV and $\Delta Deoxy$, when compared to the tumor size information.

Using the same hypothesis testing problem defined above, we compared the performances of different classifiers in terms of the AUC values obtained using three features trained with leave-one-out technique. The AUC value of NMSC classifier is statistically different from the AUC values of PAR, SVC, NDC, and NEURC classifiers with p-values of 0.0312, 0.0274, 0.0201, 0.0113, respectively. We also compared the performance of PAR classifier with SVC, NDC, and NEURC classifiers. The AUC values of PAR and SVC classifiers are not statistically different in terms of classification of three features, with a p-value of 0.182. However, the AUC value of PAR classifier is statistically different from the AUC values of NDC and NEURC classifiers with p-values of 0.0234, 0.0217, respectively. Similarly, the AUC value of SVC classifier is statistically different from NDC and NEURC classifiers with p-values of 0.0118, 0.0152, respectively. Finally, we compared the performances of NDC and NEURC classifiers. The AUC value of NDC classifier is statistically different from the AUC value of NEURC classifier with a p-value of 0.0385.

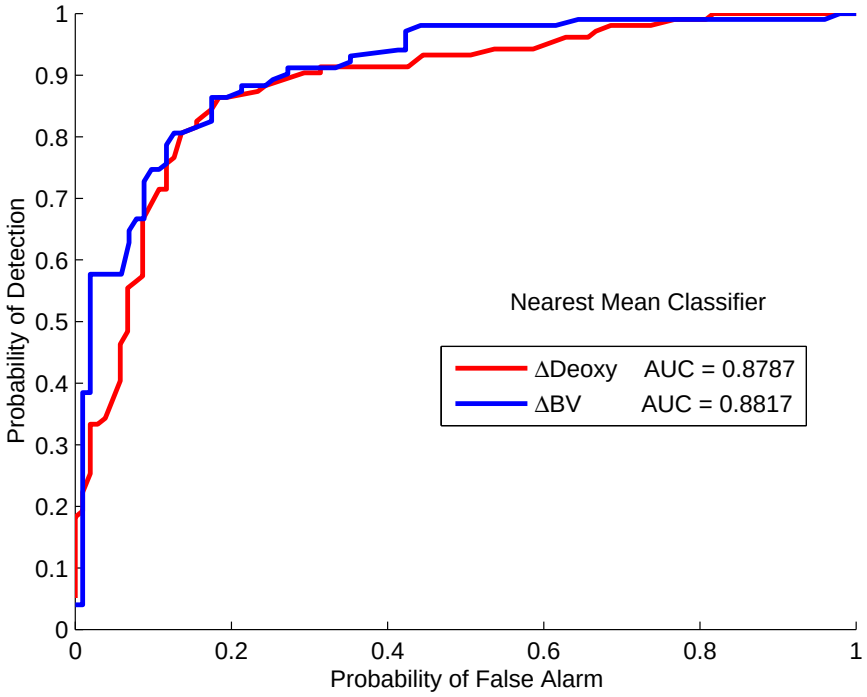

Figure 5.6: ROC curves for ΔBV and $\Delta Deoxy$ using NMSC Classifier.

CHAPTER 6
Conclusion and Future Work

6.0.1 Conclusion

In this thesis, we developed mathematical modeling and computational techniques to investigate the value of *i*) pharmacokinetic information provided by ICG; and *ii*) the endogenous contrast provided by NIR imaging and spectroscopy.

In Chapter 2, we presented three different compartmental models, an EKF framework for the modeling, and estimation of ICG pharmacokinetics in cancerous tumors based on NIR measurements. Additionally, we introduced an information theoretic criterion and residual analysis for model selection and statistical validation. The proposed compartmental models are fit to data obtained from Fischer rats with adenocarcinoma cells. The pharmacokinetic rates and volume fractions are estimated for all models. The estimated rates for all compartmental models indicate that the exchange rates between the capillary and the adjacent compartment are significantly larger for the edematous tissue as compared to the necrotic cases. Based on the BIC and residual analysis, we concluded that the two-compartment model provides the best statistical fit for the rat data and ICG pharmacokinetics. Parameters of this model indicate that the permeability rates are higher for edematous cases as compared to the necrotic tumors.

In Chapter 3, we presented a method of forming pharmacokinetic-rate images and reported pharmacokinetic-rate images of ICG for three patients with breast tumors. To form pharmacokinetic-rate images, we first obtained a sequence of ICG concentration images using the differential diffuse optical tomography technique. We next employed the two-compartment model, and estimated the pharmacokinetic-rates and concentrations in each compartment for each voxel using the EKF framework. We formed the pharmacokinetic-rate images using the *in vivo* data obtained from three patients with breast tumors. We also obtained bulk pharmacokinetic-rates for each patient. Comparison of spatially resolved and bulk ICG pharmacokinetic-rates show that ICG pharmacokinetic imaging may provide more consistent and su-

perior information than bulk ICG pharmacokinetic-rates. Along with the pharmacokinetic-rates, we also estimated the ICG concentrations in plasma and EES compartments. We observed that ICG concentrations in plasma and the EES compartments are higher in the tumor region agreeing with the hypothesis that around the tumor region ICG may act as a diffusible extravascular flow in leaky capillary of tumor vessels.

In Chapter 4, we presented a new method for the reconstruction of spatially resolved pharmacokinetic-rates, volume fractions and concentrations in different compartments for optical fluorophores directly from dynamic NIR boundary measurements. We first derived a mathematical model that maps the boundary measurements to the spatially resolved pharmacokinetic-rates and volume fractions. For this, we combined the compartmental modeling with the diffusion approximation to radiative transfer equation to model NIR light propagation in tissue. We next formed a state-space model and introduced a spatio-temporal prior model on the pharmacokinetic-rate and volume fraction images, and addressed the resulting image formation problem by the EKF framework. We performed two sets of reconstructions, first set is based on a numerical phantom and the second set is based on *in vivo* data obtained from patients with breast tumors. The first set demonstrates the performance of the proposed algorithms under different noise levels and compares them with the voxel-by-voxel reconstruction algorithm that we presented in [179]. Our simulation study shows that there is a good agreement between the true and the estimated images in terms of localization of the heterogeneities. Additionally, the EKF based direct reconstruction algorithms lead to better performance than the voxel-by-voxel reconstruction algorithm with respect to normalized mean-square error criterion. The improvements in the direct reconstruction technique can be attributed to better use of the temporal correlations between the dynamic NIR measurements by combining spatial and temporal modeling into a single step and the use of prior models on pharmacokinetic-rate images. For the processing of the *in vivo* breast data, we used a two-compartment model for the ICG pharmacokinetics and combined it with the linear NIR photon propagation model. We reconstructed the pharmacokinetic-rate images of ICG using the direct reconstruction method.

Our results show that the pharmacokinetic-rates are higher around the tumor region agreeing with the fact that permeability increases around the tumor region.

In Chapter 5, we evaluated the diagnostic capability of optical features extracted from *in vivo* near-infrared spectroscopy data. Our evaluation criteria was based on different classifiers and ROC methodology. Three features, namely, relative blood volume concentration, ΔBV, oxygenation desaturation, $\Delta Deoxy$, and the size of the tumor, S, were used to characterize benign and malignant tumors. Our results suggest that the features, relative blood volume concentration, and oxygen saturation can differentiate malignant and benign breast tumors with a relatively high precision which may help to reduce the number of unnecessary biopsies.

6.0.2 Discussion and Future Work

- While the two-compartment model is sufficient to model the ICG pharmacokinetics, higher-order compartmental models may be advantageous for modeling the pharmacokinetics of functionalized optical contrast agents that actively accumulate or activate in diseased tissue [134–136]. In the future, we plan to develop compartmental models for newly developed optical flourophores approved for human and animal use.

- The formulation and the algorithms introduced in this study can be utilized to address the reconstruction of pharmacokinetic-rate images for PET or MR contrast agents by replacing the NIR photon propagation model with the appropriate forward models for PET and MR imaging. Using our algorithms, we plan to compare the ICG pharmacokinetics with the kinetics of an MRI based agent, Gadolinium (Gd). (Gd compounds are used as contrast agents to enhance images in MRI). Similar to ICG, Gd is a blood pooling agent and may act as a diffusible extravascular flow in leaky capillary of cancer vessels. We will analyze the Gd and ICG concentration data collected simultaneously with an MRI/NIR apparatus. By using optical and MR pharmacokinetics, we will seek to explore the connections between Gd and ICG uptake in cancerous tumors.

- Real-time imaging of kinetic activity around tumor can increase the efficiency

of biopsies and accelerate interpretation of biopsy pathological review. As a part of the research on pharmacokinetic analysis, we plan to work on real-time imaging of pharmacokinetic rates. For this task, we plan to develop real-time implementation of the EKF based direct pharmacokinetic-rate imaging algorithms.

- In this thesis, we showed that pharmacokinetic-rate imaging provides a new tool to investigate and improve breast cancer diagnosis, and potentially staging. However, the available patient data is limited to fully investigate the value of ICG pharmacokinetic-rate imaging for breast cancer. We leave for future work to collect sufficient number of patient data, to extract new quantitative features from ICG pharmacokinetic-rate images, and to analyze the spatial distribution of pharmacokinetic-rates.

- Following this task, once sufficient number of patient data is available, we plan to extend our ROC studies (Chapter 5) by combining the endogenous features (i.e., relative blood volume concentration, oxygenation desaturation, the size of the tumor) and the features extracted from pharmacokinetic-rate images, (i.e., pharmacokinetic rates, the ratio of the concentrations in different compartments, volume fractions). We plan to evaluate the value of combined set of features for breast cancer diagnosis and staging.

BIBLIOGRAPHY

[1] American cancer society, statistics for 2008: http://www.cancer.org/

[2] Report of the Joint Working Group on Quantitative In Vivo Functional Imaging in Oncology, Sponsored by the *U.S. Public Health Services Office on Womens Health* and *National Cancer Institute*, 1999.

[3] L. Tabar, T. Tot, P. B. Dean, *Breast Cancer: The Art And Science Of Early Detection With Mamography: Perception, Interpretation, Histopatholigic Correlation*, Thieme Medical Publishers, 2004.

[4] N. Breen, and L. Kessler, "Changes in the use of screening mammography: evidence from the 1987 and 1990 National Health Interview Surveys," *American Journal of Public Health*, Vol. 84-1, pp. 62-67, 1994.

[5] R. E. Hendrick, R. A. Smith, J. H. Rutledge, C. R. Smart, "Benefit of screening mammography in women aged 40-49: a new meta-analysis of randomized controlled trials," *J Natl Cancer Inst Monogr*, Vol. 22, pp. 87-92, 1997.

[6] A. T. Stavros, C. L Rapp, S. H. Parker, *Breast Ultrasound*, Lippincott Williams and Wilkins, 2003.

[7] B. Alacam, B. Yazici, N. Bilgutay. "Breast Tissue Characterization using FARMA Modeling of RF Echo, *Journal of Ultrasound in Medicine and Biology*, Vol.30-10, pp. 1397-1407, 2004.

[8] E. D. Staren, T. P. O'neill, "Breast Ultrasound," The Surgical clinics of North America, Vol. 78-2, pp. 219-235, 1998.

[9] E. Morris, L. Liberman, *Breast MRI: Diagnosis and Intervention*, Springer, 2005.

[10] G. A. DeAngelis, E. E. de Lange, L. R. Miller, R. F. Morgan, "MR imaging of breast implants," *Radiographics*, Vol. 14, pp. 783-94, 1994.

[11] B. Bone, Z. Pentek, L. Perbeck, B. Veress, "Diagnostic accuracy of mammography and contrast-enhanced MR imaging in 238 histologically verified breast lesions," *Acta Radiol*, Vol. 38, pp. 489-96, 1997.

[12] Folkman, J., Tumor angiogenesis: therapeutic implications. N. Engl. J. Med., 1971. 285(21): p. 1182-6.

[13] E. M. Sevick-Muraca, G. Lopez, T. L. Troy, J. S. Reynolds, and C. L. Hutchinson, "Fluorescence and absorption contrast mechanisms for biomedical optical imaging using frequency-domain techniques, *Photochem. Photobiol.*, Vol. 66, pp. 55, 1997.

[14] J. Chang, H. Graber, and R. L. Barbour, "Imaging of fluorescence in highly scattering media," IEEE Trans. Biomed. Eng., vol. 44, pp. 810-822, 1997.

[15] V. Ntziachristos, R. Weissleder, "Experimental three-dimensional fluorescence reconstruction of diffuse media by use of a normalized Born approximation," *Opt. Lett.* Vol. 26, pp. 893, 2001.

[16] Y. Yang, N. Iftimia, Y. Xu, H. Jiang, "Frequency-domain fluorescent diffusion tomography of turbid media and in vivo tissues," *Proc. SPIE* Vol. 4250, pp. 537, 2001.

[17] S.R. Arridge, "Optical tomography in medical imaging," *Inverse Probl.* Vol. 15, R41-93, 1999.

[18] A.H. Hielschera, A.Y. Bluestonea, G.S. Abdoulaeva, A.D. Klosea, J. Laskera, M. Stewartb, U. Netzc, and J. Beuthanc, "Near-infrared diffuse optical tomography," *Disease Markers*, Vol. 18, pp. 313337, 2002.

[19] X. Intes, C. Maloux, M. Guven, B. Yazici, and B. Chance, "Diffuse optical tomography with physiological and spatial a priori constraints," *Phys. Med. Biol.*, Vol. 49 pp. N15563, 2004.

[20] A. G. Yodh, B. Chance, "Spectroscopy and imaging with diffusing light," *Phys. Today*, Vol. 48, pp. 3440, 1995.

[21] N. Shah, A. Cerussi, C. Eker, J. Espinoza, J. Butler, J. Fishkin, R. Hornung, B. Tromberg, "Noninvasive functional optical spectroscopy and human breast tissue," *Proc. Natl. Acad. Sci.*, Vol. 98, 4420-4431, 2001.

[22] X. Gu, Q. Zhang, L. Larcom, and H. Jiang, "Three-dimensional bioluminescence tomography with model-based reconstruction," *Optics Express*, Vol. 12, Issue 17, pp. 3996-4000, 2004.

[23] W. Cong, G. Wang, D. Kumar, Y. Liu, M. Jiang, L. Wang, E. A. Hoffman, G. McLennan, P. B. McCray, J. Zabner, A. Cong, "Practical reconstruction method for bioluminescence tomography," *Optics Express*, vol. 13-18, pp.6756-6761, 2005.

[24] S. A. Boppart, W. Luo, D. L. Marks, K. W. Singletary, "Optical coherence tomography: feasibility for basic research and image-guided surgery of breast cancer," *Breast Cancer Res Treat.*, Vol. 84-2, pp. 85-97, 2004.

[25] B. Alacam B, B. Yazici, X. Intes, and B. Chance, "Extended Kalman Filtering for the Modeling and Analysis of ICG Pharmacokinetics in Cancerous Tumors using NIR Optical Methods," *Transactions in IEEE Biomedical Eng.* vol. 53-10, pp. 1861-1871, 2006.

[26] X. Intes, and B. Chance, "Non-PET functional imaging techniques: Optical," *Radio. Clin. of North Am.* Vol. 43-1, pp. 221-234, 2005.

[27] F. Fedele, J. P. Laible, M. J. Eppstein, "Coupled complex adjoint sensitivities for frequency-domain fluorescence tomography: theory and vectorized implementation," *Journal of Computational Physics*, vol. 187-2, pp. 597-619, 2003.

[28] M. J. Eppstein, F. Fedele, J.P. Laible, C. Zhang, A. Godavarty and E.M. Sevick-Muraca, "A comparison of exact and approximate adjoint sensitivies in fluorescence tomography," *IEEE Transactions on Medical Imaging*, vol. 22-10, pp. 1215-1223, 2003.

[29] S. Mussurakis, D. L. Buckley, P. J. Drew, J. N. Fox, P. J. Carleton, L. W. Turnbull, and A. Horsman, "Dynamic MR imaging of the breast combined with analysis of contrast agent kinetics in the differentiation of primary breast tumours," *Clin Radiol.* Vol. 52-7, 516-526, 1997.

[30] M.J. Gorris, D. A. Gray, I.M.Y Mareels, "Reducing the computational load of a Kalman filter," *IEEE Electronic Letters*, vol. 33-18, pp. 1539-1541, 1997.

[31] V. Ntziachristos, A. G. Yodh, M. Schnall, B. and Chance, "Concurrent MRI and diffuse optical tomography of breast after indocyanine green enhancement," *Medical Sciences* Vol. 97-6, pp. 2767-2772.

[32] Su M Y, Yu H J, Carpenter P M, McLaren C E and Nalcioglu O 2005 Pharmacokinetic parameters analyzed from MR contrast enhancement kinetics of multiple malignant and benign breast lesions detected in the same patients *Technol Cancer Res Treat.* **4**(3) 255-263.

[33] Sun H, Collins J M, Mangner T J, Muzik O and Shields A 2006 Imaging the pharmacokinetics of [F-18]FAU in patients with tumors: PET studies *Cancer Chemother. Pharmacol.* **57**(3) 343-348.

[34] J. G. Fujimoto, C. Pitris, S. A. Boppart, M. E. Brezinski, "Optical coherence tomography: an emerging technology for biomedical imaging and optical biopsy," *Neoplasia*, Vol. 2(1-2), pp. 9-25, 2000.

[35] J.G. Fujimoto, "Optical coherence tomography for ultrahigh resolution in vivo imaging," *Nat Biotechnol.*, Vol. 21(11), pp. 1361-1367, 2003.

[36] U. Mahmood, C.H. Tung, A. Bogdanov Jr., and R. Weissleder,"Near infrared optical imaging of protease activity for tumor detection," *Radiology*, Vol. 213-3, pp. 866-870, 1999.

[37] M. F. Kircher, R. Weissleder, L. Josephson, "A dual fluorochrome probe for imaging proteases," *Bioconjug Chem.*, Vol. 15-2, pp. 242-248, 2004.

[38] Folkman, J., What is the evidence that tumors are angiogenesis dependent? J. Natl. Cancer inst., 1990. 82(1): p. 4-6.

[39] Blood, C. H. and B. R. Zetter, Tumor interactions with the vasculature: angiogenesis and tumor metastasis. Biochem. Biophys. Acta, 1990. 1032(1): p. 89-118.

[40] Vaupel, P., et al., Current status of knowledge and critical issues in tumor oxygenation. Results from 25 years research in tumor pathophysiology. Adv. Exp. Med. Biol., 1998. 454: p. 591-602.

[41] Vaupel, P., et al., Oxygenation of human tumors: evaluation of tissue oxygen distribution in breast cancers by computerized O2 tension measurements. Cancer Res., 1991. 51(12): p. 3316-3322.

[42] Runkel, S., et al., Oxygenations of mammary tumors as evaluated by ultrasound-guided computerized-pO2-histograpy. Adv. Exp. Med. Biol., 1994. 345: p. 451-8.

[43] Eker, C., Montan, S., Jaramillo, E., Koizumi, K., Rubio, C., Andersson-Engels, S., Svanberg, K., Svanberg, S., and Slezak, P., "Clinical spectral characterization of colonic mucosal lesions using autofluorescence and D aminolevulinic acid sensitizations," *Gut Online*, 44, 511, 1999.

[44] Leevy, C.M., Smith, F., and Longueville, J., "Indocyanine green clearance as a test for hepatic function. Evaluation by dichromatic ear densitometry," *J. Am. Med. Assoc.*, 200, 236, 1967.

[45] Kogure, K., David, N.J., Yamanouchi, U., and Choromokos, E., "Infrared absorption angiography of the fundus circulation," *Arch. Ophthalmol.*, 83(2), 209, 1970.

[46] Landsman, M.L., Kwant, G., Mook, G., and Zijlstra, W.G., "Light-absorbing properties, stability, and spectral stabilization of indocyanine green," J. *Appl. Physiol.*, 40, 575, 1976.

[47] Mordon, S., Devoisselle, J.M., Soulie, S. Begu, and Desmettre, T., "Indocyanine green: physiochemical factors affecting its fluorescence in vivo", *Microvasc. Res.*, 55, 146, 1998.

[48] Sakatani K, Kashiwasake-Jibu M, Taka Y, Wang S, Zuo H, Yamamoto K, Shimizu K, "Noninvasive optical imaging of the subarachnoid space and cerebrospinal fluid pathways based on near-infrared fluorescence," *J Neurosurg* 1997, 87:738-745.

[49] Reynolds, J.S., Troy, T.L., Mayer, R.H., Thompson, A.B., Waters, D.J., Cornell, K.K., Snyder, P.W., and Sevick-Muraca, E.M., "Imaging of spontaneous canine mammary tumors using fluorescent contrast agents," *Photochem. Photobiol.*, 70, 87, 1999.

[50] C. W. Tornoe, "Grey-Box PK/PD Modeling of Insulin," M.S. Thesis, June 28, 2002.

[51] D. H. Anderson, *Lecture Notes in Biomathematics: Compartmental Modeling and Tracer Kinetics*, Springer-Verlag, Berlin, 1983.

[52] J. A. Jacquez, *Compartmental Analysis in Biology and Medicine: Kinetics of Distribution of Tracer-labeled Materials*, Elsevier Pub. Co., New York, 1972.

[53] C. Cobelli, D. Foster, and G. Toffolo, *Tracer Kinetics in Biomedical Research: from Data to Model*, Kluwer Academic/Plenum, New York, c2000.

[54] L.P. Adler, P.F. Faulhaber, K.C. Schnur, et al., "Axillary lymph node metastases: screening with [F-18]2-deoxy-2-fluoro-D-glucose (FDG) PET," Radiology, vol. 203, pp. 323-327, 1997.

[55] J.P. Crowe, L.P. Adler, R.R. Shenk, et al., "Positron emission tomography and breast masses-comparison with clinical, mammographic, and pathological findings," Annals of Surgical Oncology, vol. 1, pp. 132-140, 1994.

[56] M. Jacobs, J. Mantil, C. Peterson, et al., "FDG PET in breast cancer," J Nucl Med, vol. 35, pp. 142P, 1994.

[57] C.J. Thompson, K. Murthy, I.N. Weinberg, et al., "Feasibility study for positron emission mammography," Med Phys, vol. 21, pp. 529-538, 1994.

[58] R.L. Wahl, R.L. Cody, G.D. Hutchins, et al., "Primary and metastatic breast carcinoma: initial clinical evaluation with PET with the radiolabeled glucose analog 2-[F-18]Fluoro-2-deoxy-D-glucose," Radiology, vol. 179, pp. 765-770, 1991.

[59] Haglund MM, Hochman DW, Spence AM, Berger MS, "Enhanced optical imaging of rat gliomas and tumor margins" *Neurosurgery* 1994, 35:930-939.

[60] J. M. Brown, A. J. Giaccia, "The unique physiology of solid tumors: opportunities (and problems) for cancer therapy," *Cancer Res.* Vol. 58(7), pp. 1408-16, 1998.

[61] H. Hashizume, P. Baluk, S. Morikawa, J. W. McLean, G. Thurston, S. Roberge, R. K. Jain, and D. M. McDonald, "Openings between Defective Endothelial Cells Explain Tumor Vessel Leakiness," *Am J Pathol.*, vol. 156(4), pp. 13631380, 2000.

[62] Ntziachristos, V., Yodh, A.G., Schnall, M., and Chance, B., "Concurrent MRI and diffuse optical tomography of the breast after indocyanine green enhancement," *Proc. Natl. Acad. Sci. U.S.A.*, 97, 2767, 2000.

[63] Mordon, S., Devoisselle, J.M., and Maunoury, V., "*In vivo* pH measurement and imaging of tumor tissue using a pH-sensitive fluorescent probe (5,6-carboxyfluorescein): instrumental and experimental studies," *Photochem. Photobiol.*, 60, 274, 1994.

[64] Folli, S., Westermann, P., Braichotte, D., Pelegrin, A., Wagnires, G., van den Bergh, H., and Mach, J.P., "Antibody-indocyanin conjugates for immunophotodetection of human squamous cell carcinoma in nude mice," *Cancer Res.*, 54, 2643, 1994.

[65] Ballou, B., Fisher, G.W., Waggoner, A.S., Farkas, D.L., Reiland, J.M., Jaffe, R., Mujumdar, R.B., Mujumdar, S.R., and Hakala, T.R., "Tumor labeling in vivo using cyanine-conjugated monoclonal antibodies," *Cancer Immunol. Immunother.*, 41, 257, 1995.

[66] Ballou, B., Fisher, G.W., Deng, J.-S., Hakala, T.R., Srivastava, M., and Farkas, D.L., "Fluorochromelabeled antibodies in vivo: assessment of tumor imaging using Cy3, Cy5, Cy5.5, and Cy7," *Cancer Detection Prev.*,22(3), 251, 1998.

[67] Soukos, N.S., Hamblin, M.R., Keelm, S., Fabian, R.L., Deutsch, T.F., and Hasan, T., "Epidermal growth factor receptor-targeted immunophotodiagnosis and photoimmunotherapy of oral precancer *in vivo*," *Cancer Res.*, 61, 4490, 2001.

[68] Goldsmith SJ, "Receptor imaging: competitive or complementary to antibody imaging," *Semin Nucleic Med* 1997, 27:85-93.

[69] Jain RK, "Barriers to drug delivery in solid tumors," *Sci Am* 1994, 271:58-65.

[70] C.H. Tung, Y. Lin, W.K. Moon, and R. Weissleder, "A receptor-targeted near-infrared fluorescence probe for in vivo tumor imaging," *Chembiochem.*, vol. 3, pp. 784786, 2002.

[71] W.K. Moon, Y. Lin, T. OLoughlin, Y. Tang, D.E. Kim, R. Weissleder, and C.H. Tung, "Enhanced tumor detection using a folate receptor-targeted nearinfrared fluorochrome conjugate," *Bioconjug. Chem.*, vol. 14, pp. 539545, 2003.

[72] M.D. Kennedy, K.N. Jallad, D.H. Thompson, D. Ben-Amotz, and P.S. Low, "Optical imaging of metastatic tumors using a folate-targeted fluorescent probe," *J. Biomed. Opt.*, vol. 8, pp. 636641, 2003.

[73] Achilefu, S., Dorshow, R.B., Bugaj, J.E., and Rajagopalan, R., "Tumor specific fluorescent contrast agents", *Proc. SPIE*, 3917, 80, 2000.

[74] Achilefu, S., Bugaj, J.E., Dorshow, R.B., Jimenez, H.N., and Rajagopalan, R., "New approach to optical imaging of tumors," *Proc. SPIE*, 4259, 110, 2001.

[75] Achilefu, S., Bugaj, J.E., Dorshow, R.B., Jimenez, H.N., Rajagopalan, R., Wilhelm, R.R., Webb, E.G., and Erion, J.L., "Site-specific tumor targeted .uorescent contrast agents," *Proc. SPIE*, 4156, 69, 2001.

[76] Bugaj, J.E., Achilefu, S., Dorshow, R.B., and Rajagopalan, R., "Novel fluorescent contrast agents for optical imaging of in vivo tumors based on a receptor-targeted dye-peptide conjugate platform," *J. Biomed. Opt.*, 6, 122, 2001.

[77] Becker, A., Hessenius, C., Licha, K., Ebert, B., Sukowski, U., Semmler, W., Wiedenmann, B., and Grotzinger, C., "Receptor-targeted optical imaging of tumors with near-infrared fluorescent ligands," *Nat. Biotechnol.*, 19, 327, 2001.

[78] Zaheer, A., Lenkinski, R.E., Mahmood, A., Jones, A.G., Cantley, L.C., and Frangioni, J.V., "*In vivo* near-infrared .uorescence imaging of osteoblastic activity," *Nat. Biotechnol.*, 19(12), 1148, 2001.

[79] Licha, K., Becker, A., Kratz, F., and Semmler, W., "New contrast agents for optical imaging: acidcleavable conjugates of cyanine dyes with biomolecules," *Proc. SPIE*, 3600, 29, 1999.

[80] Huber, M.M., Staubili, A.B., Kustedjo, K., Gray, M.H.B., Shih, J., Fraser, S., Jacobs, R.E., and Meade, T.J., "Fluorescently detectable magnetic resonance imaging agents," *Bioconjug. Chem.*, 9, 242, 1998. 3600, 29, 1999.

[81] E. Liaudet, D. Derocq, H. Rochefort, and M. Garcia, "Transfected cathepsin D stimulates high density cancer cell growth by inactivating secreted growth inhibitors," *Cell Growth Differ*, vol. 6, pp. 10451052, 1995.

[82] D. Keppler, M. Sameni, K. Moin, T. Mikkelsen, C. Diglio, and B. Sloane, "Tumor progression and angiogenesis: Cathepsin B and Co.," *Biochem. Cell Biol.*, vol. 74, pp. 799810, 1996.

[83] R. Weissleder, C.H. Tung, U. Mahmood, and A. Bogdanov Jr., "In vivo imaging of tumors with protease-activated near-infrared fluorescent probes," *Nat. Biotechnol.*, vol. 17. pp.375378, 1999.

[84] C.H. Tung, S. Bredow, U. Mahmood, and R. Weissleder, "Preparation of a cathepsin D sensitive near-infrared fluorescence probe for imaging," *Bioconjug. Chem.*, vol. 10, pp. 892896, 1999.

[85] C.H. Tung, U. Mahmood, S. Bredow, and R. Weissleder, "*In vivo* imaging of proteolytic enzyme activity using a novel molecular reporter," Cancer Res., vol. 60, pp. 49534958, 2000.

[86] A. Yodh and B. Chance, "Spectroscopy and imaging with diffusing light," Phys. Today Vol. 48-3, pp. 34-40, 1995.

[87] X. Intes and B. Chance, "Non-PET functional imaging techniques: optical," *Radiol. Clin. N Am.*, vol.43, pp.221-234, 2005.

[88] A. B. Milstein, S. Oh, K. J. Webb, C. A. Bouman, Q. Zhang, D. A. Boas, and R. P. Millane, "Fluorescence optical diffusion tomography," *Appl. Opt.* 42, 3081-3094, 2003.

[89] A. B. Milstein, J. J. Stott, S. Oh, D. A. Boas, R. P. Millane, C. A. Bouman, and K. J. Webb, "Fluorescence optical diffusion tomography using multiple-frequency data," *J. Opt. Soc. Am.* vol. A-21, 10351049, 2004.

[90] D. Boas, D. Brooks, E. Miler, C. DiMarzio, M. Kilmer, R. Gaudette, "Imaging the body with diffuse optical tomography," *IEEE Signal Processing Magazine*, vol. 18, pp. 57-74, 2001.

[91] D. Hawrys and E. Sevick-Muraca, "Developments toward diagnostic breast cancer imaging using Near-Infrared optical measurements and fluorescent contrast agents," *Neoplasia* vol.2, pp. 388-417, 2000.

[92] Furukawa, K., D. H. Crean, T. S. Mang, H. Kato and T. J. Dougherty (1995) "Fluorescence detection of premalignant, malignant, and micrometastatic disease using hexylpyropheophorbide," *Proc. SPIE* vol. 2371, pp. 510-514.

[93] Y. Chen , Q. Liu , P. Huang, S. Hyman, X. Intes, W. Lee, and B. Chance, "Assessment of tumor angiogenesis using fluorescence contrast agents," *Proc. of the SPIE*, vol. 5254, no.1, pp. 296-301, 2003.

[94] A. Becker, G. Schneider, B. Riefke, K. Licha, and W. Semmler, "Localization of near-infrared contrast agents in tumors by intravital microscopy," *Proc. SPIE* vol. 3568, pp. 112-118.

[95] M. Gurfinkel, A. B. Thompson, W. Ralston, T. L. Troy, A. L. Moore, T. A. Moore, J. D. Gust, D. Tatman, J. S. Reynolds, B. Muggenburg, K. Nikula, R. Pandey, R. H. Mayer, D. J. Hawrysz, and E. M. Sevick-Muraca, "Pharmacokinetics of ICG and HPPH-car for the detection of normal and tumor tissue using fluorescence, near-infrared reflectance imaging: a case study," *Photochem. Photobiol.,* vol. 72, pp. 94-102, 2000.

[96] D.J. Cuccia, F. Bevilacqua, A. J. Durkin, S. Merritt, B. J. Tromberg, G. Gulsen, H. Yu, J. Wang, and O. Nalcioglu, "In vivo quantification of optical contrast agent dynamics in rat tumors by use of diffuse optical spectroscopy with magnetic resonance imaging coregistration," *Applied Optics*, vol. 42, no. 1, pp. 2940-2950, June 2003.

[97] X. Intes, J. Ripoll, Y. Chen, S. Nioka, A. G. Yodh, B. Chance, "*In vivo* continuous-wave optical breast imaging enhanced with Indocyanine Green," *Med. Phys.*, vol. 30-6, pp.1039-1047, June 2003.

[98] D. Hansen, A. Spence, T. Carski, and M. Berger, "Indocyanine green (ICG) staining and demarcation of tumor margins in a rat glioma model," *Surg. Neurol.*, vol. 40, pp. 451-456, 1993.

[99] H. Shinohara, A. Tanaka, T. Kitai, N. Yanabu, T. Inomoto, S. Satoh, Hatano, Y. Yamaoka, and K. Hirao, "Direct measurement of hepatic Indocyanine Green clearance with near-infrared spectroscopy: separate evaluation of uptake and removal," *Hepatology*, vol. 23, pp. 137-144, 1996.

[100] A. ElDeosky, A. Seifalian, M. Cope, D. Delpy, and B. Davidson, "Experimental study of liver dysfunction evaluated by direct Indocyanine green clearance using near infrared spectroscopy," *Br. J. Surg.*, vol. 86, pp. 1005-1011, 1999.

[101] X. Li, B. Beauvoit, R. White, S. Nioka, B. Chance, and A. Yodh, "Tumor localization using fluorescence of Indocyanine Green (ICG) in rat models," *Proc. SPIE*, vol. 2389, pp. 789-797, 1995.

[102] M. S. Yates, C. J. Bowmer, and J. Emmerson, "The plasma clearance of indocyanine green in rats with acute renal failure: effect of dose and route of administration," *Biochem. Pharmacol.*, vol. 32, pp. 3109-3114, 1983.

[103] D. H. Anderson, *Lecture Notes in Biomathematics: Compartmental Modeling and Tracer Kinetics*, Springer-Verlag, Berlin, 1983.

[104] J. A. Jacquez, *Compartmental Analysis in Biology and Medicine: Kinetics of Distribution of Tracer-labeled Materials*, Elsevier Pub. Co., New York, 1972.

[105] C. Cobelli, D. Foster, and G. Toffolo, *Tracer Kinetics in Biomedical Research: from Data to Model*, Kluwer Academic/Plenum, New York, c2000.

[106] P. Huang, X. Intes, B. Chance, S. Nioka, "Simulation of delivery of indocynanine green injected intravenously into the human subject for breast cancer detection," *Proceedings of SPIE*, vol. 4949, pp. 450-459, 2003.

[107] S. Mordon, J. M. Devoisselle, S. Soulie-Begu, T. Desmettre, "Indocyanine Green: Physicochemical Factors Effecting Its Flourescence in vivo," *Microvascular Research*, vol. 55, pp. 146-152, 1998.

[108] S. Fickweiler, R. M. Szeimies, W. Baumler, P. Steinbach, S. Karrer, A. E. Goetz, C. Abels, F. Hofstadler, M. Landthaler, "Indocyanine Green: Intracellular Uptake and Phototherapeutic effects in vitro," *Jour. Photochem. Photobio. B: Biology*, vol. 38, pp. 178-183, 1997.

[109] P. S. Tofts, DPhil, G. Brix, D. L. Buckley, J. L. Evelhoch, E. Henderson, M. V. Knopp, H. B.W. Larsson, T. Lee, N. A. Mayr, G. J.M. Parker, R. E. Port, J. Taylor, and R. M. Weisskoff, "Estimating Kinetic Parameters From Dynamic Contrast-Enhanced T1-Weighted MRI of a Diffusable Tracer: Standardized Quantities and Symbols," *Jour. Mag. Res. Ima.*, vol. 10, pp. 223-232, 1999.

[110] P. S. Tofts, "Modeling tracer kinetics in dynamic Gd-DTPA MR imaging," *J. Magn. Reson. Imag.*, vol. 7, pp. 91-101, 1997.

[111] C. Chen, *Linear System Theory and Design*, Oxford University Press, New York, 1999.

[112] P. Zarchan, *Fundamentals of Kalman Filtering : a Practical Approach*, American Institute of Aeronautics and Astronautics, Reston, 2000.

[113] C.K.Chui, G. Chen, *Kalman Filtering with real time applications*, Springer, Berlin, 1999.

[114] C. E. Catlin, *Estimation, Control, and the Discrete Kalman Filter*, Springer, New York, 1989.

[115] L. Ljung, "Asymptotic Behavior of the Extended Kalman Filter as a Parameter Estimator for Linear Systems," *IEEE Tran. Automa. Control*, vol. AC-24, no. 1, pp. 36-50, Feb 1979.

[116] R. Togneri, and L. Deng, "Joint State and Parameter Estimation for a Target-Directed Nonlinear Dynamic System Model," *IEEE Tran. on Sig. Proc.*, vol. 51, no. 12, pp. 3061-3070, Dec 2003.

[117] L. Nelson, and E. Stear, "The Simultaneous On-Line Estimation of Parameters and States in Linear Systems," *IEEE Tran. on Auto. Control*, vol.21, pp. 94-98, Feb 1976.

[118] B. F. La Scala, and R. R. Bitmead, "Design of an extended Kalman filter frequency tracer," *IEEE Tran. on Sig. Proc*, vol. 44, no. 3, pp. 739-742, March 1996.

[119] M. Boutayeb, H. Rafaralahy, M. Darouach, "Convergence analysis of the Extended Kalman Filter used as an observer for nonlinear deterministic discrete-time systems," *IEEE Transactions on Automatic Control*, vol. 42, no. 4, pp. 581-586. 1997.

[120] B. J. Schnekenburger, "An extended Kalman filter as a parameter estimator for linear discrete time systems" M.S. thesis, University of NJIT, Newark, NJ, USA, 1988.

[121] G. Schwarz, "Estimating the dimensions of a model," *Annals. of Statistics*, vol. 6, pp. 461-464,1978.

[122] G.E.P. Box, G.M. Jenkins, and G.C. Reinsel, *Time Series Analysis: Forecasting and Control*, Third edition, Prentice Hall, 1994.

[123] H. Akaike, "Likelihood and the Bayes Procedure," Bayesian Statistics, Univ. Press, Valencia, Spain, 1980.

[124] A. Harvey, *Time Series Models*, MIT Press, 1993.

[125] W.M. Sallas and D.A. Harville, "Noninformative Priors and Restricted Maximum Likelihood Estimation in the Kalman Filter", in J.C. Spall (Ed.), Bayesian Analysis of Time Series and Dynamic Models, New York: Marcel-Dekker, Inc., 1988.

[126] F. Bevilacqua, A. J. Berger, A. E. Cerussi, D. Jakubowski, and B. J. Tromberg, "Broadband absorption spectroscopy in turbid media by combined frequency-domain and steady-state methods," *Appl. Opt.*, vol. 39, pp. 6498-6507, 2000.

[127] D. J. Jakubowski, "Development of broadband quantitative tissue optical spectroscopy for the non-invasive characterization of breast disease," Beckman Laser Institute, University of California, Irvine, Irvine, Calif., 2002.

[128] S. Merritt, F. Bevilacqua, A. J. Durkin, D. J. Cuccia, R. Lanning, B. J. Tromberg, G. Gulsen, H. Yu, J. Wang, and O. Nalcioglu, "Monitoring tumor physiology using near-infrared spectroscopy and MRI coregistration," *Appl. Opt.*, vol. 42, pp. 2951-2959, 2003.

[129] L.M. Gray, L.D. Davisson, *An Introduction to Statistical Signal Processing*, Cambridge University Press, Boston, 2004.

[130] M. Y. Su, A. Muhler, X. Lao, and O. Nalcioglu, "Tumor characterization with dynamic contrast-enhanced MRI using MR contrast agents of various molecular weights," *Magn. Reson. Med.*, vol. 39, pp. 259-269, 1998.

[131] J. B. Fishkin, O. Coquoz, E. Anderson, M. Brenner, and B. J. Tromberg, "Frequency-domain photon migration measurements of normal and malignant tissue optical properties in a human subject," *Appl. Opt.*, vol. 36, pp. 10-20, 1997.

[132] D. L. Buckley, "Uncertainty in the analysis of tracer kinetics using dynamic contrast-enhanced T1-weighted MRI," *Magn. Reson. Med.*, vol. 47, pp. 601-606, 2002.

[133] A. Gelb, *Applied Optimal Estimation*, M.I.T. Press, Cambridge, 1989.

[134] K. Licha, "Contrast agents for optical imaging," *Topics in Current Chemistry*, vol.222, pp.1-29, 2002.

[135] Y. Chen, G. Zheng, Z. Zhang, D. Blessington, M. Zhang, H. Li, "Metabolism Enhanced Tumor Localization by Fluorescence Imaging: In Vivo Animal Studies," *Optics Letters*, vol. 28, pp. 2070-2072, 2003.

[136] R. Weissleder, C. H. Tung, U. Mahmood, A. Bogdanov, "In vivo imaging with protease-activated near-infrared fluorescent probes," *Nat. Biotech.*, vol. 17, pp. 375-378, 1999.

[137] B. Alacam, B. Yazici, X. Intes, B. Chance "Extended Kalman Filtering Framework for the Modeling and Analysis of ICG Pharmacokinetics," *Proc. Of 2005 SPIE Photonic West,* San Jose, California USA, 22 - 27 January 2005, vol. 5693. pp. 17-27.

[138] B. Alacam, B. Yazici, X. Intes, B. Chance "Analysis of ICG Pharmacokinetics in Cancerous Tumors using NIR Optical Methods," *Proc. of* $EMBS - 27^{th}$ *Anniversary Conference*, Shanghai, China, September 2005.

[139] J. Ripoll, V. Ntziachristos, R. Carminati, and M. Nieto-Vesperinas, "Kirchhoff approximation for diffusive waves," *Phys. Rev.* E 64, 051917, 2001.

[140] J. Ripoll, V. Ntziachristos, J. P. Culver, D. N. Pattanayak, A. G. Yodh, and M. Nieto-Vesperinas, "Recovery of optical parameters in multiplelayered diffusive media: theory and experiments," *J. Opt. Soc. Am.* A 18, 821830, 2001.

[141] D. Boas, T. Gaudette, and S. Arridge, "Simultaneous imaging and optode calibration with diffuse optical tomography," *Opt. Express* 8, 263270, 2001.

[142] P. Hansen and D. OLeary, "The use of the L-curve in the regularization of discrete ill-posed problems," *SIAM J. Sci. Comput.*, 14, 1487 1503, 1993.

[143] S. Nioka, Y. Yung, M. Schnall, S. Zhao, S. Orel, C. Xie, B. Chance, and S. Solin, "Optical imaging of breast tumor by means of continuous waves," *Adv. Exp. Med. Biol.*, 411, 227232, 1997.

[144] L. A. Bauer, *Applied Clinical Pharmacokinetics*, McGraw-Hill, New York, 2001.

[145] Sevick-Muraca, E.M., Lopez, G., Troy, T.L., Reynolds, J.S., and Hutchinson, C.L.,"Fluorescence and absorption contrast mechanisms for biomedical optical imaging using frequency-domain techniques," *Photochem. Photobiol.*, 66, 55, 1997.

[146] M. J. Eppstein, D. E. Dougherty, T. Troy, E. M. Sevick-Muraca, "Biomedical optical tomography using dynamic parameterization and Bayesian conditioning on photon migration measurements." Applied Optics, vol. 38-10, pp. 2138-2150, 2001.

[147] V. Kolehmainen, S. Prince, S. R. Arridge, and J. P. Kaipio,"State-estimation approach to the nonstationary optical tomography problem," *J. Opt. Soc. Am.* A 20, 876889 (2003).

[148] S. Prince, V. Kolehmainen, J. P. Kaipio, M. A. Franceschini, D. Boas, and S. R. Arridge,"Time-series estimation of biological factors in optical diffusion tomography," *Phys. Med. Biol.* Vol. 48, 14911504 (2003).

[149] M. Kamasak, C. A. Bouman, E. D. Morris, and K. Sauer, "Direct Reconstruction of Kinetic Parameter Images from Dynamic PET Data," *IEEE Trans Med Imag*, vol. 24, pp. 636-650, 2005. 1919-1923.

[150] A. B. Milstein, K. J. Webb, and C. A. Bouman, "Estimation of kinetic model parameters in fluorescence optical diffusion tomography," J. Opt. Soc. Am., Vol. 22, No. 7, pp. 1357-1368.

[151] Li, X., Chance, B., and Yodh, A.G.,"Fluorescence heterogeneities in turbid media limits for detection, characterization, and comparison with absorption," *Appl. Opt.*, 37, 6833, 1998.

[152] O'Leary, M.A., Boas, D.A., Li, X.D., Chance, B., and Yodh, A.G.,"Fluorescence lifetime imaging in turbid media," *Opt. Lett.* **21**, 158-160, 1996.

[153] Ntziachristos, V., Graves, E., Schultz, R., Ripoll, J.,"Fluorescence Molecular Tomography: New Detection Schemes for Acquiring High Information Content Measurements," ISBI 2004: 1475-1477.

[154] Graves, E.E., Weissleder, R., Ntziachristos, V.,"Fluorescence Molecular Imaging of Small Animal Tumor Models," *Current Molecular Medicine*, **4(4)**, 419-430, 2004.

[155] Schultz, R., Ripoll, J., Ntziachristos, V.,"Experimental fluorescence tomography of tissues with non-contact measurements," *IEEE Med. Imag.* **23(4)**, 492-500, 2004.

[156] Graves, E.E., Ripoll, J., Weissleder, R., Ntziachristos, V.,"A submillimeter resolution fluorescence molecular imaging system for small animal imaging," *Medical Physics* **30 (5)**, 901-911, 2003.

[157] Lopez, G., Troy, T.L., Hutchinson, C.L., Reynolds, J.S., and Sevick-Muraca, E.M., "Fluorescent contrast agents for biomedical optical imaging using frequency-domain techniques," J. R. Lakowicz and R. B. Thompson, eds., *Proc. SPIE*, pp. 2980, 1997.

[158] Yoo, K.M., Zang, Z.-H., Ahmed, S.A., and Alfano, R.R.,"Imaging objects hidden in scattering media using a fluorescence-absorption technique," *Opt. Lett.* **16**, 1252-1254, 1991.

[159] Knüttel, A., Schmitt, J.M., Barnes, R., and Knutson, J.R., "Acousto-optic scanning and interfering photon density waves for precise localization of an absorbing (or fluorescent) body in a turbid medium," *Rev. Sci. Instrum.* **64**, 638-644, 1993.

[160] O'Leary, M.A., Boas, D.A., Chance, B., and Yodth, A.G., "Reradiation and imaging of diffuse photon density waves using fluorescent inhomogeneities," *J. Luminescence*, 60(61), 281, 1994.

[161] E.D. Aydin, C. R. E. de Oliveira, and A. J. H. Goddard, "A comparison between transport and diffusion calculations using a finite element-spherical harmonics radiation transport method," *Med. Phys.*, 29, pp. 2013-23, 2002.

[162] A. H. Hielscher, R. E. Alcouffe, and R. L. Barbour, "Comparison of finite-difference transport and diffusion calculations for photon migration in homogeneous and heterogeneous tissues," *Phys. Med. Biol.*, 43, pp. 1285-1302, 1998.

[163] B. Chen, K. Stammes, and J. J. Stamnes, "Validity of the diffusion approximation in bio-optical imaging," *Appl. Opt.*, 40 (34), pp. 6356-6366, 2001.

[164] A. D. Kim, and A. Ishimaru, "Optical diffusion of continuous-wave, pulsed, and density waves in scattering media and comparisons with radiative transfer," *Appl. Opt.*, 37 (22), pp. 5313-5319, 1998.

[165] G. S. Abdoulaev, A. H. Hielscher, "Three-dimensional optical tomography with the equation of radiative transfer," *J. Electronic Imaging*, 12 (4), pp. 594-601, 2003.

[166] M. O'Leary, "Imaging with Diffuse Photon Density Waves," in PhD Thesis, Dept. Physics & Astronomy, U. of Pennsylvania, May 1996.

[167] Ntziachristos, V., Weissleder, R., "Experimental three-dimensional fluorescence reconstruction of diffuse media by use of a normalized Born approximation," *Optics Letters*, **26**(12): 893-895, 2001. 20. S. R.

[168] M. Schweiger, S. R. Arridge, and D. T. Delpy, "The finite element method for the propagation of light in scattering media: Boundary and source conditions," *Med. Phys.*, 22 (11), pp. 1779-1792, 1995.

[169] C.K.Chui, G. Chen, *Kalman Filtering with real time applications*, Springer, Berlin, 1999.

[170] B. F. La Scala, and R. R. Bitmead, "Design of an extended Kalman filter frequency tracer," *IEEE Tran. on Sig. Proc*, vol. 44, no. 3, pp. 739-742, March 1996.

[171] M. Boutayeb, H. Rafaralahy, M. Darouach, "Convergence analysis of the Extended Kalman Filter used as an observer for nonlinear deterministic discrete-time systems," *IEEE Transactions on Automatic Control*, vol. 42, no. 4, pp. 581-586. 1997.

[172] B. J. Schnekenburger, "An extended Kalman filter as a parameter estimator for linear discrete time systems" M.S. thesis, University of NJIT, Newark, NJ, USA, 1988.

[173] G. Beer and J. O. Watson, "Introduction to Finite and Boundary Element Methods for Engineers," Wiley, Chichester, UK, 1992.

[174] J.Ripoll, V. Ntziachristos, A.G. Yodh, R. Carminati, and M. Nieto-Vesperinas, "Kirchhoff approximation for diffusive waves," *Physical Review* E 64, 0519171-0519178 , 2001.

[175] M. S. Patterson, B. Chance and B. C. Wilson, "Time resolved reflectance and transmittance for the noninvasive measurement of tissue optical properties," *Appl. Opt* 28, pp. 22312336, 1989.

[176] M. A. Franceschini, K. T. Moesta, S. Fantini, G. Gaida, E. Gratton, H. Jess, W. Mantulin, M. Seeber, P. M. Schlag and M. Kaschke, "Frequency-domain techniques enhance optical mammography: initial clinical results," *Proc. Natl. Acad. Sci. USA* 94 (12), pp. 64686473, 1997.

[177] A. Soubret, J. Ripoll, V. Ntziachristos, "Accuracy of fluorescent tomography in the presence of heterogeneities: study of the normalized Born ratio," *IEEE Trans. Med. Imaging*, 24 (10), pp. 1377-1386, 2005.

[178] B. Alacam, B. Yazici, Ahmed Serdaroglu, X. Intes, B. Chance, "Reconstruction of Spatially Resolved Pharmacokinetic Rate Images of Fluorescence Agents in FDOT in *Proc. of EMBS-28th Anniversary Conference*, pp. 5627-5630, New York City, USA, September 2006.

[179] B. Alacam, B. Yazici, X. Intes, B. Chance, "Spatially Resolved Pharmacokinetic Rate Images of ICG using Near Infrared Optical Methods," *Journal of Physics of Medicine and Biology*, Vol. 53-4, pp. 837-859, 2008.

[180] B. Alacam, B. Yazici, X. Intes, S. Nioka, B. Chance, Direct Reconstruction of Pharmacokinetic Rate Images of Indocyanine Green in Fluorescence Molecular Tomography *Proceedings of Biomedical Optics Topical Meeting*, pp. SH65, Fort Lauderdale, USA, March 2006.

[181] B. Alacam, B. Yazici, X. Intes, S. Nioka, B. Chance, "Spatially Resolved Pharmacokinetic Rate Images of ICG using Near Infrared Optical Methods, *Proc. of 2006 SPIE Photonic West*, San Jose, California USA, 21- 26 January 2006, vol. 6088. pp. 455-464.

[182] A. Soubret, and V. Ntziachristos, "Fluorescence molecular tomography in the presence of background fluorescence," *Phys. Med. Biol.*, Vol. 51, pp. 3983-4001, 2006.

[183] B. Alacam and B. Yazici"Reconstruction of Spatially Resolved Pharmacokinetic Rate Images of Optical Fluorophores from NIR Measurements", submitted to *IEEE Transactions in Medical Imaging.*

[184] B. Alacam, B. Yazici, X. Intes, B. Chance, "Evaluation of NIR Optical Features for Breast Cancer Diagnosis using *in vivo* Patient Data," submitted to IEEE Transactions in Biomedical Engineering.

[185] B. Alacam, B. Yazici. B. Chance, S. Nioka, "Characterization of Breast Tumors with NIR Methods using Optical Indices," in Proc. of IEEE EMBS-29th Anniversary Conference, pp. 5186-5189, Lyon, France, August 2007.

[186] S. C. Brenner, and L. R. Scott, *The mathematical theory of finite element methods*, Springer, Berlin, 1994.

[187] D. H. Anderson, *Lecture Notes in Biomathematics*, Springer-Verlag, Berlin, 1983.

[188] J. A. Jacquez, *Compartmental analysis in biology and medicine, Kinetics of distribution of tracer-labeled materials*, Elsevier Pub. Co., New York, 1972.

[189] V. Ntziachristos, B. Chance, and A. Yodh,"Differential diffuse optical tomography," Opt. Express 5, 230-242 (1999).

[190] S. R. Arridge, "Optical tomography in medical imaging: topical review," Inverse Problems, Vol.15 pp. R4193, 1999.

[191] C.K.Chui, G. Chen, *Kalman Filtering with real time applications*, Springer, Berlin, 1999.

[192] M. Seul, M. J. Sammon, L. O'Gorman, *Image Analysis, Random Fields and Markov Chain Monte Carlo Methods: A Mathematical Introduction*, Springer, New York, 2000.

[193] S. Z. Li, *Markov Random Field Modeling in Image Analysis*, Springer-Verlag, Telos, 2001.

[194] R. Chellappa, A. Jain, *Markov Random Fields, Theory and Application*, Academic Press, San Diego, 1993.

[195] R. L. Barbour, H. L. Graber, C. H. Schmitz, Y. Pei, S. and Zhong, "Spatio-temporal imaging of vascular reactivity in optical tomography," *Proc. of the Inter-Institute Workshop on in-vivo Optical Imaging* pp. 161167, 1999.

[196] A.Y. Bluestone, G. Abdoulaev, C. H. Schmitz, R. L. Barbour, and A. H. Hielscher,"Three-dimensional optical tomography of hemodynamics in the human head," *Opt. Express* , Vol.9 pp. 272286, 2001.

[197] M. J. Eppstein, D.J. Hawrysz, A. Godavarty, and S. Muraca,"Three dimensional near infrared fluorescence tomography with Bayesian methodologies for image reconstruction from sparse and noisy data sets," *Proc. Natl Acad. Sci.* Vol. 99, pp. 96199624.

[198] M. Guven, B. Yazici, X. Intes, and B. Chance, "Diffuse optical tomography with a priori anatomical information," *Phys. Med. Biol.*, Vol. 50, pp. 2837-2858.

[199] A. H. Hielscher, and S. Bartel, "Use of penalty terms in gradient-based iterative reconstruction schemes for optical tomography," *J. Biomed. Opt.*, Vol.6, pp. 183192.

[200] K. D. Paulsen, and H. Jiang, "Enhanced frequency domain optical image reconstruction in tissues through total variation minimization," *Appl. Opt.*, Vol. 35, pp. 34473458.

[201] B. W. Pogue, T. O. McBride, J. Prewitt, U. L. Osterberg, and K. D. Paulsen, "Spatially varying regularization improves diffuse optical tomography," *Appl. Opt.*, Vol. 38, pp. 29502961.

[202] C. C. Martin, R. F. Williams, J. H. Gao, L. D. Nickerson, J. Xiong, P. T. Fox. "The pharmacokinetics of hyperpolarized xenon: implications for cerebral MRI," *J Magn Reson Imaging*, Vol. Sep-Oct;7(5), pp. 848-854, 1997.

[203] G. R. Moran, F. S. Prato, "Modeling (1H) exchange: an estimate of the error introduced in MRI by assuming the fast exchange limit in bolus tracking," *Magn Reson Med.*, Vol. Apr;51(4), pp. 816-827, 2004.

[204] R. Srikanchana, D. Thomasson, P. Choyke, A. Dwyer, "A Comparison of Pharmacokinetic Models of Dynamic Contrast Enhanced MRI,", *7th IEEE Symposium on Computer-Based Medical Systems*, p.361, 2004.

[205] O. Langer, R. Karch, U. Mller, G. Dobrozemsky, A. Abrahim, M. Zeitlinger, E. Lackner, C. Joukhadar, R. Dudczak, K. Kletter, M. Mller, M. Brunner, "Combined PET and Microdialysis for In Vivo Assessment of Intracellular Drug Pharmacokinetics in Humans," *Journal of Nuclear Medicine*, Vol. 46 No. 11, pp. 1835-1841.

[206] K. Kwon and B. Yazici, "Born expansion and Frechet derivatives in diffuse optical tomography, submitted to Inverse Problems, May 2006.

[207] Fukunaga K. Introduction to Statistical Pattern Recognition, New York:Academic Press, 1990.

[208] Fantini S, Hueber D, Franceschini MA, Gratton E, Rosenfeld W, Stubblefield PG, Maulik D, Stankovic MR., "Non-invasive optical monitoring of the newborn piglet brain using continuous-wave and frequency-domain spectroscopy," *Phys. Med. Biol.*, Vol. 44, pp. 1543-1563, 1999.

[209] X. Intes, J. Yu, A. G. Yodh, and B. Chance, "Developement and evaluation of a multi-wavelength mulit-channel timeresolved optical instrument for NIR/MRI mammography co-registration," *Bioengineering Conference*, Proceedings of the IEEE 28th Annual Northeast, pp. 91-92, 2002.

[210] National Cancer Institute, Breast Cancer, 2008.

[211] A. M. Leitch, G. D. Dodd, M. Costanza, "American Cancer Society guidelines for the early detection of breast cancer," *CA Cancer J Clin*, Vol. 47, pp. 50-153, 1997.

[212] K. Kerlikowske, J. Barclay, "Outcomes of modern screening mammography," *J Natl Cancer Inst Monogr*, vol. 22, pp. 105-111.

[213] B. Alacam, B. Yazici, N. Bilgutay et al, Breast Tissue Characterization using FARMA Modeling of RF Echo, *Journal of Ultrasound in Medicine and Biology*, vol.30-10, pp. 1397-1407, 2004.

[214] J. W. Tian, L. T. Sun, Y. H. Guo, H. D., Zhang Y.T., "Computerized-aid diagnosis of breast mass using ultrasound image," Medical Physics, vol. 34-8, 3158-3164, 2007.

[215] L. Liberman, E. A. Morris, D. D. Dershaw et al, "MR imaging of the ipsilateral breast in women with percutaneously proven breast cancer," *AJR Am J Roentgenol.*, vol. 180, pp. 901-910, 2003.

[216] M. Van Goethem, K. Schelfout, L. Dijckmans, J. C. Van Der Auwera, J. Weyler, I. Verslegers, I. Biltjes and A. De Schepper, " MR mammography in the pre-operative staging of breast cancer in patients with dense breast tissue: comparison with mammography and ultrasound," *European Radiol*, vol. 14(5), pp. 809-816, 2004.

[217] Report of the Joint Working Group on Quantitative In Vivo Functional Imaging in Oncology, Sponsored by the *U.S. Public Health Services Office on Womens Health* and *National Cancer Institute*, 1999.

[218] J. A. Swets, "ROC Analysis applied to the evaluation of medical imaging techniques," *Investigative Radiology*, vol. 14, pp. 109-121, 1979.

[219] C. E. Metz, "ROC methodology in radiologic imaging,"*Investigative Radiology*, vol. 21, pp. 720-733, 1986.

[220] D. D. Dorfman, K. S. Berbaum, C. E. Metz, "Receiver operating characteristics rating analysis: generalization of the population of readers and patients with the jackknife method," *Invest Radiol*, vol. 27, pp. 723731, 1992.

[221] B. W. Pogue, S. Jiang, H. Dehghani, C. Kogel, S. Soho, S. Srinivasan, X. Song, T. D. Tosteson, S. P. Poplack, K. D. Paulsen, "Characterization of hemoglobin, water, and NIR scattering in breast tissue: analysis of intersubject variability and menstrual cycle changes," *Journal of Biomedical Optics*, Vol. 9(3), pp. 541552, 2004.

[222] D. Grosenick, H. Wabnitz, K T. Moesta, J. Mucke, M. Mller, C. Stroszczynski, J. Stel, B. Wassermann, P. M. Schlag, and H. Rinneberg, "Concentration and oxygen saturation of hemoglobin of 50 breast tumours determined by time-domain optical mammography," *Phys. Med. Biol.* Vol. 49 No. 7, pp. 1165-1181, 2004.

[223] M. Khayat, Z. Ichalalene, N. Mincu, F. Leblond, O. Guilman, and S. Djeziri, "Optical tomography as adjunct to x-ray mammography: methods and results," *Proc. of SPIE*, Vol. 6431 64310F-1, 2007.

[224] R. X. Xu, D. C. Young, J. J. Mao, S. P. Povoski, "A prospective pilot clinical trial evaluating the utility of a dynamic near-infrared imaging device for characterizing suspicious breast lesions," *Breast Cancer Research*, Vol. 9-6, pp. 1-12, 2007.

[225] B. J. Tromberg, N. Shah, R. Lanning, A. Cerussi, J. Espinoza, T. Pham, L. Svaasand, and J. Butler, "Non-invasive in vivo characterization of breast tumors using photon migration spectroscopy," Neoplasia Vol. 2 (12), pp. 2640, 2000.

[226] V. Ntziachristos, B. Chance, "Probing physiology and molecular function using optical imaging: applications to breast cancer," *Breast Cancer Res.*, Vol. 3, pp. 41-46, 2001.

[227] P. Vaupel, A. Mayer, S. Briest, and M. Hockel, "Oxygenation gain factor: a novel parameter characterizing the association between hemoglobin level and the oxygenation status of breast cancers," *Cancer Res.*, Vol. 63, pp. 76347637, 2003.

[228] B.D. Ripley, *Pattern Recognition and Neural Networks*, Cambridge:Cambridge University Press,1996.

[229] J. A. Hanley, B. J. McNeil, "The meaning and use of the area under a receiver operating characteristic (ROC) curve," *Radiology*, vol. 143, pp. 29-36, 1982.

[230] J. A. Hanley, B. J. McNeil, "A method of comparing the areas under receiver operating characteristic curves derived from the same cases," *Radiology*, vol. 148, pp. 839-843, 1983.

[231] B. Chance, S. Nioka, J. Zhang, E. F. Conant, E. Hwang, S. Briest, S. G. Orel, M. D. Schnall, B. J. Czerniecki, "Breast cancer detection based on incremental biochemical and physiological properties of breast cancers: a six-year, two-site study," *Academic Radiology*, Vol. 12, Issue 8, pp. 925-933, 2005.

[232] S. Fantini, D. Hueber, M. A. Franceschini, E. Gratton, W. Rosenfeld, P. G. Stubblefield, D. Maulik, M. R. Stankovic, "Non-invasive optical monitoring of the newborn piglet brain using continuous-wave and frequency-domain spectroscopy," *Phys. Med. Biol.*, Vol. 44, pp. 1543-1563, 1999.

[233] D. Fradkin and I. Muchnik "Support Vector Machines for Classification", *DIMACS Series in Discrete Mathematics and Theoretical Computer Science*, vol. 70, pp. 13-20, 2006.

[234] P. H. Chen, C. J. Lin, and B. Schlkopf, "A tutorial on support vector machines," *Appl. Stoch. Models. Bus. Ind.* vol. 21, pp. 111-136, 2005.

[235] N. Cristianini and J. Shawe-Taylor, *An Introduction to Support Vector Machines*, Cambridge: Cambridge University Press, 2000.

[236] R. O. Duda, P. E. Hart, D. G. Stork, *Pattern Classification*, New York: Wiley-Interscience, 2000.